

6112-AN-01

DTIC FILE COPY

(1)

AD-A222 870

DEFORMATION, FRACTURE AND EXPLOSIVE PROPERTIES OF REACTIVE MATERIALS

Principal Investigator: Dr J E Field

EUROPEAN RESEARCH OFFICE

United States Army
London W1, England

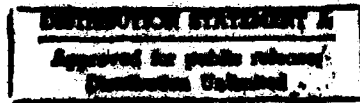
DTIC
SELECTED
JUN 13 1990
S B

Contract No DAJA45-89-C-0009

FINAL TECHNICAL REPORT DECEMBER 1989

Physics and Chemistry of Solids
Cavendish Laboratory
University of Cambridge
Madingley Road
Cambridge CB3 0HE
England

"The research supported in this document has been made possible through
the support and sponsorship of the US Government through its European
Research Office of the US Army. This report is intended only for the
~~internal management use of the Contractor and the US Government~~"



90 06 12 070

Unclassified

SECURITY CLASSIFICATION OF THIS PAGE

REPORT DOCUMENTATION PAGE				Form Approved OMB No 0704-0188 Exp Date Jun 30 1986									
1a. REPORT SECURITY CLASSIFICATION Unclassified		1b. RESTRICTIVE MARKINGS											
2a. SECURITY CLASSIFICATION AUTHORITY		3. DISTRIBUTION/AVAILABILITY OF REPORT Approved for public release; distribution unlimited											
2b. DECLASSIFICATION/DOWNGRADING SCHEDULE													
4. PERFORMING ORGANIZATION REPORT NUMBER(S)		5. MONITORING ORGANIZATION REPORT NUMBER(S) R&D 4380A-R-AN											
6a. NAME OF PERFORMING ORGANIZATION University of Cambridge	6b. OFFICE SYMBOL (if applicable)	7a. NAME OF MONITORING ORGANIZATION USARDSG(UK)											
6c. ADDRESS (City, State, and ZIP Code) Cavendish Laboratory, Madingley Road, Cambridge CB3 OHE, England	7b. ADDRESS (City, State, and ZIP Code) Box 65 FPO New York 09510-1500												
8a. NAME OF FUNDING / SPONSORING ORGANIZATION USARDSG(UK)	8b. OFFICE SYMBOL (if applicable) AMXSN-UK-RA	9. PROCUREMENT INSTRUMENT IDENTIFICATION NUMBER DAJA45-89-C-0009											
8c. ADDRESS (City, State, and ZIP Code) Box 65 FPO New York 09510-1500	10. SOURCE OF FUNDING NUMBERS <table border="1"><tr><td>PROGRAM ELEMENT NO.</td><td>PROJECT NO.</td><td>TASK NO</td><td>WORK UNIT ACCESSION NO</td></tr><tr><td>61103A</td><td>1L161103BH57</td><td>06</td><td></td></tr></table>			PROGRAM ELEMENT NO.	PROJECT NO.	TASK NO	WORK UNIT ACCESSION NO	61103A	1L161103BH57	06			
PROGRAM ELEMENT NO.	PROJECT NO.	TASK NO	WORK UNIT ACCESSION NO										
61103A	1L161103BH57	06											
11. TITLE (Include Security Classification) (U) Deformation, Fracture and Explosive Properties of Reactive Materials													
12. PERSONAL AUTHOR(S) J. Field													
13a. TYPE OF REPORT Final	13b. TIME COVERED FROM Nov 88 TO Dec 89	14. DATE OF REPORT (Year, Month, Day) 1989.12.08	15. PAGE COUNT 92										
16. SUPPLEMENTARY NOTATION													
17. COSATI CODES <table border="1"><tr><td>FIELD</td><td>GROUP</td><td>SUB-GROUP</td></tr><tr><td>19</td><td>01</td><td></td></tr><tr><td>19</td><td>09</td><td></td></tr></table>		FIELD	GROUP	SUB-GROUP	19	01		19	09		18. SUBJECT TERMS (Continue on reverse if necessary and identify by block number) Explosives, ignition, impact, sensitiveness, hot spots, high speed photography, deformation fracture, PETN, HMX, PBX's		
FIELD	GROUP	SUB-GROUP											
19	01												
19	09												
19. ABSTRACT (Continue on reverse if necessary and identify by block number)													
See overleaf													
20. DISTRIBUTION/AVAILABILITY OF ABSTRACT <input checked="" type="checkbox"/> UNCLASSIFIED/UNLIMITED <input type="checkbox"/> SAME AS RPT. <input checked="" type="checkbox"/> DTIC USERS		21. ABSTRACT SECURITY CLASSIFICATION Unclassified											
22a. NAME OF RESPONSIBLE INDIVIDUAL Dr. R E Keichenbach		22b. TELEPHONE (Include Area Code) 01-409 4423	22c. OFFICE SYMBOL AMXSN-UK-RA										

DD FORM 1473, 84 MAR

83 APR edition may be used until exhausted
All other editions are obsolete.

SECURITY CLASSIFICATION OF THIS PAGE

Unclassified

ABSTRACT

A range of techniques have been developed for studies of the behaviour of explosives when impacted and for recording their strength, failure and ignition properties; these are described in Section 2. They include a drop-weight facility with transparent anvils, an instrumented drop-weight machine, a miniaturised Hopkinson bar system for high rate of strain property measurement, laser speckle for studies of deformation and fracture of PBX's, an automated system for analysing speckle and moiré records, and a heat sensitive film technique for recording the position and temperatures of "hot spots". The report gives data on the behaviour of a range of HMX's of different particle sizes, TATB, PBX's based on TATB (Section 2) and various propellants when impacted in the drop-weight test. In the experiments with propellants (Section 4) they were studied both at room temperature and below their glass transition temperature. At the lower temperature their flow stresses were higher and in the main they were more sensitive. Photographic evidence is presented (Section 2) of adiabatic shear band formation: measurements of band spacing and band width are compared with theoretical predictions. Section 5 and Appendices 2-4 describe our continued development of speckle and moiré techniques and their application to deformation, impact and fracture studies. Section 6 outlines research on the propagation of reaction down columns of pressed explosive and of shock/cavity interactions.

Table of Contents

1.	INTRODUCTION	2.
2.	Adiabatic shear bands	3.
2.1	Shear band model calculations	3.
3.	Impact studies on TATB based PBX's	6.
3.1	Introduction	6.
3.1	Experimental	6.
3.3	Results	6.
3.4	Discussion	6.
4.	Ignition of propellants	9.
4.1	High-speed photography	
4.2	Further deflagration experiments between glass anvils	10.
4.4	Low temperature experiments	11.
4.5	Stress-strain curves at a strain rate of 10^3 s^{-1}	13.
4.6	Conclusions	14.
5.	Laser speckle and moiré photography: Application to strength measurement and crack propagation.	16.
5.1	Introduction	16.
5.2	Summary of laser speckle photography and review of past research	16.
5.3	Recent research	17.
5.4	Improvements to instrumentation	18.
6.	Propagation down columns of explosive; shock/cavity interactions	20.
	REFERENCES	21.
	FIGURE CAPTIONS	23.
	APPENDICES	
1.	Deformation and explosive properties of HMX powders and PBX's	
2.	Speckle photography fringe analysis: assessment of current algorithms	
3.	High resolution moiré photography: application to dynamic stress analysis	
4.	Crack propagation in visco-elastic media: effect of specimen size.	

INTRODUCTION

As described in previous reports (see for example the report for 1988) a range of techniques have been developed in this laboratory for studies of the behaviour of explosives when impacted and for recording their strength, failure, and ignition properties. They include (i) a drop-weight facility with transparent anvils; this allows observation of the sample by high-speed photography throughout the impact event (ii) an instrumented drop-weight machine which is used for the determination of H₅₀'s and stress/strain behaviour at strain rates in the range 10² to 10³ s⁻¹ (iii) a direct impact Hopkinson bar of 10mm diameter to cover the strain rate range 10² to 2 x 10³ s⁻¹. It is mounted vertically which makes the positioning of the sample particularly easy, (iv) a miniaturised direct impact Hopkinson bar system for high rate of strain property measurement for the range 10⁴ to 10⁵ s⁻¹, (v) a Brazilian test apparatus which can stress disc samples of PBX's to failure at low strain rates, (vi) laser speckle and moiré techniques for studies of deformation and fracture. The speckle technique is routinely used with the Brazilian test geometry for deformation studies of PBX's. Automated techniques have been specially developed for analysing the speckle and moiré records. These have been significantly speeded up during the present grant period (a factor of 25X). The optical techniques have wide application to a range of impact and fracture situations and various studies on both explosive and inert materials are now in progress, (vii) a heat sensitive film technique for recording the position and temperature of "hot spots".

A paper describing the application of these techniques to studies of HMX of different particle sizes was presented to the 9th Symposium on Detonation at Portland (Field et al. 1989). It is reproduced here as Appendix 1.

Section 2 describes the use of the transparent anvil drop weight apparatus for studies of adiabatic shear bands. Attempts are now being made to quantify the spacing and width of the shear bands.

Section 3 describes a study of the response of TATB and PBX's based on TATB to drop-weight impact. The flow and ignition behaviour was recorded using the transparent anvil apparatus combined with high-speed photography at microsecond framing intervals.

Section 4 describes the application of the techniques to the flow and ignition behaviour of the propellants including some which were elastomer modified cast doubled-based propellants. In addition to photographic recording, use was also made of the heat sensitive film technique. The strength properties of the propellants were recorded using both the instrumented drop-weight and direct impact Hopkinson bar techniques. An innovation was to obtain data both at room temperature and at a temperature below the glass transition temperature. In general the materials became stiffer and more sensitive at the lower temperatures.

Section 5 summarises our progress with the optical techniques of speckle and moiré. These have now been applied to a wide range of deformation, impact and fracture studies. In the current period of the grant there have been significant advances in (i) combining the techniques (which give high spatial resolution) with high speed photographic recording (ii) developing faster automated techniques for analysing the speckle and moiré fringe records. Appendices 2-4 are recent publications in this area.

Section 6 summarises two new studies which we hope to develop further in future work. The first is concerned with the propagation of fast reaction in columns of explosive powder and the second is a basic study of shock/cavity interactions.

2. ADIABATIC SHEAR BANDS

The importance of localised shear as a "hot spot" ignition mechanism was first discussed by us in a paper by Winter and Field (1975). Since then we have taken many camera sequences showing the production of shear bands in impacted samples of inert materials such as polymers (Swallowe and Field 1982, Field et al. 1982), PETN and RDX (Heavens and Field 1974, Field et al 1982, Hutchinson et al 1986), HMX (Field et al. 1989) and various PBX's (Field et al. 1985 and 1989).

Figures 1 and 2 show sequences taken using the transparent anvil drop-weight apparatus and the C4 continuous access rotating mirror camera. In Figure 1 a 6.35mm diameter 2.5mm thick disc of polyether sulphone (PES) is impacted by a 5.5 kg weight falling from 1 m. Two modes of failure can be seen (i) a peripheral crack which leads to a particle separation of a piece of the polymer and (ii) shear banding.

Figure 2 shows a similar impact on a 6.35 mm diameter, 1 mm thick disc of polystyrene. The structure of the shear bands is well-defined in both these sequences.

In earlier work we have used the heat sensitive film technique and shown that high temperatures (typically of a few hundred °C) are associated with the shear bands (Swallowe et al 1986, Field et al. 1989). Related work has also shown that polymers which exhibit this mode of failure sensitise explosives (Swallowe et al. 1982, Field et al. 1982, Hutchinson et.al. 1986).

2.1. SHEAR BAND MODEL CALCULATIONS

Most model calculations have shown that if flow is uniform throughout the deforming region, very high strains are needed to produce temperatures high enough for initiation. On the other hand if the deformation is localized as in shear banding, significant temperature rise can occur. Several attempts have been made in the past to assess the temperature rise in shear bands (Frey 1981, Dienes 1986). Grady and Kipp (1987) have derived expressions for shear band spacing, width, and growth times based on a catastrophic growth model of unstable thermoplastic shear. Their expressions relate the shear band characteristics with the thermal properties of the material and the dynamic loading data. The expressions provided are as follows:

$$\text{Band width, } a_0 = \left(\frac{9\rho^3 c^2 k^3}{\tau_y^3 \alpha^2 \dot{\gamma}} \right)^{1/4} \quad (1)$$

$$\text{Band spacing, } b_0 = 2 \left(\frac{9\rho c^2 k}{\tau_y \alpha^2 \dot{\gamma}^3} \right)^{1/4} \quad (2)$$

where ρ is the density, c is the specific heat, k is the thermal diffusivity ($\lambda/\rho c$), λ is the thermal conductivity, τ_y is the flow stress, α is the thermal softening coefficient in the shear band, and $\dot{\gamma}$ is the shearing strain rate. The thermal softening coefficient α , is taken as $2.0/T_m$ since the shear stress is assumed to fall to zero at half the melting point, T_m . The flow stress, τ_y is defined as $\tau_y = 0.5Y$, where Y is the uniaxial yield stress, which in turn is related to the

Vickers Hardness value H_v , by $H_v = 3Y$. The shear strain rate $\dot{\gamma}$ is given by

$\sqrt{3}\dot{\epsilon}$ where $\dot{\epsilon}$ is the longitudinal strain rate which is related to the radial velocity, V_r , by $\dot{\epsilon} = 2V_r/r$, r being the radius of the sample.

Daja 45-89-C-0009
JEF/PB
Feb 1990

Availability Codes	
Dist	Aveil and/or Special
R-1	

Typical values for the various properties mentioned above for the different explosives considered are given in Table 1. Calculated band spacings and widths and the corresponding experimental values for the former are listed in Table 2. Calculations have been done at two strain rates viz. 2×10^5 and 10^4 / s, both being possible strain rates for drop-impact experiments.

It is evident from the results presented in Table 2 that a fair agreement exists between the calculated and experimental band spacings. It has to be pointed out here that the numbers given in Table 2 are only estimates and are meant to give an order of magnitude value for shear band spacings and widths. Only calculated bandwidths are given in Table 2 since the experimental values could not be easily ascertained from the photographs. However, the latter are somewhat higher than those predicted by equation (2). Frey (1981) has stated that the thickness of the shear region is typically less than one micron while Howe et al. (1985) have found shear cracks with widths in the range 10-100 μm in heavily confined explosive targets subjected to impact. This is an area in which we hope to do much more research.

TABLE 1. PHYSICAL PROPERTIES OF VARIOUS EXPLOSIVES

Explosive	ρ g/cc	$\alpha \times 10^3$ K ⁻¹	C J/kg.K	τ_y GPa	$\kappa \times 10^8$ m ² /s
PETN	1.78	4.84	1092.0	0.050	12.96
RDX	1.81	4.18	1192.8	0.039	5.20
HMX	1.90	3.58	970.2	0.066	27.80
Tetryl	1.71	4.96	1058.4	0.050	15.80
Picric Acid	1.76	5.06	987.0	0.050	5.80

Values taken from Dobratz (1981), Palmer and Field (1982).

TABLE 2 SHEAR BAND SPACINGS AND WIDTHS FOR DIFFERENT EXPLOSIVES

Explosive	Band spacing (μm)			Band width (μm)		
	Calculated		Experimental		Calculated	
	$2 \times 10^5/\text{s}$	$10^4/\text{s}$	Drop Impact	Particle Impact	$2 \times 10^5/\text{s}$	$10^4/\text{s}$
PETN	255	2400	250	75	0.12	0.25
RDX	237	2240	-	50	0.08	0.16
HMX	321	3030	400	-	0.20	0.46
Tetryl	260	2430	-	-	0.13	0.29
Picric Acid	193	1830	-	-	0.19	0.13

3 IMPACT STUDIES ON TATB BASED PBX's

3.1 Introduction

The impact behaviour of a variety of polymer bonded explosives based on the insensitive high explosive (IHE) Triamino-Trinitrobenzene (TATB) and two different binders, has been studied using the transparent anvil impact apparatus together with a high speed rotating mirror camera.

3.2 Experimental

Details of the PBX formulations studied are given in TABLE 3.

DETAILS OF PBX COMPOSITIONS

Composition	Constituents	Formulation / wt%
A	TATB/KEL-F800	95.0/5.0
B	HMX/HTPB-IPDI	95.0/5.0
C	TATB/HMX/HTPB-IPDI	85.0/10.0/5.0
D	TATB/HMX/KEL-F800	80.0/15.0/5.0
E	TATB/HTPB-IPDI	95.0/5.0

The C4 rotating mirror camera allows continuous access, enabling photographs to be recorded when sufficient light is available. The camera records 140 separate images during one complete revolution of the mirror. The light source is provided by a flash tube which has a typical duration of 1ms. The interframe time was about 7 μ s for all the experiments. The specimens were provided by AWE Aldermaston and consisted of small right circular cylinders, 3.81 mm in diameter by 2.0 mm thick. The specimens were impacted by a 5.5 Kg mass falling from 1 metre.

3.3 Results

Figure 3 shows a C4 sequence of the impact behaviour of Composition E (95/5 TATB/HTPB-IPDI). Twelve frames are reproduced at 28 μ s intervals. This material showed no evidence of ignition. As shown by the sequence, the sample deforms symmetrically by flowing in a radial manner. In frame 12 corresponding to 385 μ s, cracks or tears, probably caused by tensile hoop stresses acting at the periphery, are propagating towards the centre of the sample. The photographic sequence also shows that the material did not begin to undergo bulk failure until after frame 11. Measurements on the radius suggest that the material was deformed to a compressive strain in excess of 2.6 prior to cracking. Examination of the radius versus time plot, shown in figure 4, shows that by frame 12 the sample has almost stopped deforming; at this stage the anvil edges are in contact (see Field et al., 1985). Cracking occurs as the weight

rebounds. The maximum radial flow velocity is approximately 44 m s^{-1} , occurring at about $200\mu\text{s}$ after impact. The corresponding compressive strain rate is estimated as ca. $1.8 \times 10^4 \text{ s}^{-1}$.

Figure 5 illustrates the impact behaviour of composition A, (95/5 wt% TATB/KEL-F800). Twelve frames are reproduced again at $28\mu\text{s}$ intervals. This material shows evidence of cracking by frame 2 ($42\mu\text{s}$ after impact) corresponding to an estimated compressive strain of 0.55. The material expands in an asymmetrical manner with a jagged periphery from frames 2 to 7. From frame 8 on, expansion proceeds more slowly in an increasingly symmetrical manner as the drop-weight comes to rest. The maximum radial flow velocity occurs in the initial stages of impact and has a value of approximately 17 m s^{-1} . The high speed photographic sequence shows no evidence of ignition. However examination of the recovered toughened glass anvils showed evidence of scouring, indicating a low order ignition.

In composition D the TATB has been replaced by a 80/15 wt% mixture of TATB/HMX, whilst retaining the KEL-F800 binder. This material ignited under impact. The impact behaviour is shown in figure 6 where 16 frames are reproduced at $28\mu\text{s}$ intervals. The initial stages of impact are very similar to that for composition A. Cracking occurs early on, forming several quite large distinct fragments as seen in frames 6 and 7. By frame 8 comminution and compaction of the fragments leads to the formation of an increasingly symmetrical opaque layer, as shown in frame 9. Between frames 11 and 12 the compacted layer flows rapidly, with an estimated radial velocity of ca. 90 m s^{-1} . Ignition occurs on the periphery at the point labelled A in frame 13. Further possible ignition sites are labelled B in frame 15. Figure 7 shows the radius time plot for composition D.

The impact behaviour of composition C is shown in figure 8. This material is very similar to composition E, except that the TATB is replaced by an 85/10 wt% mixture of TATB/HMX whilst retaining the HTPB binder. Twelve frames are reproduced from the C4 sequence at $28\mu\text{s}$ intervals. As with composition E, this material deforms in radially symmetric manner, and comparison of its radius time plot again shown in figure 7, with that of composition E emphasizes the similarity. This material however appears to be able to withstand a higher compressive strain without cracking. As with composition E there was no evidence of ignition.

Composition B contains 95/5 wt% HMX/HTPB-IPDI, and ignited violently under impact as shown in figure 9. The corresponding radius time plot is shown in figure 10, together with that for composition E (95/5 TATB/HTPB) included for comparison. Sixteen frames from the C4 sequence are reproduced. Frames 1 to 5 are at $35\mu\text{s}$ intervals, whilst frames 6 to 16 are at $7\mu\text{s}$ intervals. From impact to about $320\mu\text{s}$, the material deforms radially with an almost constant radial velocity of 8 m s^{-1} . Between frames 3 to 6 there is a rapid expansion of the layer followed by ignition on the periphery at the point labelled A in frame 7. The remainder of the sequence shows how the reaction develops. A second more energetic ignition is shown in frame 11 at the point labelled B.

3.4 Discussion

Four TATB based PBX's with two different binder systems, HTPB-IPDI and KEL-F800 have been studied with the C4 camera when impacted. The results suggest that the formulations containing the KEL-F binder can be ignited under impact, whereas the formulations containing the HTPB binder do not ignite for the shocks produced in these experiments. The same trend was also observed for the formulations containing the TATB/HMX mixture. By comparison the HMX/HTPB formulation ignited violently when impacted.

The C4 sequences showing ignition of the explosive under impact (ie figures 6 and 9), show in each case that the compacted layer starts flowing rapidly prior to ignition. This type of behaviour has been reported previously in the impact of thin explosive layers (Heavens and Field 1974). Further work on the sensitizing effect of adding different polymers to an explosive (Swallowe and Field 1982) has shown that tough polymers which fail

catastrophically can localize energy at crack tips or in shear bands, and thereby sensitize the explosive to impact.

For the two binder systems in this work, the Kel-F800 binder is by far the tougher having an elastic modulus of 160-170 MPa compared with a value of 1-2 MPa for HTPB. It has also been shown by the use of a heat sensitive film technique, that KEL-F 800 when impacted can produce "hot spots" with temperatures of up to 460° C (Hutchinson et al. 1985). However these temperatures were obtained with samples of bulk polymer whereas in a PBX only thin layers of typically micron dimensions are present.

In view of the small quantities of polymer present in a PBX, it would appear unlikely that the production of "hot-spots" resulting from the impact deformation of the polymer is a viable mechanism for the sensitization of the explosive to impact. Another possibility may be that the inclusion of a stiff high modulus binder into a formulation, increases the probability of the compacted layer undergoing a catastrophic mechanical failure by either rapid flow or adiabatic shear, with the "hot-spots" being produced by these processes.

4. IGNITION OF PROPELLANTS

This section describes the application of our techniques to the study of the mechanical and ignition properties of a range of ten cast double-based propellants (labelled P1 to P10). Propellants P1, P2, P3, P7 and P8 were elastomer modified. P4 is a conventional CDB and P6 is a composite modified CDB. This section illustrates the type of information that can be obtained. In future work, we hope to receive a range of low vulnerability propellants from BRL.

4.1 High speed photography

(a) Circular discs

The transparent anvil drop-weight apparatus was used and a photographic sequence taken at room temperature with a 7 μ s interframe interval for each of the ten compositions. Selected frames from sequences exemplifying the four different types of behaviour identified are presented in figs 11- 14.

(i) Smooth flow. Compositions P2, P3, and P5 exhibited this behaviour. The edge becomes slightly broken at large strains (see Figure 11 for the sequence taken of P5). No ignition was seen in any of the three sequences taken.

(ii) Jagged periphery. Compositions P8, P9, and P7 showed this phenomenon. The periphery becomes very jagged in the later stages of deformation (see Figure 12 for the example of P8). No ignitions were seen for P8 and P9, but a weak ignition was seen after 637 μ s for P7.

(iii) Debonding. Two compositions (P1 and P10) do not flow uniformly but break up, the grains debonding from the binder (see Figure 13 for P1; the light bands are presumably fractures). P1 cracked at an early stage of the deformation.

(iv) Deflagration. P6 and P4 both gave rise to violent ignitions near the periphery with strong light emission. The flow up to ignition was very similar to the behaviour of those compositions described in (ii), deforming with jagged peripheries. This could be an important factor in the ignition since the fast flow could trap gas and adiabatically compress it. Fig. 14 shows this for P6. Figure 14 is a photograph of the damage caused to the glass anvils by the deflagration of composition P6.

(b) Annular specimens

In earlier research (Heavens 1973, Heavens and Field 1974 and Field et al. 1982) it was shown that some explosives were more sensitive to impact if they were in the form of an annulus. This appears to be the case with all of the propellants studied in this contract. Photographic evidence of this is given in Figures 16 - 17. Figure 16 is for P6, which also ignited in disc form. The first frame shows the annulus just before impact. The hole collapsed during the first 300 μ s. After a delay of a further 100 μ s, reaction becomes visible from an internal site near the position of the trapped gas. The reaction develops violently with the reacted products disrupting the sample. Further reaction sites form near the first one after 483 μ s and adds to the activity in this region. At 525 μ s, a reaction site develops near the top of the frame.

Figure 17 is for P7. This is a sample of the material which gave only a weak ignition site when photographed, the only occasion in five experiments when it deflagrated in solid disc form (Table 4). However, in annular form as Figure 17 shows it is much more reactive. In this sequence, there is some overwriting so that in the frame labelled 0 we see both the annulus (which has just been impacted) and the final channels through which the reaction products

escaped. This picture is instructive since it shows that the reaction grows from the position of the trapped gas.

Even compositions which never deflagrated in disc form were sensitised by the presence of the gas space (see Table 4). In all cases, the cavity collapsed completely before ignition from the centre, though in the case of P3 the time interval before completion of collapse and ignition was as short as the interframe time of the camera ($7\mu s$).

4.3 Further deflagration experiments between glass anvils

Obtaining a photographic sequence of an event is time consuming. To help improve the ignition statistics for the different compositions, a larger series of experiments were carried out using the glass anvil apparatus but without using the high-speed camera. The criteria for deciding whether a deflagration had occurred were the following: (i) loud bang heard, (ii) smell from reaction products, (iii) observation of a flash of light from the sample, and (iv) evidence of rapid flow of material across the anvils, sometimes accompanied by damage marks on the surface of the glass (see Figures 13, 16 for examples). Criteria (ii) and (iv) were the ones that were used most frequently. Table 4 summarises the data.

TABLE 4
Deflagration experiments between glass anvils

Material	Solid disc		Annulus	
	No. of drops	No. of deflagrations	No. of drops	No. of deflagrations
P1	5	0	3	3
P2	5	0	3	3
P3	5	0	4	4
P4	10	1	3	3
P5	5	0	3	3
P6	5	3	8	8
P7	5	1	8	8
P8	5	0	3	3
P9	5	0	3	2
P10	5	0	3	3

In solid disc form, only 3 compositions ignited. P6 ignited in three tests out of five and the photographic sequence shown in Figure 14 shows that it reacted violently. P4 showed a violent reaction when photographed but failed to ignite in 9 further experiments! P7 was a material which ignited weakly when photographed, but again ignition was a rare event.

The much greater sensitivity of samples in annular form is apparent from the data: only P9 was ever observed not to ignite, and that in only one test out of three.

4.4 Low temperature experiments

(a) Method

Five of the compositions were elastomer modified cast double base propellants (EMCDBs) and thus exhibit a glass transition temperature (T_g). These were: P1, P2, P3, P7, and P8. Three of our techniques outlined have been applied to this problem: (i) high speed photography with and without heat sensitive film, (ii) steel anvil dropweight apparatus with and without heat sensitive film, and (iii) intermediate strain rate direct impact Hopkinson bar.

The specimens to be tested were cooled by immersing them in liquid nitrogen. This had to be done slowly and carefully; just dropping the discs into the coolant resulted in them fracturing, the fragments often flying apart at quite high speeds due to locked in thermal stresses. So the discs were held in the cold vapour above the liquid for about a minute to cool them down slowly before dropping them into the bath. Experiments were performed using a thermocouple to see how quickly the discs warmed up after they were removed from the cryogenic environment. We found that after only 10 s they had reached the glass transition temperature (ca. -65°C) and after a further 10 - 20 s, room temperature was achieved. Thus it can be seen that tests have to be performed quickly after removal from the coolant! This was fairly easy to achieve with the steel anvil and direct impact Hopkinson bar apparatuses, but added to the already considerable problems of taking high speed photographs.

Several alterations were made to the transparent anvil drop-weight apparatus in order to make high speed photography possible below T_g . First it was clear that because the camera mirror takes considerably longer than 10s to come up to speed, a way had to be found of keeping the specimen cool. This was achieved by constructing a paper collar around the anvil to form a temporary liquid nitrogen bath into which the specimen could be placed. It was soon discovered that it was not adequate merely to cool the lower anvil; it had to be taken all the way down to -196°C in order that the liquid nitrogen became quiescent, as the discs are sufficiently light to be knocked around by the boiling liquid. This meant in turn that the lower surface had to be dry and in contact with very dry air, else it rapidly frosted over making photography impossible. The space below the anvil can be easily sealed and hence dried out using a boat containing phosphorus pentoxide.

(b) Results

High speed photographic sequences of the deformation of the five EMCDB compositions deforming at liquid nitrogen temperatures have been taken and two are illustrated in Figures 18 and 19. All deformed in a brittle fashion, disintegrating into a powder soon after impact. Two of the compositions (P1 and P7) were observed to deflagrate strongly (Figure 19 is an example), in marked contrast to their behaviour at room temperature. The high speed sequences for the other three that did not deflagrate nevertheless show evidence of the evolution of a small quantity of gaseous products in that part way through, some of the powder moves very rapidly in what appears to be a plume. Figure 19 gives the clearest evidence so far for the postulated mechanism of ignition caused by gas being trapped by a jagged periphery. The gas space is clearly seen in the frame labelled 400 μ s. It disappears from view by the time 696 μ s have passed, but the deflagration event starting at 704 μ s begins where the gas space was, and rapidly consumes the sample.

High speed photographic sequences were also obtained for specimens of P1 below its glass transition temperature in the presence of heat sensitive film. The procedure adopted was different for the case when film was present because the physical and chemical properties of the heat sensitive film would be significantly altered if cooled to liquid nitrogen temperatures. It proved to be possible to place the cold specimen on the anvil with the camera mirror at full speed and immediately release the dropweight so that impact occurred before the specimen warmed up. Figure 20 illustrates the early stages of impact. There is very little radial

expansion of the disc before fragmentation starts at the circumference as can be seen in the first four frames. In the following frames, individual angular fragments move radially outwards with velocities of ca. $35 - 40 \text{ m s}^{-1}$. During this time, the material in the centre of the field of view expands more slowly at ca. 17 m s^{-1} , and the larger fragments comminute further and start compacting together to form an opaque layer. This can be seen clearly in the top left of frames 9 - 12. There was no indication of deflagration either from the high speed photography, or from the sound of a crack, or from discolouration of the film. This sequence ended close to the last frame presented, so further drops were performed to try to capture events happening later on in the deformation. Figure 21 starts at $455 \mu\text{s}$ (the early frames are very similar to those in Figure 20, and are thus not presented). In frames 1- 6, the larger angular fragments are undergoing further comminution and the layer is expanding at ca. 25 m s^{-1} . Between frames 7 and 8, part of the layer in the lower right hand side of the field of view starts to flow rapidly with a velocity of at least 43 m s^{-1} . The white arrow in frame 8 points to two ignition sites that are just visible. Frame 9 shows deflagration starting as indicated by the arrow, whilst successive frames at $7 \mu\text{s}$ intervals show material being displaced by the deflagration products. The recovered heat sensitive film for this sample showed clear evidence of discolouration.

Table 5 gives the frequency of ignition data for the steel anvil apparatus with a layer of heat sensitive film present. Force-time traces obtained from samples of compositions P1 and P8 below their glass transition temperatures along with pictures of the associated discoloured heat sensitive films are presented in Figures 22 - 24. Ignition was known to have occurred if there was a sharp crack and a pungent smell.

Three samples of P8 were tested and an example is given in Figure 22, where there was a sufficiently violent deflagration to scour away part of the emulsion in the shape of a rough segment. This strongly suggests that deflagration started close to the centre of the sample. The associated force-time plot shows two rapid pressure drops, the second one being much greater than the first, followed by a sinusoidal trace as the weight loads the anvil elastically and rebounds.

In the case of P1, again three samples were tested below their glass transition temperature, and for comparison one was also deformed at room temperature (Figure 25). The first one ignited giving an odour but no bang. The film showed discolouration in the centre and at the end of the region scoured by the deflagration. The force-time plot showed a drop of ca. 10 kN during the loading phase of the impact. The second (Figure 23) ignited very violently with a loud crack and pungent smell. The film was extensively damaged, even to the extent of having a hole punched through it. The remaining film is intensively discoloured. The force-time trace shows a particularly large rapid drop of ca. $20 - 25 \text{ kN}$. The third (Figure 24) also ignited, and this time the film had two areas where the emulsion was scoured away surrounded by intense discolouration. The right hand horizontal arrow shows a region of the heat sensitive film where there are faint parallel lines of discolouration which may be indicative of adiabatic shear bands. This suggests there were two separate ignition sites. It is interesting to note that there are two large force drops in the strain gauge output. The sample tested at room temperature (Figure 25) did not ignite. However, the heat sensitive film shows quite clearly two areas close to the periphery where high temperatures were obtained. This was in the absence of rapid force drops or fluctuations.

TABLE 5
Experiments with heat sensitive film on specimen
behaviour above and below T_g for the elastomer modified
propellants

Material	Room temp.		Low temp.	
	No. of drops	No. of deflagrations	No. of drops	No. of deflagrations
P1	1	0	6	4
P2	1	0	3	0
P3	2	1	2	2
P7	1	0	1	1
P8	1	0	4	2

4.5 Stress-strain curves at a strain rate of 10^3 s^{-1}

Two different apparatuses were used to determine the mechanical behaviour of the various propellant compositions quantitatively at high strain rates. The first was a Direct Impact Hopkinson Bar (DIHB). The impact bar falls from a height of 1m giving a strain rate of $2 \times 10^3 \text{ s}^{-1}$ with a specimen of 2mm thickness. It is designed to measure the impact conditions and force output with an accuracy of 1% from any given test. The main sources of error and variability between runs arise from shape differences between specimens, particularly deviations from the assumed geometry of a right circular cylinder (the micrometer used is accurate to ca. $5\mu\text{m}$) and a certain amount of subjectivity about determining the zero point for starting the integration to calculate stress and strain. The second apparatus is an instrumented drop-weight machine. This is inherently a less accurate machine than the DIHB as the strain gauges are positioned closer to the end of the steel roller than is desirable for the strains to obey St. Venant's principle and be independent of the loading profile on the ends. It has the advantage, however, of a much longer time window for recording data (2ms as opposed to $300\mu\text{s}$) and it also has the ability to apply greater loads. This was particularly an advantage when testing compositions below their glass transition temperatures. The strain rates it is normally used to apply are slightly lower: $7 \times 10^2 \text{ s}^{-1}$ to 10^3 s^{-1} .

A summary of the peak stresses obtained for the various compositions is presented in Table 6.

TABLE 6

Peak stresses (MPa) obtained at room temperature using a direct impact Hopkinson bar at strain rates of $2 \times 10^3 \text{ s}^{-1}$ and at low temperatures using a dropweight machine at strain rates of $1 \times 10^3 \text{ s}^{-1}$

Material	Room Temp.	Below T_g	Ratio
P1	70 ± 8	450 ± 100	6.5
P2	35 ± 5	750 ± 100	21.5
P3	50 ± 20	600 ± 100	12
P4	70 ± 5	-----	---
P5	35 ± 5	-----	---
P6	60 ± 8	-----	---
P7	35 ± 5	900 ± 400	26
P8	45 ± 5	600	13
P9	60 ± 8	-----	---
P10	40 ± 5	-----	---

4.6 CONCLUSIONS

(a) Room temperature behaviour

In general, the strengths of the propellants are lower than the PBX's we have studied before (Field et al. 1985), but they exhibit much larger strains. For example, various HMX based PBX's with different binders had ultimate compressive strengths (UCS's) at a strain rate of 10^2 s^{-1} in the range 20 to 70 MPa and at a strain rate of 10^4 s^{-1} in the range 70 to 150 MPa. The peak stresses at a strain rate of 10^4 s^{-1} were at strains less than 0.05.

The Hopkinson bar data on the propellants were obtained at a strain rate of $2 \times 10^3 \text{ s}^{-1}$. Stress values at a strain of 0.6 were typically 40 to 70 MPa, while at a strain of 0.1 they were 6 to 18 MPa. Drop-weight experiments at room temperature showed that load drops seen with the DIHB for compositions P4, P6, P8, and P9 were genuine and that therefore mechanical failure at this temperature is a possible source of ignition, but note that only one of these four compositions is an EMCDB (P8).

The amount of energy absorbed is, of course, proportional to the area under the stress-strain curve. The fact that the propellants have only marginally lower strengths but exhibit **much** greater strains at failure (or ignition) means that the energy absorbed (and therefore the bulk heating) is greater than for PBX's.

High speed photography of PBX's igniting (Field et al. 1985) has shown that they did so after a pressure drop associated with the onset of plastic flow. Evidence for ignition at adiabatic shear bands was found.

The high speed sequences in this report showed that ignition (unlike the PBX's) occurred after extensive flow and near the periphery. Propellants which ignited fell into the category of those which flowed and produced a jagged periphery. As discussed in an earlier paper (Field et al. 1982) this kind of flow traps gas. In that paper, it was also emphasised that "hot spot" temperatures were often achieved by additive processes. We suggest that the mechanism of ignition with the propellants is the addition of bulk heating (large because of the large strains involved) plus viscous heating (the anvils are very close at the time of ignition so that material flows through a narrow channel) plus adiabatic heating of trapped gas at the periphery. This explanation is reinforced by the considerably greater sensitivity of impact onto annular propellant specimens.

(b) Low temperature experiments

This appeared to sensitise the materials. Ignition occurred at lower strains but since the stresses were much higher the area under the stress-strain curve would remain large. Similar mechanisms are thought to be responsible for ignition as for those at room temperature.

The instrumented drop-weight showed that there is a strong correlation between discolouration of the heat sensitive film and the presence of rapid and large force drops in the force-time data. In particular, these force fluctuations appear to be particularly pronounced for those samples which ignited violently.

The high speed photographic studies of the deformation behaviour of propellants below their glass transition temperature show three main stages. Initially fragmentation of the sample occurs producing fragments which move radially with speeds ca. 40 m s^{-1} . The second stage consists of comminution of the larger fragments and compaction to form a layer. In the final stage, the layer expands at speeds of ca 25 m s^{-1} . However, part of the expanding layer may flow much more rapidly, in which case ignition may result from frictional heating as material is extruded through the narrow gap between the anvils. Another mechanism which could be responsible for the localization of the impact energy to form hot-spots and hence ignition sites is by means of adiabatic shear. This mechanism is more likely to occur in situations where the material behaves in a more brittle manner, for example when the propellants are deformed below their glass transition temperature. The heat sensitive film technique shows evidence of faint parallel lines of discolouration which may be interpreted as evidence of adiabatic shear occurring in the vicinity of an ignition site.

The combination of high speed photographic studies and the instrumented drop-weight results suggests that the rapid load drops observed in the force-time data are probably due to the onset of rapid flow by either the whole or part of the layer of compacted material. This explanation may also account for the observed correlation between load drops in the force-time data and the discolouration of the heat sensitive film. Unfortunately with the present instrumented apparatus, it was not possible to determine when ignition occurred.

5. LASER SPECKLE AND MOIRE PHOTOGRAPHY: APPLICATION TO STRENGTH MEASUREMENT AND CRACK PROPAGATION

5.1 Introduction

The distribution of strain in a material or engineering component can be measured by a wide range of techniques. The resistance strain gauge is commonly used where strain values are required at a few isolated points; when wholefield information is required, optical techniques such as photoelasticity, caustics, holographic interferometry, moiré photography and speckle photography become more useful. Each technique has its advantages and disadvantages: the use of photoelasticity, for example, is relatively straightforward and easily extended to the study of dynamic events, but is restricted to a few transparent materials which exhibit the photoelastic effect. Our research into optical techniques over the past few years has been associated with two major projects: measurement of the strength and strain-to-failure of filled polymers, particularly polymer bonded explosives (PBXs); and measurement of dynamic strain fields, with applications in impact phenomena and dynamic fracture.

In the case of low modulus materials like PBXs, strain gauges have the drawback of tending to reinforce the specimen, and a non-contacting optical technique is therefore preferable. Safety considerations limit the size of the test specimen to dimensions of the order of mm, so the technique must have high sensitivity; a further consequence is that the test should make economical use of the available material. We have found laser speckle photography, used in conjunction with the Brazilian test (disc under diametral compression), to be a good combination for these experiments. The main drawback of laser speckle is the time taken to extract displacement information from the speckle photographs, and recent work on automatic image processing techniques is presented in the report.

Laser speckle photography is difficult to apply to dynamic events, and so a high resolution moiré technique has been developed for measuring strain fields with microsecond time resolution. The technique and associated image processing algorithms are described in this section.

The final piece of new research reported here concerns the propagation of a crack in a viscoelastic material. The strain energy release rate required to extend the crack is calculated as a function both of the crack speed, and of the macroscopic specimen dimensions. This size effect could have relevance to the understanding of fracture mechanisms in PBXs.

5.2 Summary of laser speckle photography and review of past research

The conventional double exposure laser speckle technique was first proposed by Burch and Tokarski (1968) working at the National Physical Laboratory. The specimen to be deformed is photographed by the light of a laser beam. The film is exposed twice: once before, and once after the deformation. Light is scattered from surface features of the specimen to create a fine random speckle pattern in the image plane. The speckles move with the scattering surface, so that when the film is developed, the image is found to be covered, in effect, by a random array of speckle pairs. The in-plane displacement vector of any point on the specimen can be obtained by measuring the speckle displacement vector at the corresponding point on the film. This is normally done by probing the photograph with a narrow laser beam. A diffraction pattern is formed which is similar to that from a mask containing two small apertures, and is therefore commonly called the "Young's fringes" pattern. The displacement vector can be deduced from the spacing and angle of the Young's fringes. The laser beam is then moved to another region of the photograph and the fringe pattern measured in the same way; this process is repeated until the complete 2-D displacement field has been mapped out. A single photograph might require upwards of several hundred such measurements, and the procedure becomes impractical when performed manually. For this reason, we have built an image processing

system (Huntley 1986a) and developed fringe analysis algorithms (Huntley 1986b, Huntley 1986/7, Huntley and Field 1986b) which allow the analysis to proceed completely automatically.

The image processing system (Huntley 1986a) consists of a linear photodiode array interfaced to a microcomputer. The speckle photograph is mounted on a stepper-motor-driven X-Y translation stage so that the computer can digitise the fringe pattern from any point on the photograph. Fourier spectral analysis is then used to process the image. With good quality fringe patterns, the system measures the speckle displacement to an accuracy of better than 50 nm. Acquisition and analysis of the fringe pattern, and translation of the photograph to the next point of interest, takes under 10 s; measurement of the displacement field from one photograph on a typical mesh of 16x16 datapoints therefore requires around 40 minutes. This system is now six years old, and is currently being substantially upgraded as described in section 5.4.

The use of Walsh spectral analysis as an alternative to Fourier transformation was investigated by Huntley (1986b). The advantage of the Walsh transform is that it requires no multiplications, and can therefore be computed more rapidly: a speed improvement by a factor of three times was obtained on a Z80 microprocessor. The performance of the two techniques, in terms of reliability and random errors, was shown to be essentially identical (Huntley 1986/7).

In the paper by Huntley and Field (1986), multiple exposure speckle photography was proposed as a method for measuring time-varying displacement fields. The film is exposed a number of times (up to ten exposures), instead of just twice as with conventional speckle photography. It was shown that, provided a shifted reference speckle pattern was also recorded on the film, the fringe patterns produced by pointwise probing of the developed photographs contained enough information to allow the displacement field at the time of each exposure to be reconstructed. With a strobed laser light source, this technique could be used to measure dynamic displacement fields without the need for a high speed camera.

Applications of the instrumentation include strain measurement of PBXs under load in the Brazilian test (Huntley et al. 1987) and measurement of the displacement field around a crack tip under both quasi-static and dynamic loading (Huntley and Field 1988a,b). These results have been described in detail in previous reports.

5.3 Recent Research

We describe in this section research into optical strain measurement techniques completed since the last report (August 1988). As discussed in the introduction, the research consists of three sub-sections which are presented here as Appendices 2-4.

In Appendix 2, the accuracy and reliability of four algorithms for analysing the Young's fringe patterns from a double exposure speckle photograph are compared. A total of 320 fringe patterns were used in the test; these were calculated from computer-generated speckle patterns to allow the effects of parameters such as fringe visibility (V), speckle diameter (σ) and radius of the laser probe beam (R) to be studied in a systematic manner. The Appendix describes in detail the generation and characterization of the fringe patterns. It was found that the random errors from all four algorithms vary in proportion to σ^2/VR , with the lowest errors given by the original 2-D Fourier transform method (Huntley 1986a)

Appendix 3 describes the development of the technique of high resolution moiré photography for measuring simultaneously both in-plane components of a dynamic displacement field. In experimental mechanics, the moiré technique refers to the superimposition of two line gratings: one is attached to the specimen (specimen grating), the other stationary (reference grating). A fringe pattern is formed which is essentially a contour map of the in-plane displacement component perpendicular to the grating lines, with a contour interval equal to the specimen

grating pitch. The superimposition is achieved in this case by imaging the specimen onto the reference grating with a specially modified lens, forming real-time fringes which are recorded by a high speed image converter camera. The lens modifications allow good contrast fringes to be recorded at a grating frequency of 150 lines mm^{-1} , around four times the maximum normally feasible with conventional moiré photography. The fringe patterns are analysed automatically by a Fourier transform method, which converts the intensity distribution into a map of the fringe phase variation. The phase values at this stage are wrapped onto the range 0 to 2π ; the process of phase unwrapping (removing the 2π discontinuities) produces a phase map which is directly proportional to the relevant displacement component. Phase unwrapping in 2 dimensions is not a straightforward process, however: noise in a small region of the image can produce inconsistencies that propagate across the phase map, causing unwrapping errors in regions well away from the corrupted data. A new noise-immune phase unwrapping algorithm has therefore recently been proposed which is based on the requirement that the unwrapped map should be independent of the route by which unwrapping takes place (Huntley 1989). This is achieved by placing strategic cut lines which act as barriers to unwrapping. Although this new algorithm has so far only been applied to moiré fringe patterns, phase unwrapping has become a fundamental process in many fringe analysis techniques, and it is expected that the algorithm will be used extensively in the moiré and speckle interferometry experiments proposed in section 5.4. The high resolution moiré technique is illustrated in Appendix 3 by results showing the transient deformation caused by solid particle impact on polymethyl methacrylate.

Appendix 4 is a theoretical analysis of the strain energy release rate, G , required to propagate a mode I crack through a strip of viscoelastic material. The Griffith criterion $G = 2\gamma$ (where γ is the intrinsic fracture surface energy) represents the condition for an equilibrium crack. In a viscoelastic material, stable crack growth can occur at larger values of G , with viscoelastic losses absorbing the surplus energy ($G - 2\gamma$). In many elastomers, G can exceed 2γ by a factor of 10^3 or more, even at crack speeds as low as a few $\mu\text{m s}^{-1}$. It is clearly important to be able to explain and predict such large variations in effective fracture surface energy in order to understand, for example, the strength properties of PBXs. It was found that G can be approximated by the expression $2\gamma C(h/V)/C(l/V)$, where $C(t)$ is the creep compliance function, h is the strip half-width, l is the Barenblatt or Dugdale zone length, and V is the crack velocity. The analysis predicts a region of the G - V curve having negative gradient, providing a possible explanation for the instability phenomena observed in the fracture of some polymers. The critical point (G_c, V_c) at which $dG/dV = 0$, is dependent on h , with wide strips having greater apparent fracture surface energy than narrow ones. Although these predictions still have to be confirmed by experiment, it suggests a means of applying fracture surface energy data obtained in macroscopic tests, to binder layers in a PBX which are typically of sub-micron thickness.

5.4 Improvements to instrumentation

We are currently upgrading our image processing system: the mechanically scanned image digitiser will be replaced by a 2-D CCD array, allowing digitisation at TV framing rates; and a new computer will also be installed. As well as speeding up the analysis of speckle photographs, the new system will be sufficiently flexible to allow the implementation of two alternatives to laser speckle photography: laser speckle interferometry and moiré interferometry.

Speckle interferometry has in the past been combined with image processing equipment in a technique commonly called Electronic Speckle Pattern Interferometry (ESPI). An ESPI system produces real-time fringes, representing contours of constant phase change due to the deformation, and can measure in- or out-of-plane displacement, depending on the geometry of the illumination system. Although useful for rapid qualitative evaluation of deformation or vibration, the very high noise level in the fringes means the system is not well suited to automatic quantitative measurements. A method of measuring the phase changes directly has recently been proposed by Creath (1985). This relies on stepping the phase of one of the

interfering beams through known increments; three phase-shifted interferograms are sufficient to determine the phase distribution of the speckle field uniquely. The specimen is then deformed and three more interferograms are digitised, from which the phase map of the deformed state is extracted. The difference between these two maps is then proportional to the relevant displacement component. Phase-stepping interferometry is superior to ESPI for quantitative measurements because the information is presented as maps of phase rather than intensity. These maps are still noisy, however, because of speckle effects and it has been suggested that shifting of the specimen beam could be used to produce a number of phase maps; these would then be averaged to reduce the noise. The technique looks promising, and is worth investigating for wholefield strain measurements on PBXs. It would allow the data analysis to be carried out during the experiment, without the need for a separate process as is required with the speckle photography technique.

Moiré interferometry involves attaching a fine reflective phase grating to the surface of the specimen. The specimen is illuminated by two beams (arranged symmetrically about the normal to the specimen); interference between the two first order diffracted beams produces a real-time moiré fringe pattern which can be recorded with a camera, or digitised. The phase stepping technique described above is also applicable here. Both speckle and moiré interferometry give the same information (i.e. one displacement component), but the moiré data is much less noisy than that from speckle. The drawback is that a grating needs to be attached to the specimen surface. We would expect that speckle interferometry would be most useful in routine testing of large numbers of samples, whereas the moiré technique might be more appropriate in specialised situations such as microstructural investigations.

A thorough review of the image processing equipment market has been carried out by H. T. Goldrein (a new research student in the group), bearing in mind the applications outlined above. A final system has been selected comprising a Sun 386i workstation; Digital Imaging Systems framestore (DIS3000); and EEV photon camera. The framestore has four image planes, each of 512x512 pixels, with 8 bits per pixel. The particular combination of camera and framestore allows clocking of the CCD data, pixel by pixel, directly into the framestore memory, thereby eliminating pixel jitter which can cause noise in a speckle interferometry experiment. The Sun computer has similar processing power to a top-of-the-range IBM AT compatible, but the amount of memory available to a program is not limited to the 640 kbyte accessible under MS-DOS. This is a considerable advantage for image processing work, both in terms of ease of programming and efficiency of execution. The framestore can also be addressed over a VME bus, allowing a more powerful computer to be installed at a later date, if required (e.g. a Sun SPARCstation). An IEEE interface will also be installed to allow control of an experiment, and instrumentation of the sample under test. The system was ordered in January 1990.

6. PROPAGATION DOWN COLUMNS OF EXPLOSIVE; SHOCK/CAVITY INTERACTIONS

A study has recently been completed for RARDE, Fort Halstead on the ignition and propagation of fast reaction in the primary explosives mercury bisfulminate, silver-s-nitrotetrazole and mercuric-s-nitrotetrazole as a function of pressed density. Observation of propagation down pressed columns was by both high-speed framing photography at sub micro-second framing rates and by streak photography. A variety of test pieces either made entirely from polycarbonate (PC) or with metal confinement with a PC "window" were used.

The main objective of this research was to investigate the factors which affect DDT and the related phenomena of dead-pressing, which may be regarded as a failure of dead-pressing at high pressed densities. Factors studied included press density, grain size distribution, void structure, confinement and initiating stimulus. A paper was presented at the 9th Symposium (Int) on Detonation (Dickson et al. 1989). New research is concerned with DDT of secondary explosives.

This laboratory has had a long interest in cavity collapse as an ignition mechanism (Bowden and Yoffe 1952, Chaudhri and Field, 1974). Recent work was described at the 9th Symposium (Int) on Detonation, (Bourne and Field 1990).

The collapse of large (1-12mm) cavities formed within inert gelatine slabs and sheets of an emulsion explosive, have been studied using high-speed framing photography and employing a schlieren technique. The cavities were punched, and in some cases solid particles were cast into sheets, that were then sandwiched between transparent blocks. This allowed processes occurring within and around the cavity to be recorded. Shocks were introduced by impact from a metal flier-plate or directly from an explosive plane wave generator. The assymmetric collapses of circular cavities was observed in which a high-speed liquid jet crossed the cavity and impacted on the downstream wall. Perturbations to the direction of jet travel and to the convection of the collapse site in the flow were caused by adjacent solid particles. Regions of high temperature within the collapsing cavity appeared as areas of gas luminescence. The development of reaction sites around collapsing bubbles in an emulsion explosive was photographed.

This research is being continued.

REFERENCES

- Bourne, N K, Field J E (1989) Proc 9th Symp (Int) on Detonation, Portland, Oregon, Paper No 88.
- Bowden F P and Yoffe A D First Edition, Cambridge University Press, Cambridge, 1952.
- Burch J.M. and Tokarski J.M.J. 1968, Opt. Acta. **15**, 101 China, Sept. 1988.
- Creath K., 1985, Appl. Opt. **24**, 3053.
- Dickson P M, Parry M A and Field J E (1989) Proc 9th Symp (Int) on Detonation, Portland, Oregon, Paper No 87.
- Dienes, J K Phys Letters A, Vol 118, No 9, 1986, p 433.
- Dobratz, B M, LLNL Explosives Handbook, UCRL 52997, Lawrence Livermore National Laboratory, 16 March 1981, p 231.
- Field J.E., Palmer S.J.P., Pope P.H., Sundarajan R. & and Swallowe G.M. - 1985. *Proc. 8th Int. Symp. on Detonation*, Albuquerque, U.S.A.
- Field J.E., Swallowe G.M. & Heavens S.N. - 1982, *Proc. Roy. Soc. Lond. A* **382** 231
- Field, J E, Palmer S J P, Pope J H, Sundararajan, R and Swallowe, G M in proceedings of the Eighth Symposium (International) on Detonation, Albuquerque, pp 635-644.
- Frey, R B in proceedings of the Seventh Symposium (International) on Detonation, Maryland, 16 June, 1981, pp 36-42.
- Grady D E and Kipp M E J Mech Phys Solids Vol 35, 1987, p 85.
- Heavens S.N. & Field J.E. - 1974, *Proc. Roy. Soc. Lond. A* **338** 77
- Heavens S.N. - 1973, PhD Thesis, University of Cambridge
- Howe, P M, Gibbon G, and Webber P E in Proceedings of the Eighth Symposium (International) on Detonation Albuquerque, 15 July 1985, pp 294-301.
- Huntley J.M. 1986/7, Opt. Lasers Eng. **7**, 149
- Huntley J.M. 1986a, J. Phys. E: Sci Instrum. **19**, 43
- Huntley J.M. 1986b, Appl. Opt. **25**, 382
- Huntley J.M. and Field J.E., 1986, Appl. Opt. **25**, 1665
- Huntley J.M. and Field J.E., 1988a, Eng. Fract. Mech. **30**, 779
- Huntley J.M. and Field J.E., 1988b, Proc. Intl. Conf. High Speed Photography, Xian
- Huntley J.M., 1989, Appl. Opt. **28**, 3270.
- Huntley J.M., Palmer S.J.P. and Field J.E., 1987, Proc. SPIE **814**, 153

Palmer, S J P and Field, J E Proc Roy Soc Lond, Vol A383, 1982, p 399.

Swallowe G.M. & Field J.E., *Proc. Roy. Soc. Lond. A* **379** 389

Winter, R E and Field, J E, Proc Roy Soc, Vol A343, 1975, P 399.

FIGURE CAPTIONS

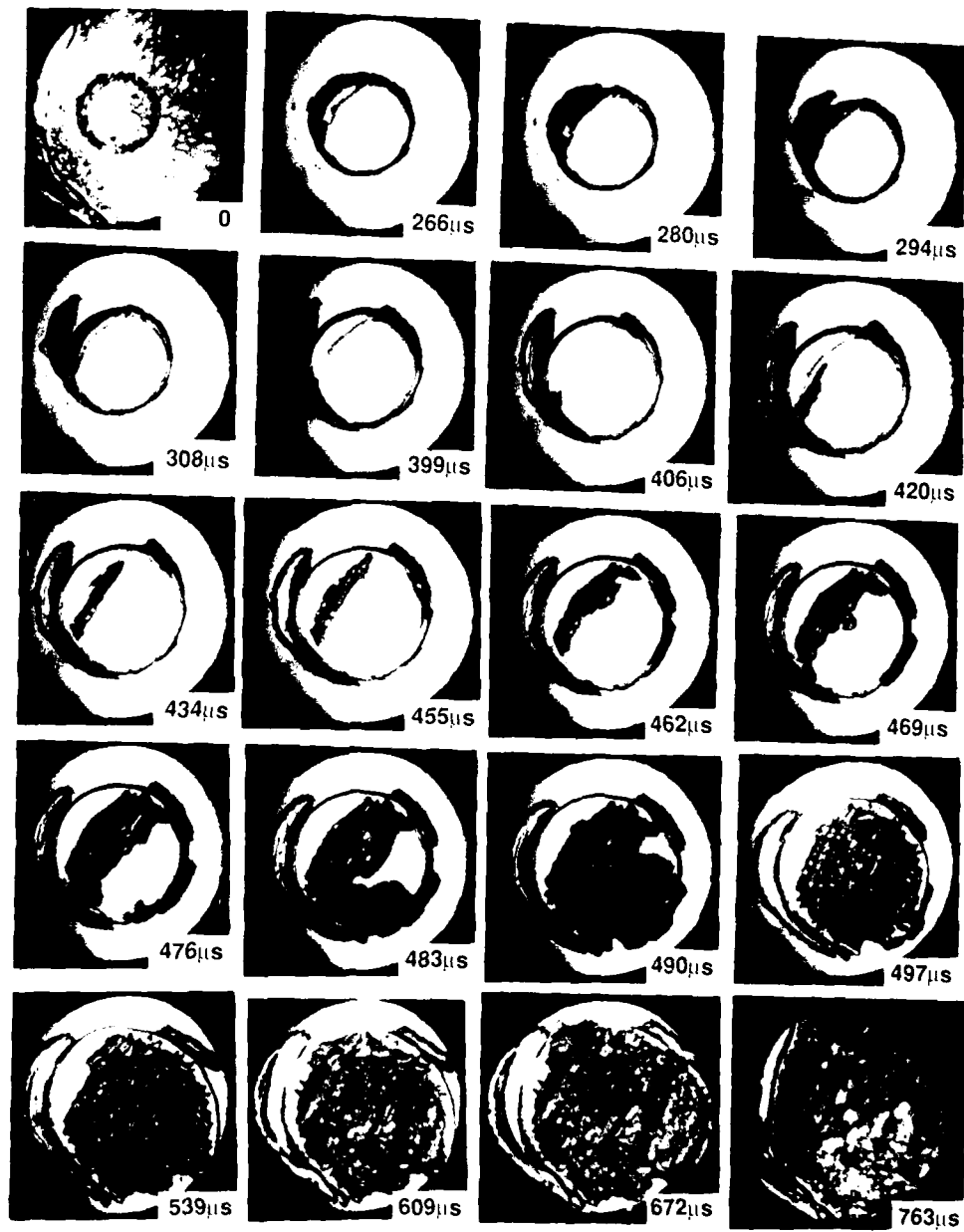
- Fig. 1 C4 sequence of the unlubricated deformation of a disc of PES.
- Fig. 2 C4 sequence of the unlubricated deformation of a disc of PS.
- Fig. 3 C4 sequence showing the impact of Composition E 95/5wt% TATB/HTPB-IPDI
- Fig. 4 Radius time plot for Composition E
- Fig. 5 C4 sequence showing the impact of Composition A 95/5wt% TATB/KEL-F800
- Fig. 6 C4 sequence showing the impact of Composition D 80/15/5wt% TATB/HMX/KEL-F800
- Fig. 7 Radius time plots for Compositions C and D
- Fig. 8 C4 sequence showing the impact of Composition C 85/10/5wt% TATB/HMX/HTPB-IPDI
- Fig. 9 C4 sequence showing the impact of Composition B 95/5wt% HMX/HTPB-IPDI
- Fig. 10 Radius time plot for Composition B. Composition E is included for comparison.
- Fig. 11 Selected frames from a high speed photographic sequence of the deformation of a solid disc of P5.
- Fig. 12 Selected frames from a high speed photographic sequence of the deformation of a solid disc of P8.
- Fig. 13 Selected frames from a high speed photographic sequence of the deformation of a solid disc of P1.
- Fig. 14 Selected frames from a high speed photographic sequence of the deformation of a solid disc of P6.
- Fig. 15 Photograph of a glass anvil after impact on a solid disc of P6.
- Fig. 16 Selected frames from a high speed photographic sequence of the deformation of an annulus of P6.
- Fig. 17 Selected frames from a high speed photographic sequence of the deformation of an annulus of P7.
- Fig. 18 Selected frames from a high speed photographic sequence of the deformation of a solid disc of P2 deforming below its glass transition temperature.
- Fig. 19 Selected frames from a high speed photographic sequence of the deformation of a solid disc of P7 deforming below its glass transition temperature.
- Fig. 20 Selected frames from a high speed photographic sequence showing the early stages of the deformation of a solid disc of P1 below its glass transition temperature and in contact with a piece of heat sensitive film.
- Fig. 21 Selected frames from a high speed photographic sequence showing the later stages

of the deformation of a solid disc of P1 below its glass transition temperature and in contact with a piece of heat sensitive film. Ignition occurred in this sequence.

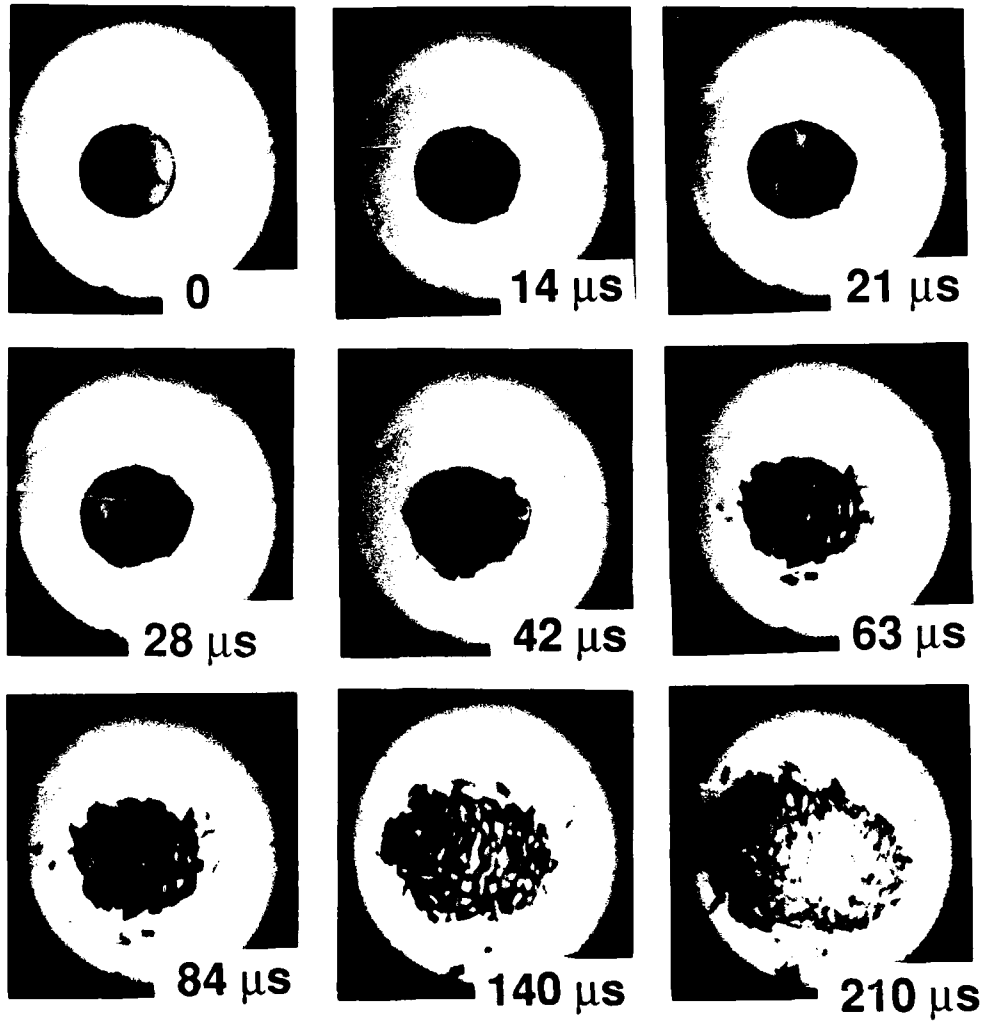
- Fig. 22 Heat sensitive film recovered from the steel anvil dropweight apparatus after a specimen of P8 below its glass transition temperature had been impacted by a 2.4kg mass dropped from a height of 20cms. The arrow shows where ignition started.
- Fig. 23 Heat sensitive film recovered from the steel anvil dropweight apparatus after a specimen of P1 below its glass transition temperature had been impacted by a 2.4kg mass dropped from a height of 20cms. Sample ignited violently punching a hole in the film. Note the discolouration indicating high temperatures at the edge of the sample (arrowed).
- Fig. 24 Heat sensitive film recovered from the steel anvil dropweight apparatus after a specimen of P1 below its glass transition temperature had been impacted by a 2.4kg mass dropped from a height of 20cms. This sample ignited in two places which are indicated by the black arrows. Close examination of the region indicated by the right-hand arrow shows faint parallel lines of discolouration possibly due to adiabatic shear bands.
- Fig. 25 Heat sensitive film recovered from the steel anvil dropweight apparatus after a specimen of P1 at room temperature had been impacted by a 2.4kg mass dropped from a height of 20cms. There was no evidence of ignition. However, the heat sensitive film shows two regions (labelled (a) and (b)) close to the edge where high temperatures were obtained.

APPENDICES

1. Deformation and explosive properties of HMX powders and PBX's.
2. Speckle photography fringe analysis: assessment of current algorithms.
3. High resolution moiré photography: application to dynamic stress analysis.
4. Crack propagation in visco-elastic media: effect of specimen size.

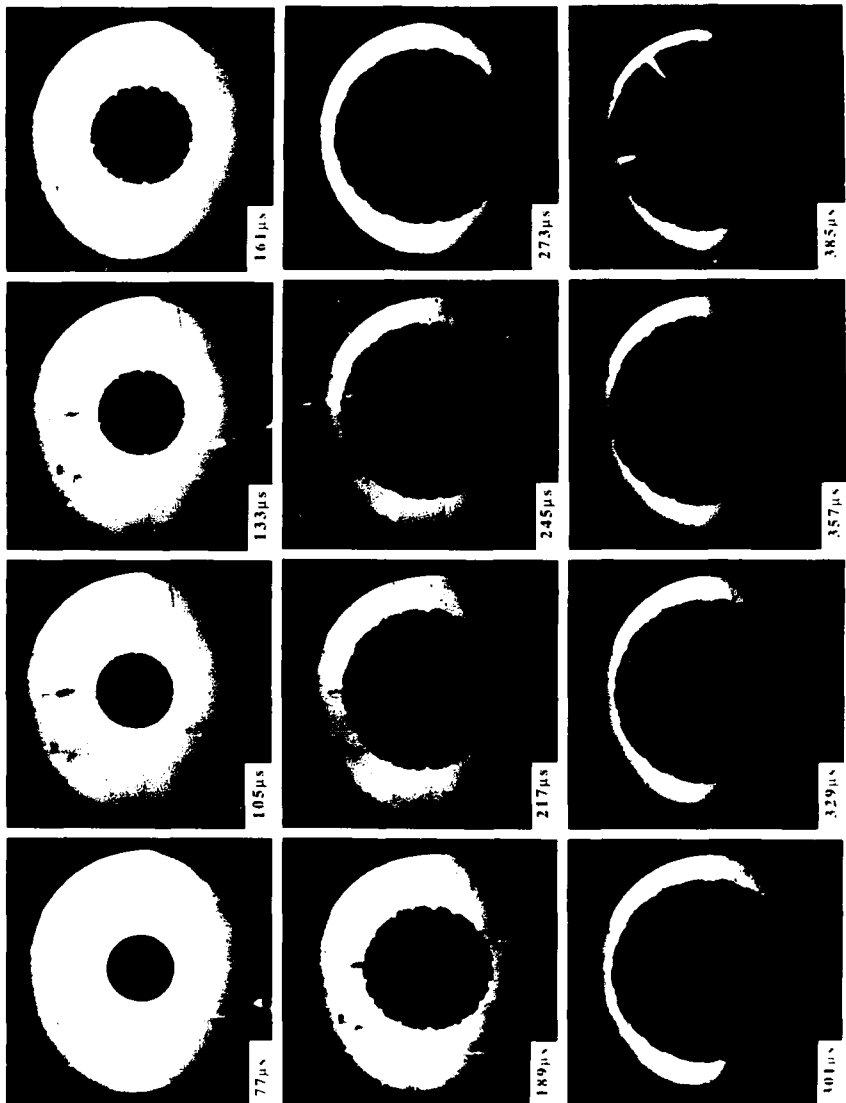


1



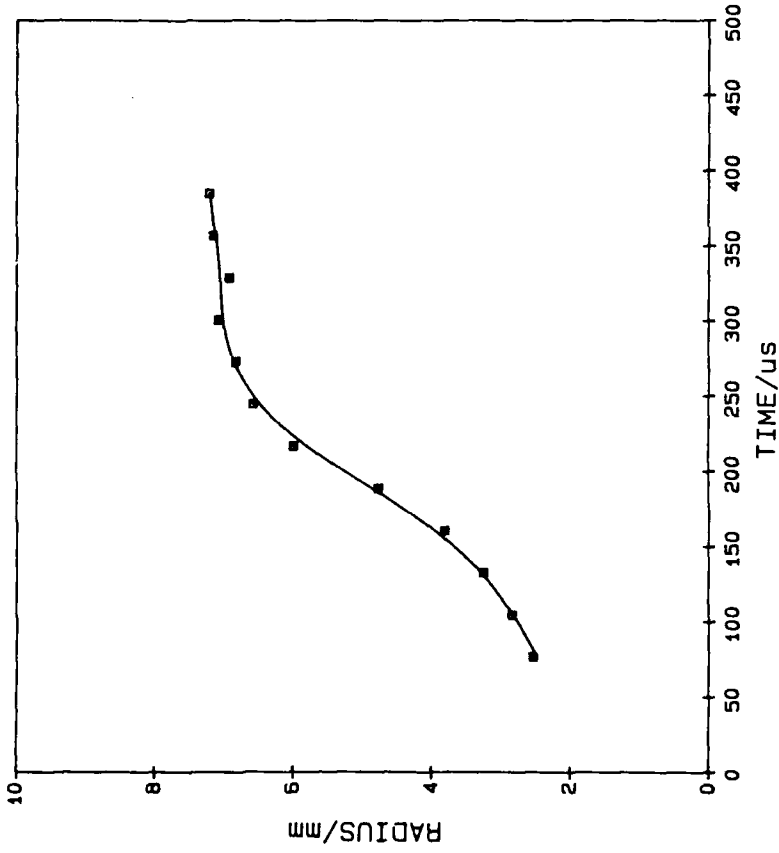
2

TATB/HTPB-IPDI
95/5 wt%



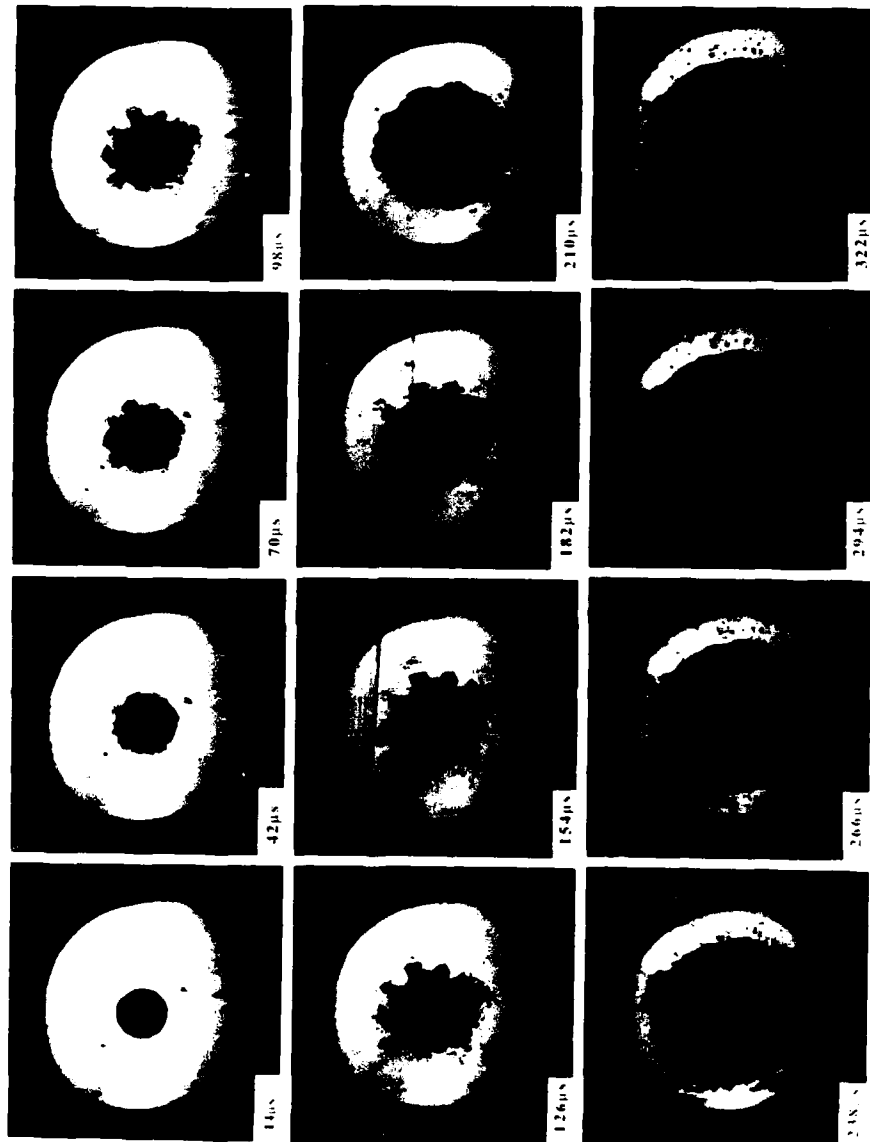
3

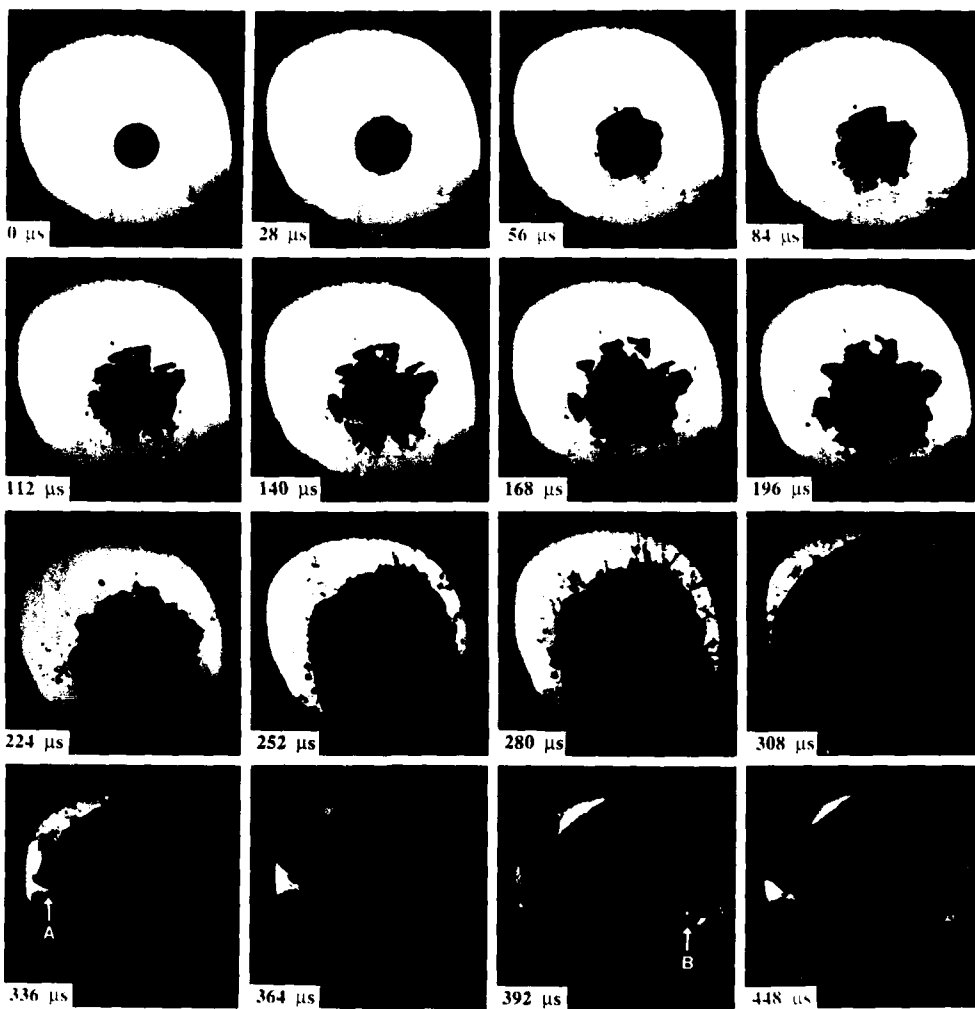
95/5 TATB/HTPB-TPDI



4

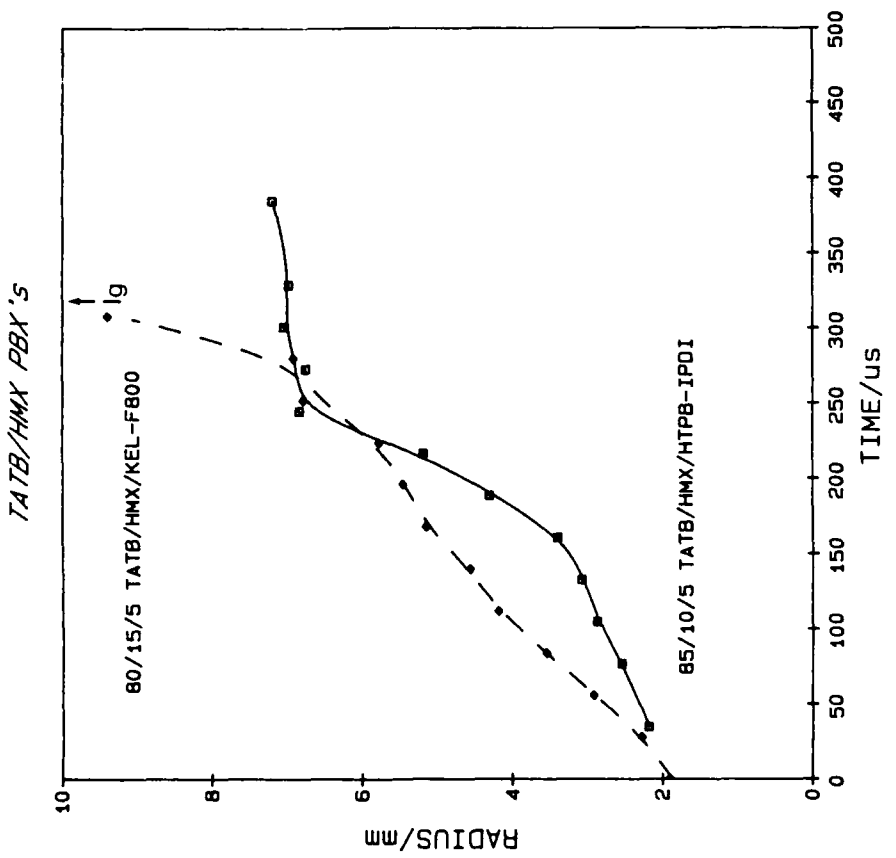
TATB/KEL-F 800
95/5 wt%



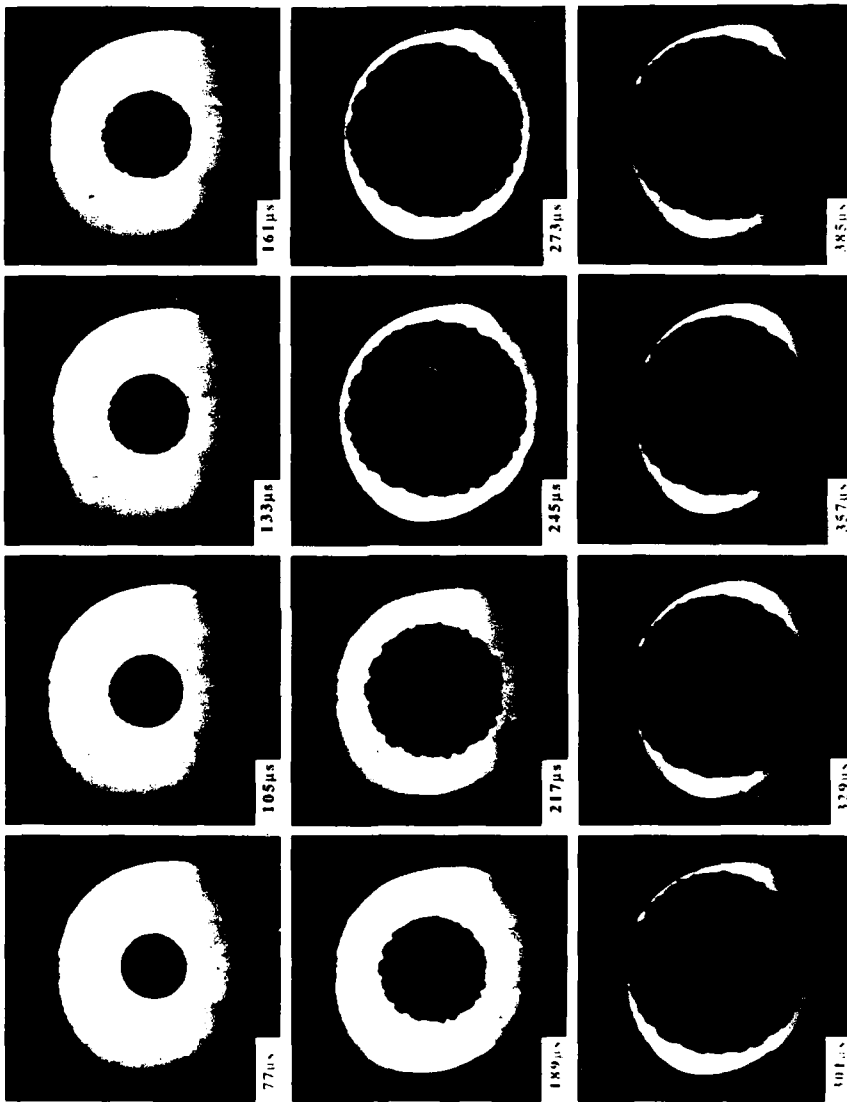


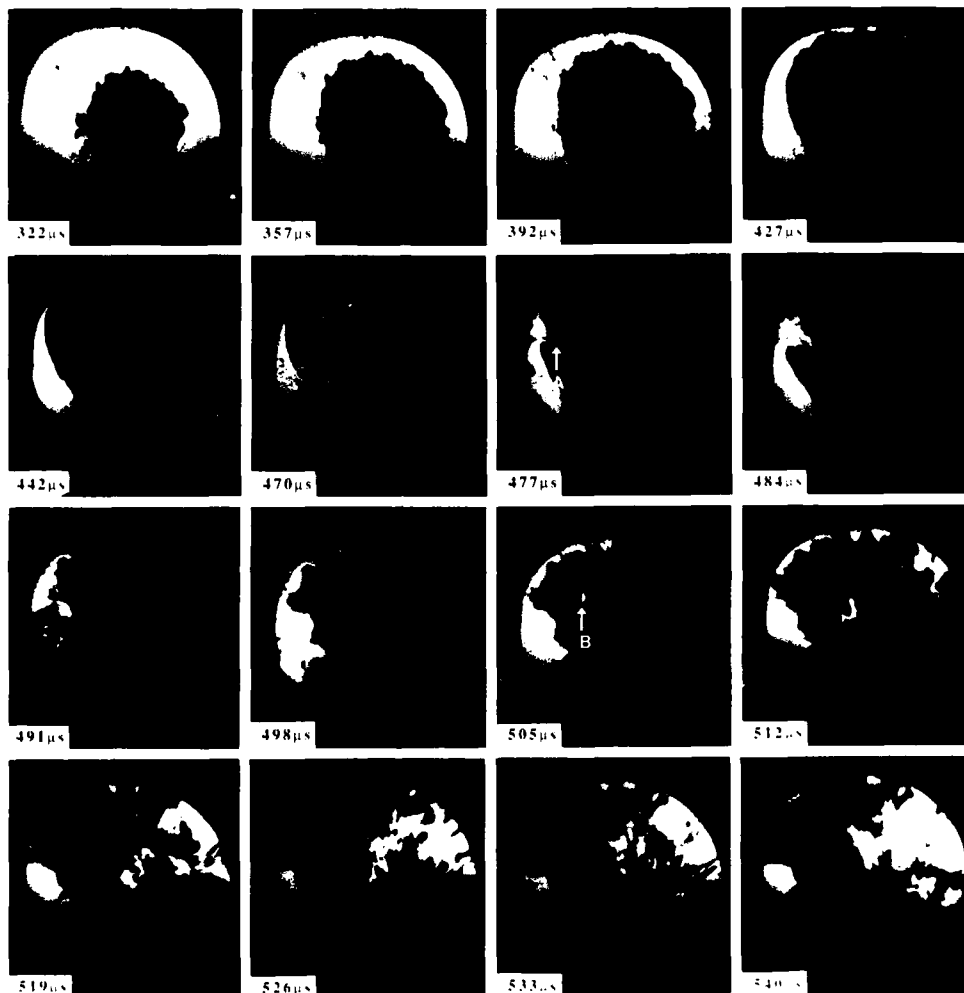
**TATB/HMX/KEL-F 800
80/15/5 wt%**

6



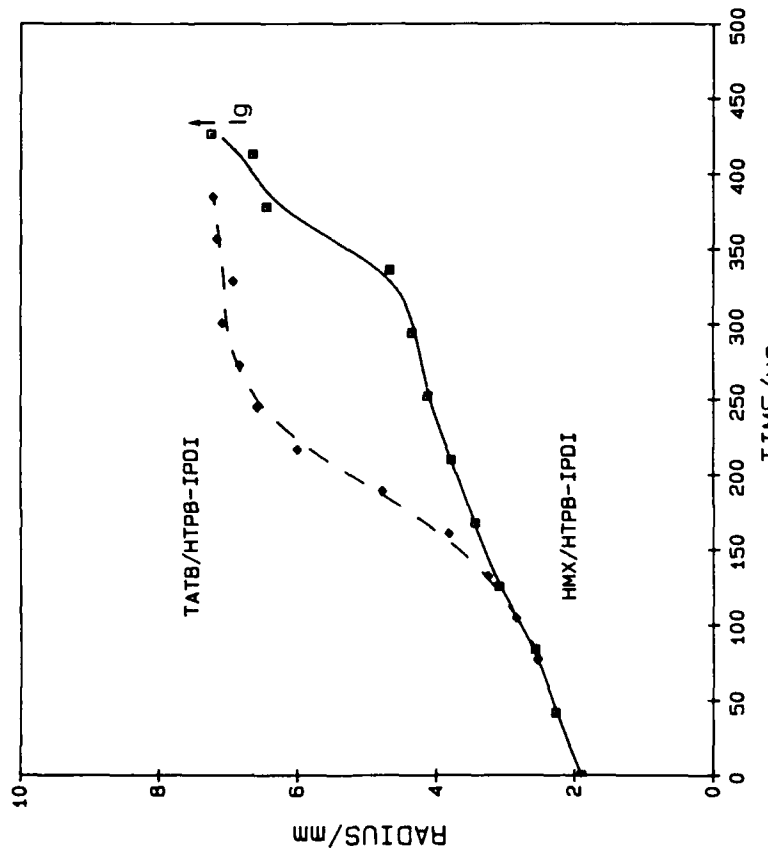
TATB/HMX/HTPB-IPDI
85/10/5 wt%



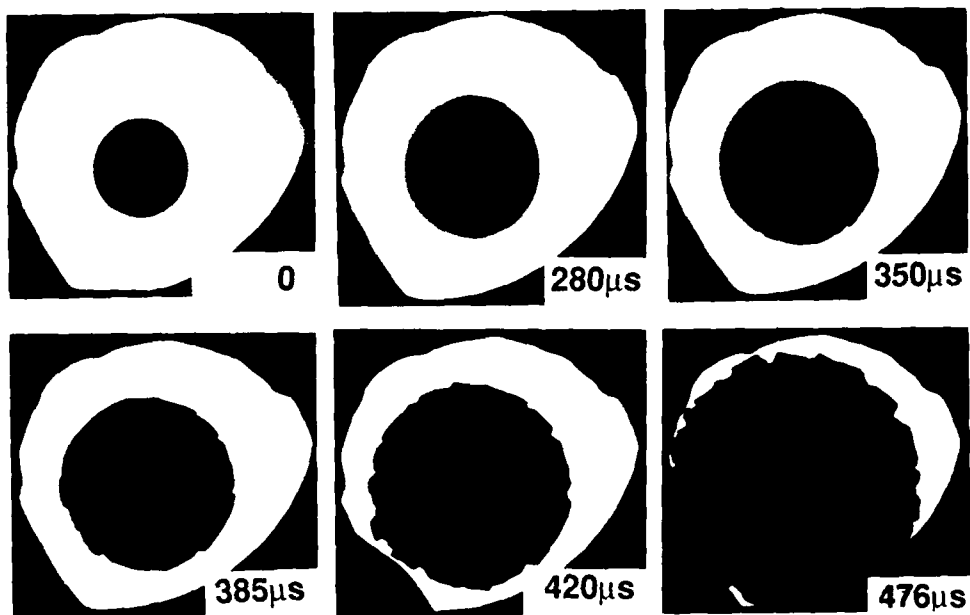


HMX/HTPB-IPDI
95/5 wt%

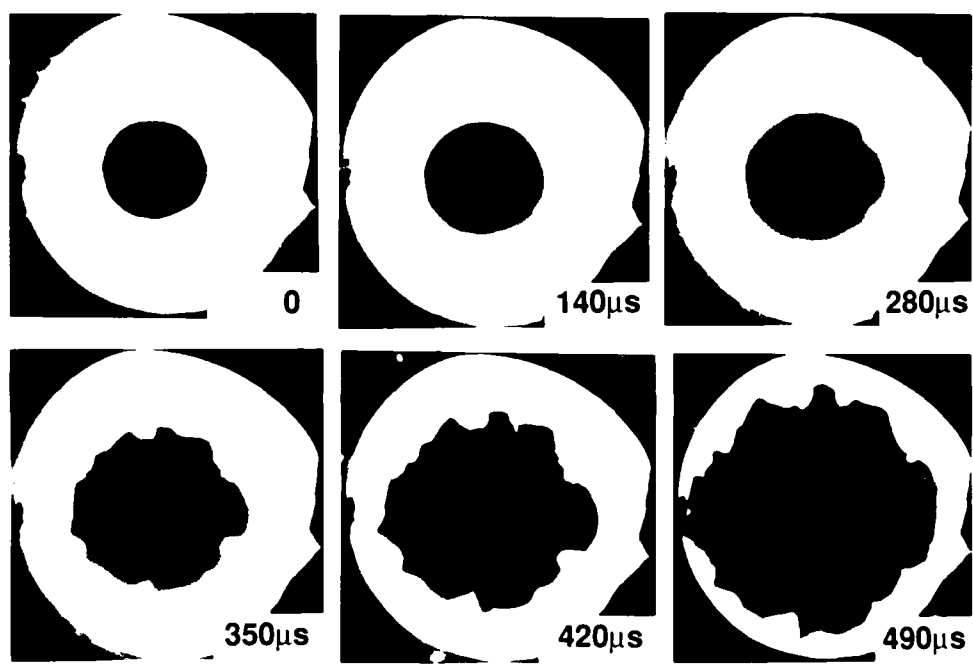
95/5 EXPLOSIVE/HTPB-IPDI



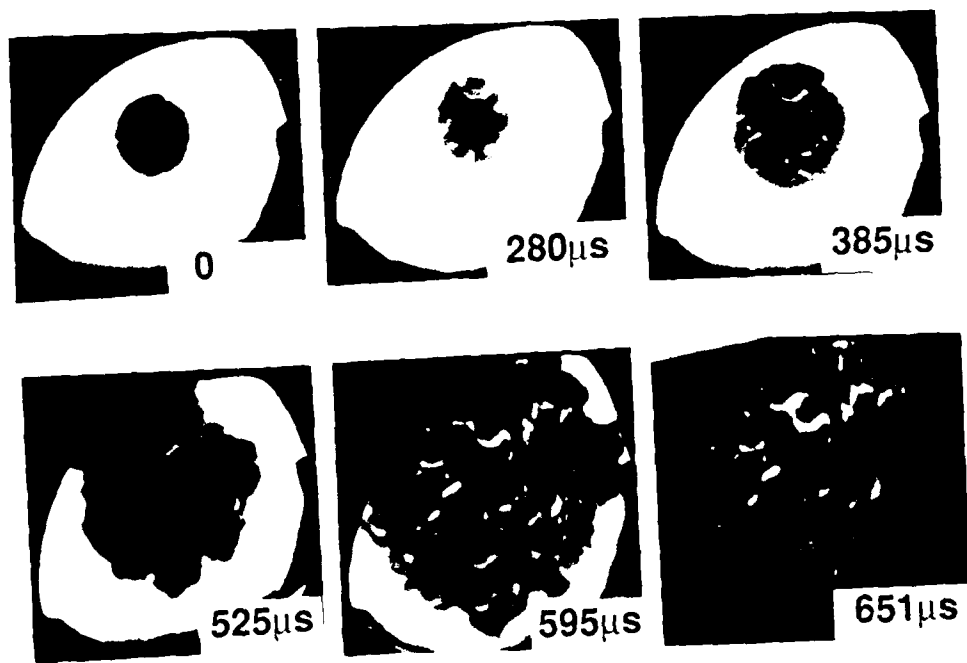
10



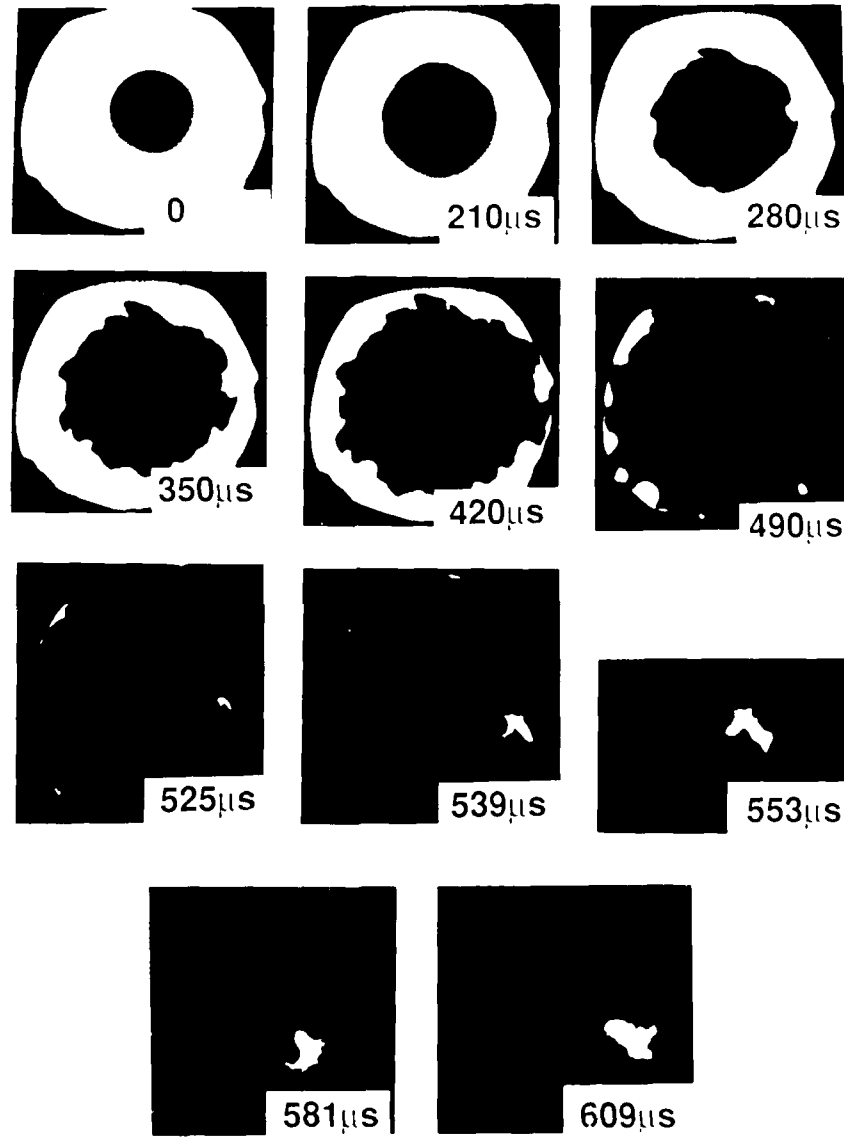
11



12



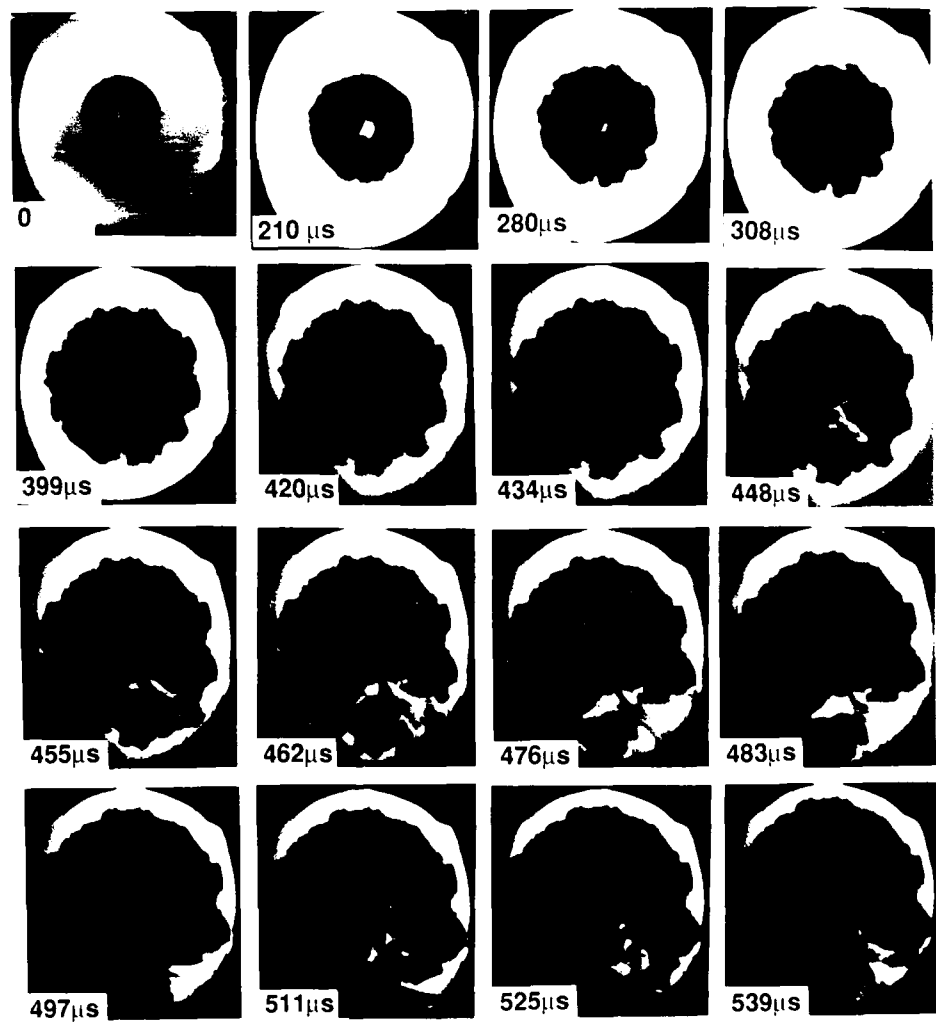
13



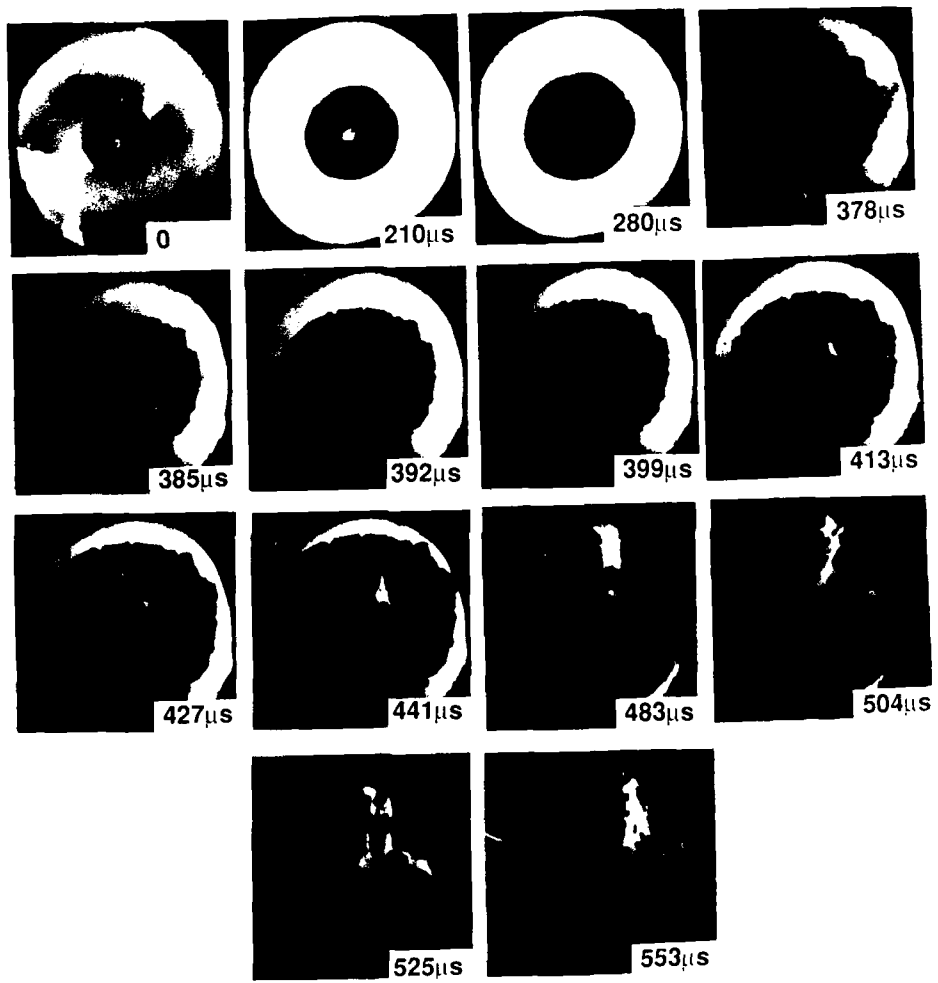
14

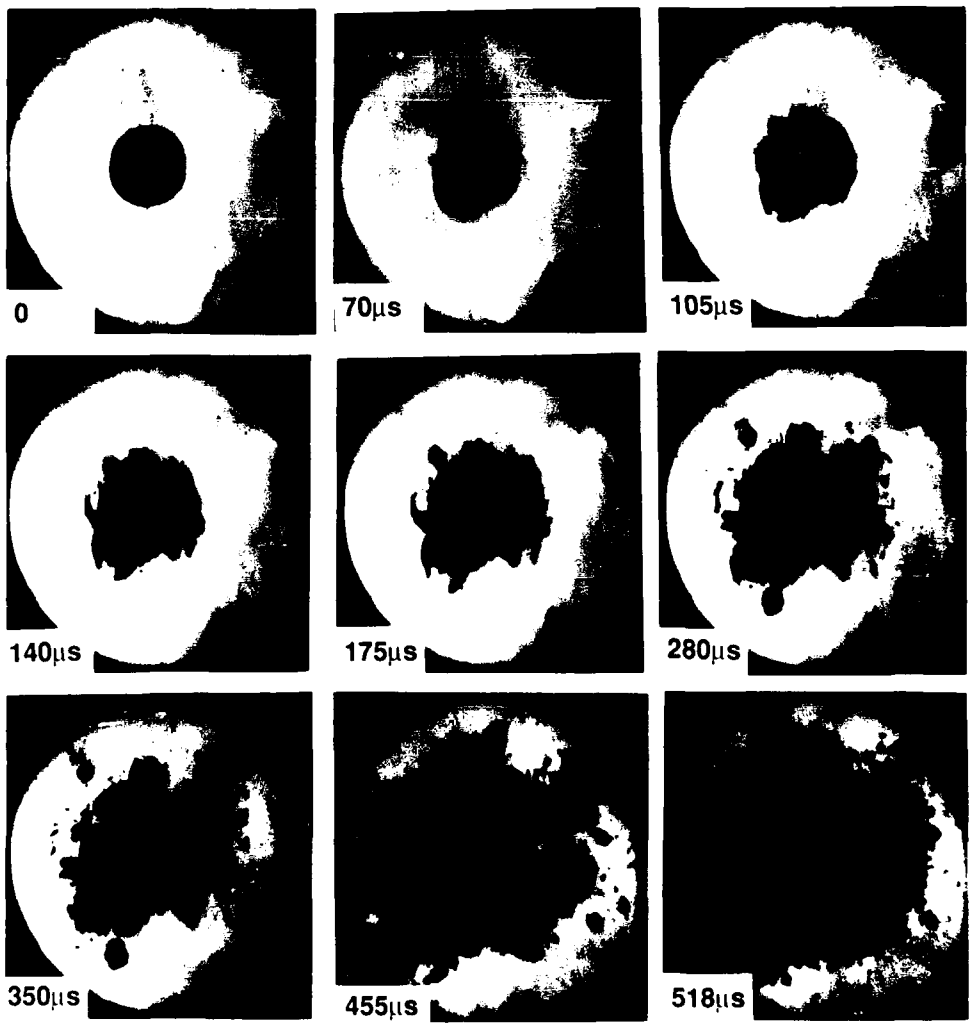


15

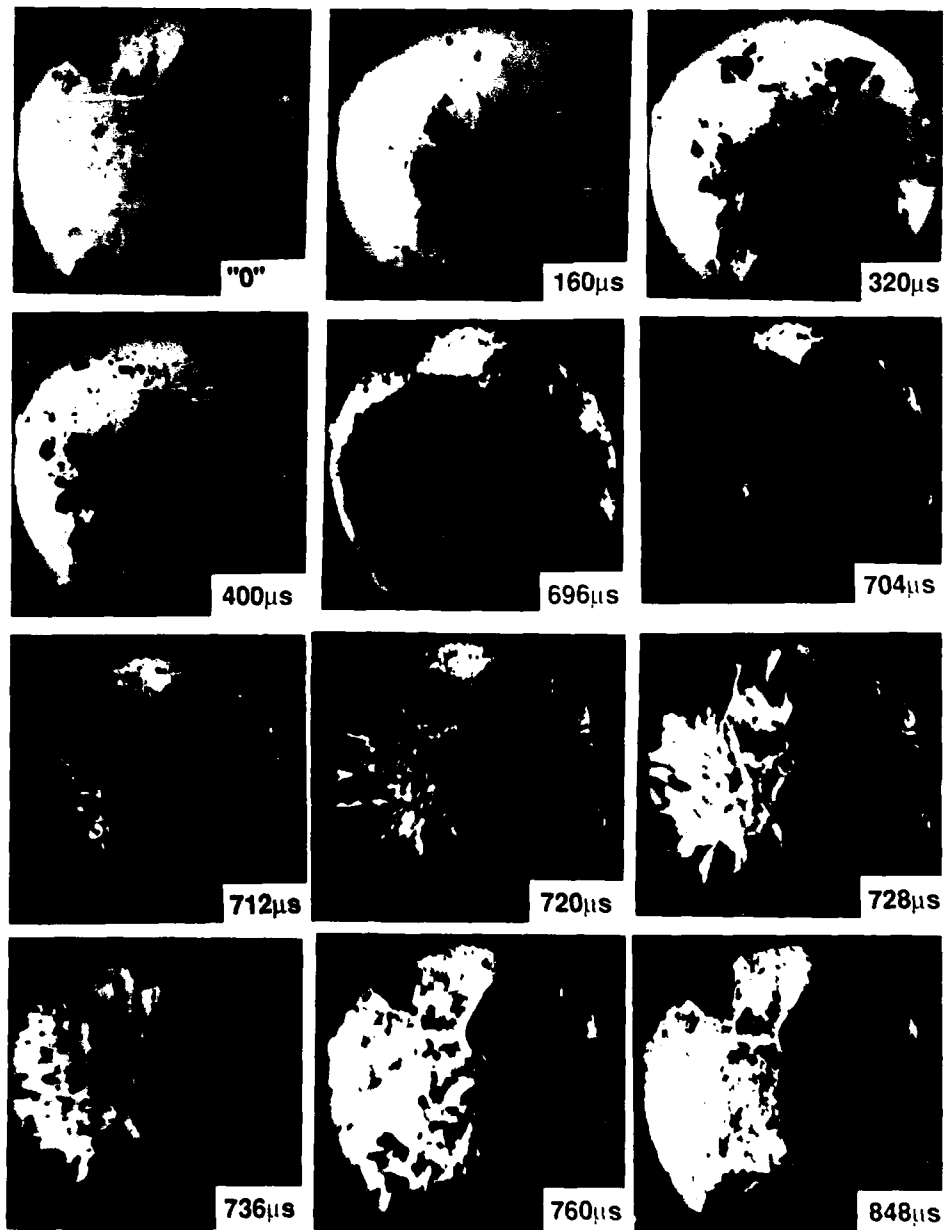


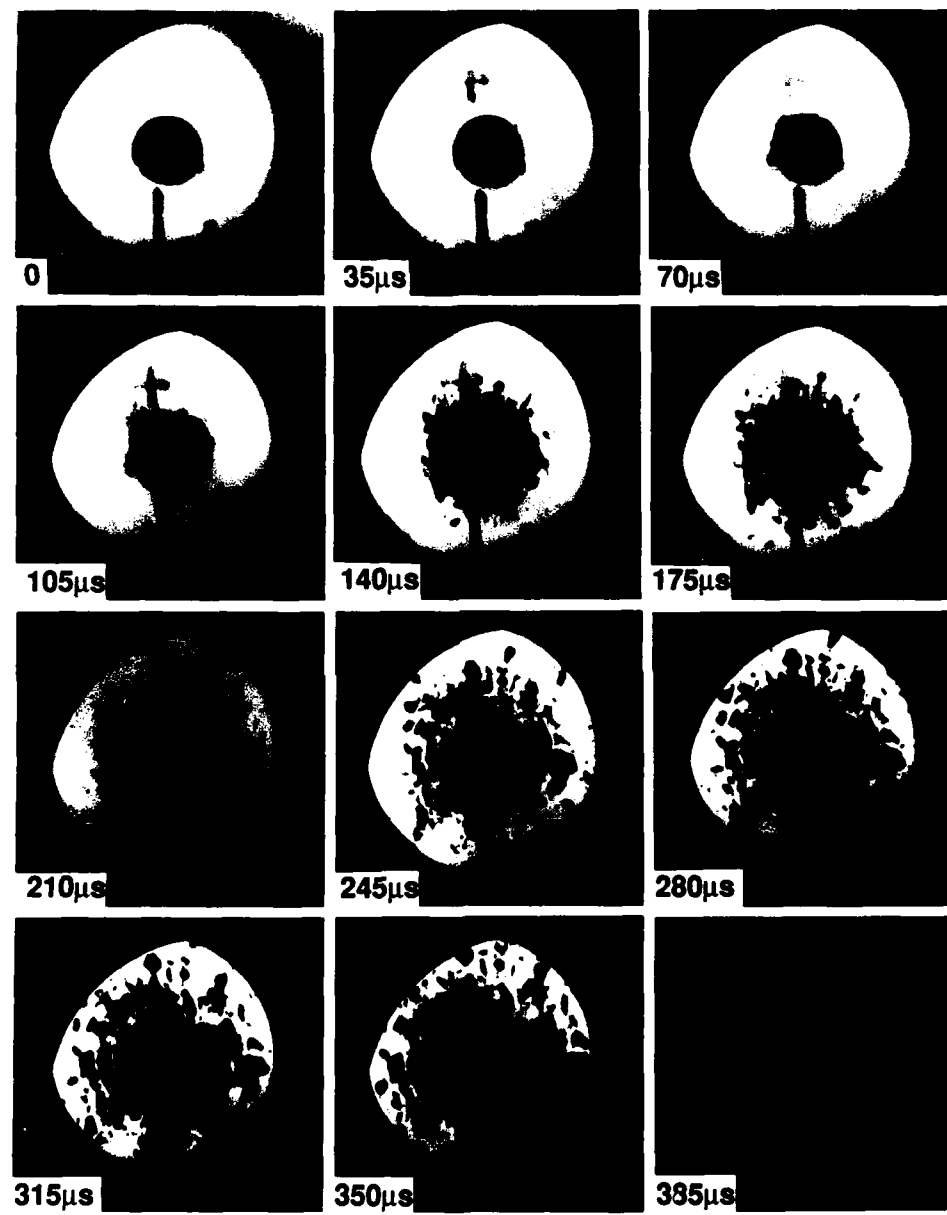
16



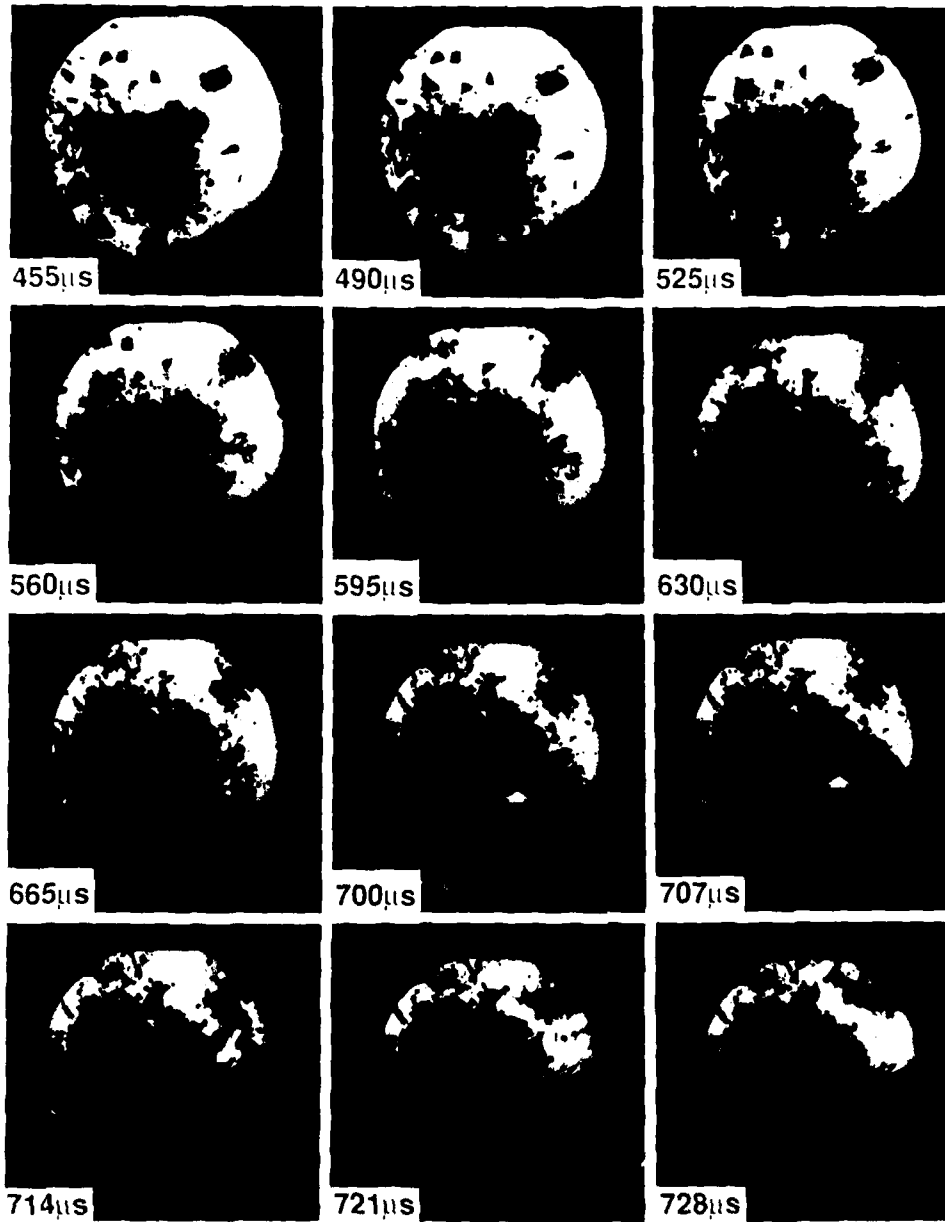


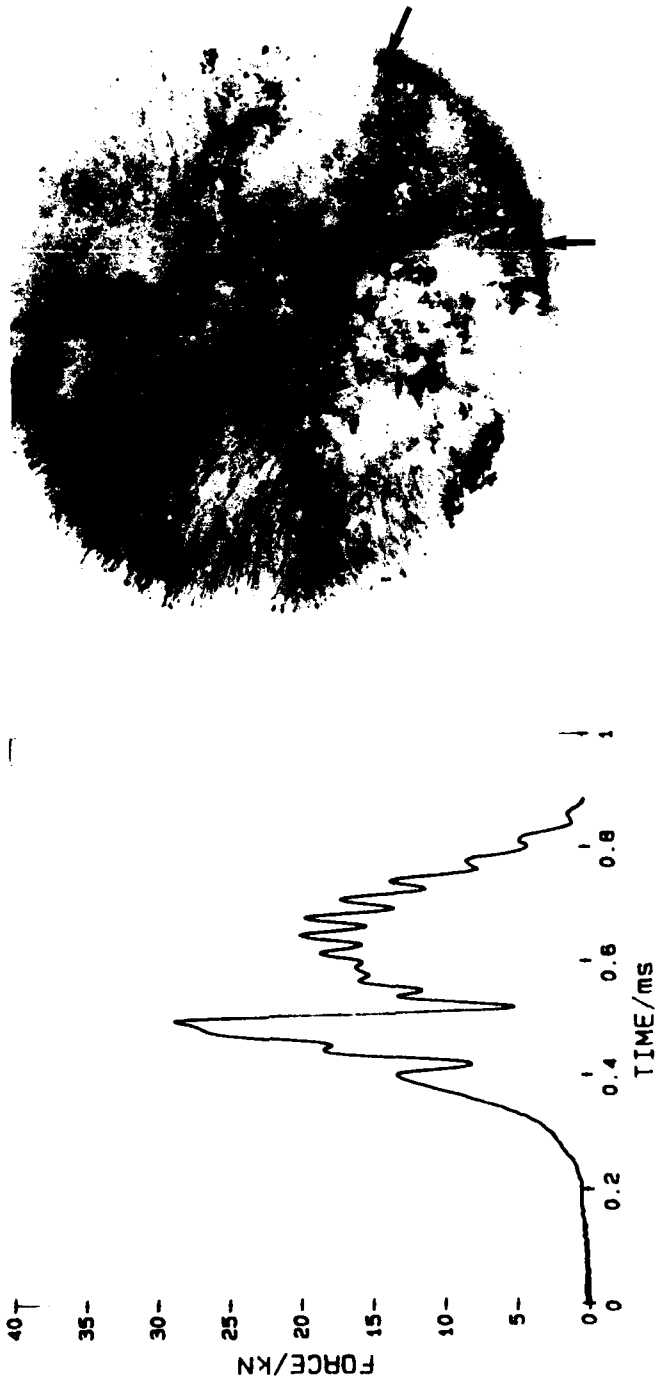
18



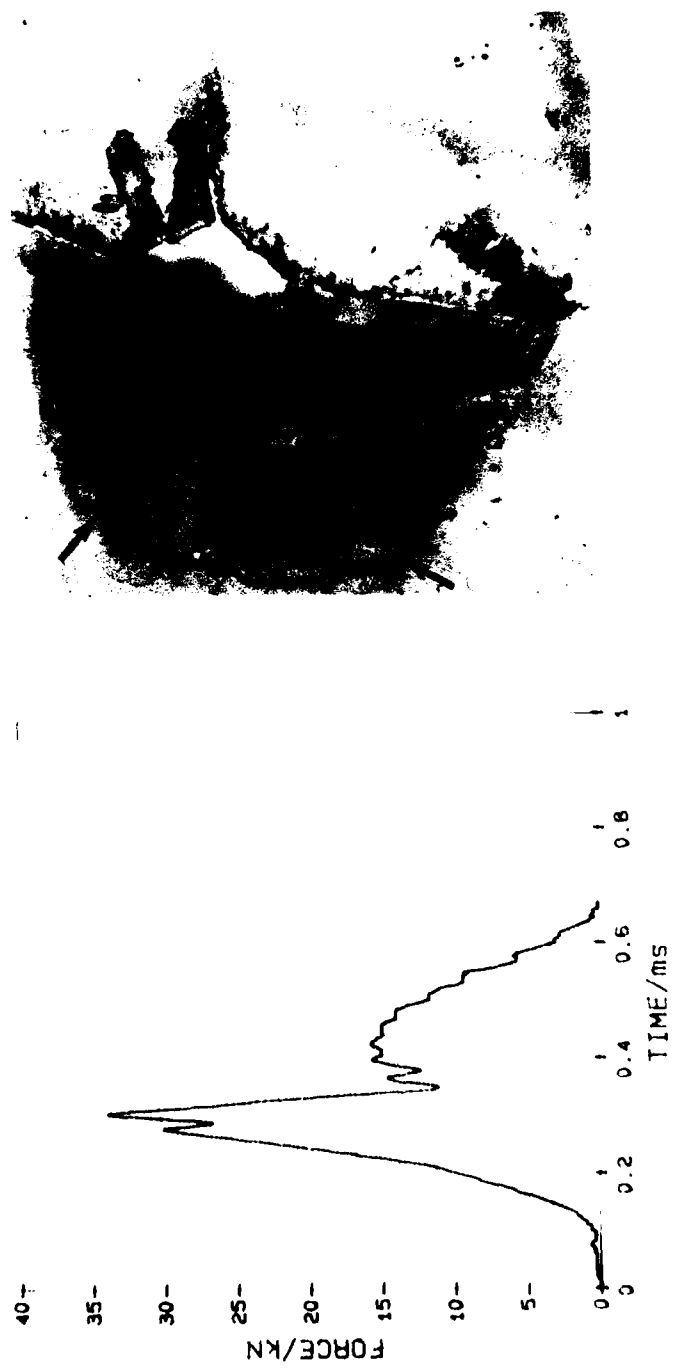


20

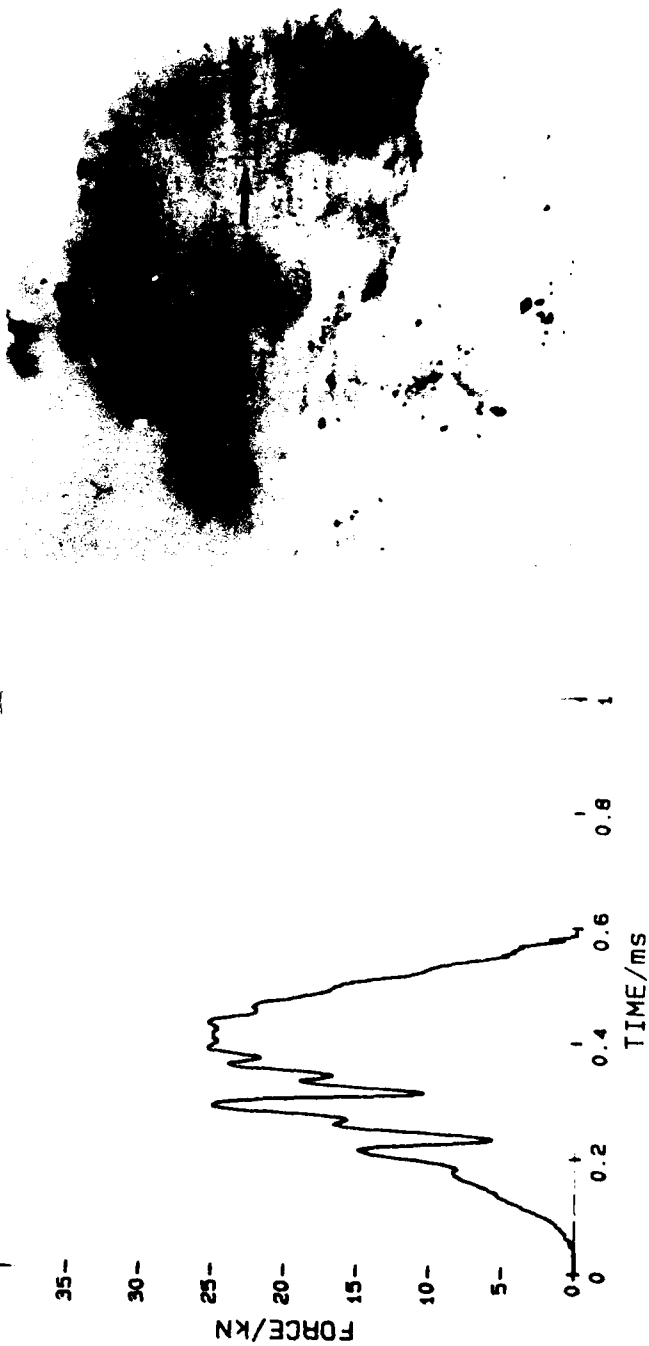




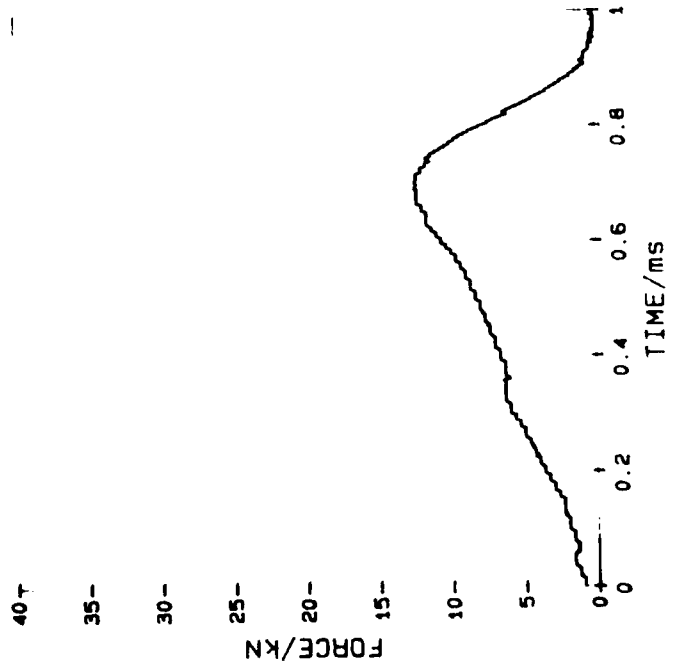
22



23



24



25

APPENDIX I

Field, Paper Number 86

9th Symposium (International) on Detonation
Portland, Oregon. September 1989.

DEFORMATION AND EXPLOSIVE PROPERTIES OF HMX POWDERS AND POLYMER BONDED EXPLOSIVES

J E Field, M A Parry*, S J P Palmer and J M Huntley
Cavendish Laboratory, University of Cambridge,
Madingley Road, Cambridge CB3 OHE, U.K.

Techniques have been developed for studying the behaviour of explosives when impacted, for recording their strength, failure and ignition properties. They include a drop-weight facility with transparent anvils, an instrumented drop-weight machine, a miniaturised Hopkinson bar system for high strain rate property measurement, laser speckle for studying the deformation and fracture of PBXs, an automated system for analysing speckle patterns and heat sensitive film for recording the positions and temperatures of "hot spots". Polishing and staining methods have been developed to observe the microstructure of PBXs and failure during quasi-static loading. Further evidence is given of shear banding in PETN and the effect of particle size on the behaviour of HMX during impact is described. The quasi-static strengths of PBX samples were measured using the Brazilian test with the strains recorded using laser speckle photography. Data is given for five PBX compositions.

INTRODUCTION

This paper describes the response of explosives to stress and impact. Samples in the form of powder layers, pressed pellets and polymer bonded explosives (PBXs) have been studied. It is important with all of these systems to understand the factors which affect their mechanical and thermal properties since these influence the mechanisms of "hot spot" formation and the explosives' "sensitivity" and "explosiveness".

EXPERIMENTAL

(a) High speed photography; transparent anvil drop-weight apparatus

Advances in the understanding of explosive phenomena have been greatly assisted by direct observation of events using high-speed photography. The ability to obtain both temporal and spatial resolution during impact has been particularly

valuable in establishing the sequence of events. The arrangement used in the present work (figure 1) was originally employed by Blackwood and Bowden¹ and has more recently been extensively used by Heavens, Field, Swallowe and others²⁻⁹. Typically, 25 mg samples of material, in the form of powders, pressed discs or PBX samples, are compressed between toughened glass anvils with an impact velocity of typically 4.5 m s^{-1} . The drop weight (mass: 5 kg) which carries the upper anvil is dropped from a height of up to 1.5 m and is guided by three rods to ensure a planar impact. Shortly before contact, the mirror within the weight comes into alignment to complete the optical path from the xenon flash light source, through to the high-speed camera. The AWRE C4 rotating mirror camera, is of the continuous access variety so that synchronization is not required. The full length of film (140 frames) is scanned in approximately 1 ms so that the duration of the flash also functions as a shutter.

Field et al^{6,7} determined that the initiation of explosive samples usually occurs after rapid radial flow (greater than ca. 100 m s^{-1}) unless sensitizing

* Now at Materials Research Laboratory, Ascor Vale, Victoria 3032, Australia.

grits are present. Valuable data which can be extracted from the photographs is therefore the radius as a function of time and, thereby, the velocity as a function of time. Rapid flow can occur as a result of mechanical failure of the sample but while this may be true in some cases, it is not a necessary precursor. If the material is sufficiently weak that it generates negligible retardation to the falling weight and deforms at constant volume, then high radial velocities are a natural outcome. In addition to the bulk plastic behaviour, other physical processes such as fracture, jetting, bulk plastic flow, localised adiabatic shear, melting and elastic recovery can be observed under favourable conditions. Explosive reaction is visible since it is self-luminous. Although photographs present a large amount of information, they cannot usually tell the whole story without corroborative evidence from other sources such as dynamic stress measurement.

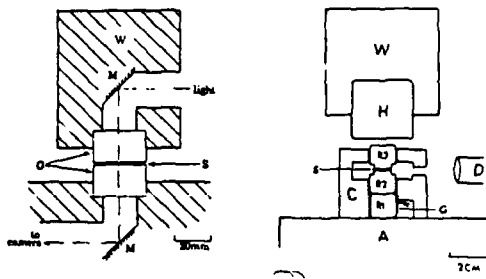


FIGURE 1. A CROSS-SECTION OF THE C4 DROP-WEIGHT SYSTEM. W IS THE WEIGHT, M A MIRROR AND G THE TOUGHENED GLASS ANVILS WITH S THE SPECIMEN.

FIGURE 2. INSTRUMENTED DROP WEIGHT. W IS THE WEIGHT, A THE ANVIL, R₁, R₂ AND R₃ THE STEEL ROLLERS, THE LOWEST BEING THE LOAD CELL HAVING STRAIN GAUGES G. LIGHT DETECTOR D.

(b) Instrumented drop-weight apparatus

A second drop-weight machine is available with instrumented steel anvils (figure 2). The system rests on a large blacksmith's anvil, which provides an almost ideal rigid support for a small load cell which measures the impact force. The cell is of in-house

design being made from a 12.7 mm × 12.7 mm steel bearing roller with two pairs of strain gauges fixed axially on opposite sides of the roller which has four flats machined on it. An impact cell is formed by two further rollers stacked on top of the load cell and samples are placed between this pair, the whole arrangement being impacted by a weight of 2.5 or 4.7 kg.

The dynamics of the system have been described in detail earlier^{2,3}, but a comparison with the behaviour of a direct impact Hopkinson bar (section c) is illuminating. Unlike the Hopkinson bar, the dynamics of the drop weight system do not require explicit account to be taken of stress wave propagation. The pressure bar in the smallest of our miniaturised Hopkinson apparatuses is made deliberately long at 150 mm, so that a stress wave can be observed without interference from reflections. The drop-weight load cell is much shorter, being 25 mm including the protective roller on top of it, but the timescale over which it operates is 400 µs compared with 16 µs for the pressure bar. Consequently there are many stress wave reflections in the load cell and its behaviour is therefore quasi-static.

A further facility which is used with 25 mg samples when initiation is expected is the detection of electrical conductivity between the anvils. This can detect ionised gas and pinpoint the initiation of explosion. Alternatively, ignition is detected by monitoring light output with a photo-cell.

(c) Miniaturised Hopkinson bar

In a conventional Hopkinson bar system (see, for example,¹⁰), the specimen is placed between two long, cylindrical rods. A stress pulse is then sent down the input bar and gauges record incident, reflected and transmitted waves. From these records, it is possible to obtain stress/strain behaviour of the specimen at strain rates of ca. 10^3 s⁻¹. A few years ago, Gorham¹¹ developed a direct impact (no input bar) miniaturised system. Initially, a high-speed camera was used to measure strains, but this is not essential and stress strain curves can be obtained from the gauge records on the output bar following an analysis given by Pope and Field¹². The advantages of the new apparatus are

that strain rates up to ca. 10^5 s^{-1} can be achieved and high strength specimens investigated. Results on a range of PBXs were presented at the last Detonation Symposium⁹.

(d) Brazilian test and laser speckle for tensile strengths and strains to failure

The Brazilian test geometry (figure 3) and laser speckle photography have been used to study the tensile strengths and rupture strains of a variety of PBX compositions at strain rates of ca. 10^{-4} s^{-1} .

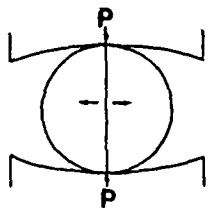


FIGURE 3. LOADING ARRANGEMENT USED IN BRAZILIAN TEST.

The compression induces tensile stresses normal to the loading axis which are sensibly constant over a region about the centre of a specimen. The tensile strength of the material is then calculated from

$$\sigma_t = 2P / \pi Dt, \quad (1)$$

in which P is the failure load, and D and t the diameter and thickness of the specimen respectively. The validity of equation 1 is based on the assumptions that failure occurs at the point of maximum tensile stress (i.e. at the centre), and that the compressive stress has no influence on the failure. In practice, the use of plane anvils can produce very high contact stresses at the loading points, and lead to the collapse of the contact edge. Awaji and Sato¹³ have shown that by using curved anvils collapse of the edge can be avoided, and shear stresses under the points of loading may be substantially reduced. If the ratio of the contact half-width, b , to the disc radius, R , is larger than approximately 0.27, the maximum principal stresses near the contact area are compressive. Then the tensile stress at the centre is given by

$$\sigma_t^* = \{1 - (b/R)^2\}\sigma_t. \quad (2)$$

Other workers¹⁴⁻¹⁶ using the Brazilian test geometry have employed displacement transducers to measure the average tensile strain across a diameter. However, the use of a relatively simple optical technique called "speckle photography" allows in-plane displacements to be measured to an accuracy of ca. $0.1 \mu\text{m}$ at different positions on the sample surface, and thereby determine the strain field at any point^{17,18}. There is the added advantage that it is a remote sensing technique which does not involve attaching gauges to the sample. For displacement and strain measurements, a double exposure is photographically recorded before and after deformation. Displacement information can be extracted by allowing an unexpanded laser beam to pass through the negative. If, at the point illuminated the "speckles" have been displaced between exposures, the displacement vector is manifested by a Young's fringe pattern observed at the far-field Fraunhofer diffraction plane. The displacement vector is perpendicular to the fringe orientation with magnitude inversely proportional to the fringe spacing. Complete analysis involves many measurements, and becomes tedious when performed manually. For this reason, a fully automatic electro-optical system for measuring the displacement field from a double exposure speckle photograph has been constructed¹⁹. With the present system the computation time per fringe pattern is under 10 s, giving a total analysis time per photograph of typically 30 - 40 minutes.

(e) Heat sensitive film technique

The technique used in this work was first suggested by Coffey and Jacobs²⁰. It is based on the use of an acetate sheet coated with a sensitive layer which darkens on exposure to heat. For very short duration heat pulses ($< 10^{-4} \text{ s}$) the film colour is yellowish-brown rather than black and the degree of darkening increases as the contact time is increased, until the film is fully blackened. The colouration is believed to be due to the reaction in the sensitive layer being unable to go to completion in the time available. Film darkening is a function of both temperature and time so, to use the film to estimate the temperature achieved during deformation, one must know the time over which the deformation occurred and then refer to a set of calibration curves (darkening as a function of time and temperature)

for the film. Details of how the film has been calibrated can be found in reference 21.

To use the calibration to obtain a temperature in an impact experiment, it was necessary to measure the time during which the darkening took place. These measurements were made by using the transparent anvil arrangement described above. Experiments were carried out by placing the film on the glass anvils with the sensitive side in contact with the sample. Results giving the temperatures achieved during the deformation, shear banding and fracture of a range of polymers can be found in reference 21.

(f) Microstructure and fracture paths in PBX's

Polishing and staining techniques have recently been developed to study the relationship between the microstructure of polymer bonded explosives and their fracture routes when broken in the Brazilian test under quasi-static conditions. A post-failure examination of the fracture route through the microstructure, provides a valuable insight into the fracture mechanisms. It is not, however, usually possible to determine where failures initiated, or the order in which events occur during crack propagation. A technique has therefore been developed using a computer operated camera (Olympus OM2 with motor drive), attached to a microscope stage to record photographic sequences of the microstructure at the centre of a sample during a Brazilian test.

RESULTS

(a) Drop-weight impact on PETN; further evidence for ignition by adiabatic shear

Drop-weight impact, using the transparent anvil and instrumented apparatus (figures 1 and 2) was first used by Heavens and Field in the early 1970's^{2,3}. They showed that thin layers exhibited fracture, compaction, sintering, plastic flow at high velocities, jetting, melting, and ignition in the glass anvil apparatus. Banded structures which became visible in some sequences, with both PETN and RDX, were interpreted, we now think wrongly, as ripples caused by jetting. The evidence on this point

was re-interpreted by Field et al.⁶ and evidence was presented to show that the features were shear bands; a mechanism for hot-spot production and ignition which has been suggested by Winter and Field for other explosives in 1975²². At the last Detonation Symposium, photographic evidence was presented of adiabatic banding in PBXs and PETN⁹.



FIGURE 4. HEAT SENSITIVE FILM RECORD OF AN IMPACT ON PETN. ORIGINAL IN COLOUR. CLEAR EVIDENCE OF SHEAR BANDING AND ASSOCIATED IGNITION.

Figure 4 shows the result of an experiment when the heat sensitive film was used. The original is in colour but the black and white reproduction shows the key features. Where there has been fast reaction the products have removed much of the heat-sensitive layer, but at the top of the picture where the film remains it is a deep orange-brown. In the lower part of the film there is a great arc of banding and where the heat sensitive layer remains attached it varies from light brown to almost black, all indicative of high temperatures. The ignition also clearly starts from the region where the bands are located. Figure 5 shows an impact from a sub-critical height onto a PETN layer. It shows the

TABLE 1

Type	Comments	Particle size range/ μm	Median particle size/ μm
A	Granular powder produced by recrystallisation from cyclohexanol.	100 to 1000	480
B	Fine powder produced by colloid milling of type A. Bimodal distribution.	2 to 130	28.5
TC/14	Micronised by fluid energy milling of type A.	2 to 180	20
TC/13	"	2 to 36	10
TC/12	"	2 to 29	6.4

families of shear bands particularly well in part of the unexploded layer.



FIGURE 5. SHEAR BANDING IN PETN AFTER IMPACT, WHERE IGNITION FAILED TO OCCUR.

(b) Drop-weight impact on HMX of different particle sizes

The HMX was provided by AWRE and Table 1 gives details.

(i) Experiments with heat-sensitive film

The HMX samples were impacted using 12 mm discs of heat-sensitive film (HSF) on the lower roller of the steel anvil apparatus, with the emulsion side of the film against the explosive. A range of drop-

heights were used and the H_{50} 's determined for the HMX samples in the presence of HSF. These H_{50} 's were in fact higher than the H_{50} 's with bare anvils. The de-sensitising effect of the HSF is thought to be due to the increased friction which decreases the velocity and extent of rapid flow.

Figure 6 shows two HSF discs viewed in silhouette, and also the extent of flow of the HMX (dashed line). The sample originally occupied an area similar to that of the discoloured region. The extent of radial flow of the sample with HSF was less than when bare metal anvils were used. Presumably this was due to increased friction between the explosive and the HSF. The band-like character of the heat output during the impact experiment is evident in figure 6a and can still be detected in figure 6b, even though partial ignition and propagation of the explosive had occurred.



FIGURE 6. TWO RECOVERED DISCS OF HEAT-SENSITIVE FILM (HSF). THE EXPLOSIVE HAS BEEN REMOVED:

- (a) THE AREA THAT THE HMX OCCUPIED AFTER IMPACT IS INDICATED. THE DISCOLOURATION OF THE HSF APPEARS AS A PATTERN OF BOTH RADIAL AND PARALLEL LINES. THE SAMPLE ORIGINALLY COVERED AN AREA SIMILAR TO THE DISCOLOURED AREA.
- (b) PARTIAL REACTION HAS OCCURRED AND PART OF THE HSF DISC HAS BEEN CONSUMED, BUT THE BAND-LIKE PATTERN IS STILL APPARENT NEAR THE CENTRE OF THE DISC.

Figure 7 is a HSF disc viewed by reflected light. Note, the original photograph was in colour! The patterns on the recovered HSF disc consists of families of approximately parallel lines, some of which bifurcate, and which are characteristic of shear bands. The figure shows that black (very hot)



FIGURE 7. HSF RECOVERED AFTER IMPACT OF HMX SHOWING BRANCHING OF THE SHEAR BANDS AND DISCOLOURATION WHERE BRANCHING OCCURS. ORIGINAL IN COLOUR.

areas also occur at the junction of some lines (labelled C). Figure 8 shows failure patterns in HMX which has remained on the steel rollers after impacts from sub-critical heights. Figure 8a shows the HMX after a test with HSF and reveals the close resemblance between lines on the HSF and failure in the explosive. This type of failure pattern was also observed during impact of HMX with bare metal rollers. Figure 8b is a clear example of shear bands in an impacted layer of HMX. The conclusion is that HMX fails by shear banding in these experiments and that these shear bands are the hot-spot sites which cause ignition.



FIGURE 8. PHOTOGRAPHS OF EXPLOSIVE REMAINING ON HARDENED STEEL ROLLERS AFTER IMPACT. (a) IS FROM A TEST WITH HSF. NOTICE THE LINES IN THE DISC RESEMBLE THE FAILURE PATTERN IN THE EXPLOSIVE. (b) WAS OBTAINED DURING IMPACTS WITH BARE METAL ROLLERS AND SHOWS A BAND-LIKE FAILURE PATTERN.

(ii) High Speed Photography

Heaens and Field^{2,3} showed that HMX compacted, jetted, flowed plastically, and ignited, but unlike PETN and RDX did not sinter and melt. Although the propagation rate in HMX was high, combustion was invariably incomplete in the drop-weight experiments. This type of behaviour was found in the present work, with the residue varying considerably. All the experiments were from a 1 m drop-height onto 25 mg powdered layers.

Figure 9 is for type A HMX and is typical of all impacts on this coarse material (Table 1) where ignition took place. The small, slightly, darker region which is just visible near the centre in most of the frames is due to overwriting as the camera mirror comes into position again. All the stages listed above are clearly shown. Ignition occurred on rebound after a short plateau region and is a perfect example of what we classify as a "widespread" ignition from a multitude of sites. The finer grain samples all exhibited "local" ignitions. Figure 10 is an example for TC/12 HMX (Table 1) where it took place during the initial rapid flow stage. The initial propagation in frame 42 is very similar to the patterns found on the heat-sensitive film (figures 6-8). Figure 11 is for type B HMX (Table 1) and contains some interesting extra features. Local ignition occurs during the rapid flow stage at a group of small sites (three white dots) in frame 48. But

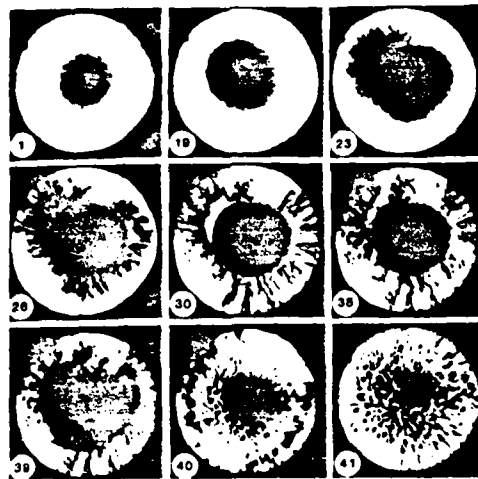


FIGURE 9. IMPACT ON TYPE A HMX,
WIDESPREAD IGNITION WITH RAPID FLOW
(MAXIMUM VELOCITY 240 m s^{-1}), FRAMING
INTERVAL $6.5 \mu\text{s}$, FIELD OF VIEW 20 mm.

these fade and extinguish (frames 48-54). Local ignition at a new site eventually takes over. Enlarged views of frames 48, 49 and 54 are shown in figure 12. Note that the structure of the main hot spot is reminiscent of the patterns on the HSF. Finally, the banded structure which influences the propagation so strongly in frame 57 also suggests the presence of shear bands in the deforming HMX.

(iii) Explosiveness, propagation; dependence on particle size

Damage to the surface of the glass anvils after impact depended on the particle size of HMX used and only occurred when there was an explosive reaction. The area of damage for coarse HMX was larger than for fine HMX, although there was overlap. The high-speed photographic records also showed that the propagation of reaction was higher in coarser material. This fits in with LABSET data (the AWE test for "explosiveness") on the PBX's that we have tested. The LABSET figure is usually higher if it contains coarser material compared to micronised crystals.

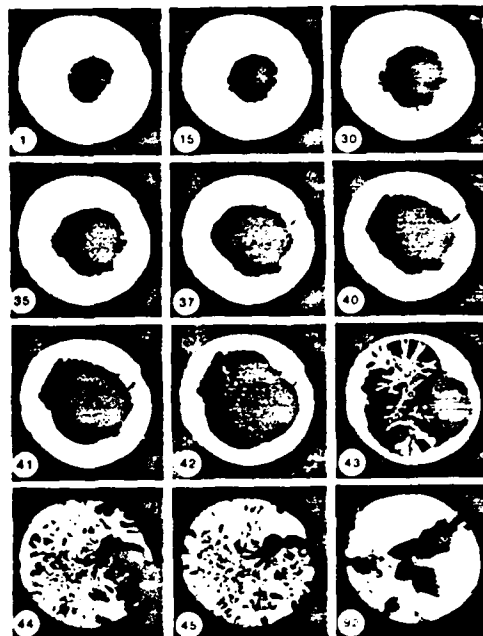


FIGURE 10. IMPACT ON FINE GRAIN HMX
(TC/12). LOCAL IGNITION DURING RAPID
FLOW (MAXIMUM VELOCITY 240 m s^{-1}),
FRAMING INTERVAL $7 \mu\text{s}$, FIELD OF VIEW
20mm.

Cross-sections of impacted layers which did not ignite show a denser compacted material with fine powders and an open structure with coarser material. The burning front clearly propagates more readily through a compacted layer of coarser material. See, for example, figure 9 with its "widespread" ignition and propagation. For finer material (see for example figures 10 and 11) there is propagation from "local" sites along a few channels. A second factor which assists more rapid propagation through a compacted layer with larger particles is the higher heat conduction. The more frequent grain boundaries with compacted fine-grain crystals lower the bulk conductivity. We have measured the thermal conductivity of pressed powdered layers; the value for coarse HMX was twice that of micronised HMX.

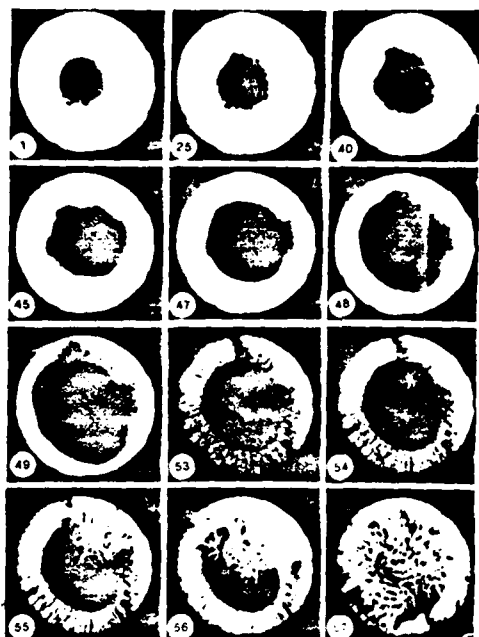


FIGURE 11. TYPE B HMX. MAXIMUM VELOCITY OF 185 m s^{-1} . THE FIRST LOCAL IGNITION SEEN IN FRAME 48 FADE. A LOCAL IGNITION WHICH PROPAGATES STARTS IN FRAME 54. NOTE THE BANDED APPEARANCE IN FRAME 27. FRAMING INTERVAL $7\mu\text{s}$, FIELD OF VIEW 20 mm.

(c) QUASI-STATIC STRENGTHS AND STRAINS TO FAILURE OF SOME PBX'S

Introduction

Samples from five different PBX compositions in the form of discs 6.35 mm in diameter by 2.0 mm thick (Table 2) were used to measure the quasi-static strengths and strains to failure, at a strain rate of 10^{-4} s^{-1} .

Typically ten samples were tested for each material. There is only space to illustrate one set of data (figure 13) and to discuss the results briefly.

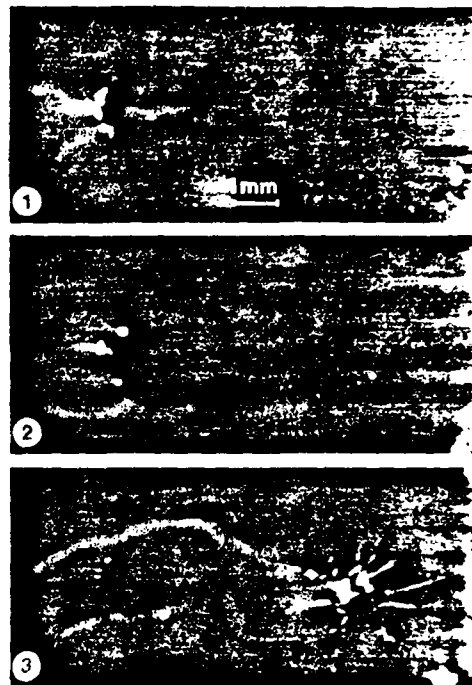


FIGURE 12. ENLARGED VIEW OF FRAMES 48, 49 AND 54 OF FIGURE 40. FRAME 1 IS $337\mu\text{s}$ AFTER FIRST CONTACT.

TABLE 2. DETAILS OF PBX COMPOSITIONS

Composition	Constituent	Weight per cent	Tensile Strength MPa	Fracture Strain /millistrain
PBX 9501	HMX ESTANE BDNPA BDNPF	95.0 2.50 1.25 1.25	0.78 ± 0.1	3.92
PBX 9502	TATB KEL F	95.0 5.0	3.23 ± 0.1	2.91
PBX 0298	HMX Kraton Oil	97.50 1.125 1.375	1.06 ± 0.1	11.20
PBX 0407	TATB PETN KEL F Dyc	69.8 25.0 5.0 0.20	4.12 ± 0.3	3.03
PBX 0344	TATB HMX KEL F	71.25 23.75 5.0	4.17 ± 0.4	1.70

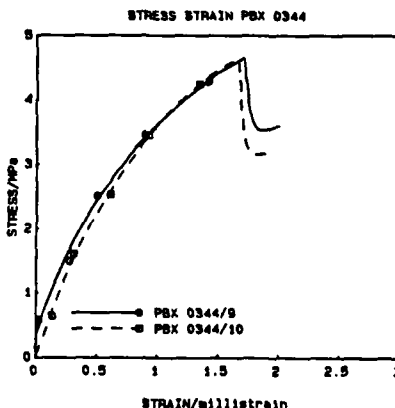


FIGURE 13. RESULTS FOR PBX 0344.
(a) STRESS VERSUS TIME PLOT.

Of the five materials tested compositions PBX 0298 and 9501 showed the lowest tensile strengths, failing at a stress of 1 MPa or less. Both materials behaved in a rather ductile manner. However the strains to failure were very different since PBX 0298 fails at about 1% strain, whilst PBX 9501 failed at less than half this value. The remaining three materials, PRX 0344, 0407 and 9502, exhibited very similar tensile strengths, particularly 0407 and 0344. The stress-strain curves for these materials (an example is given in Figure 13) show a much more brittle behaviour. Although the tensile strengths of 0344 and 0407 are very close, the failure strain of 0344 is significantly smaller than 0407. If the tensile strengths of 0407 and 9502 are compared, together with their compositions, it appears that the replacement of TATB (IHE) by a TATB/PETN mixture, significantly increases the tensile strength of the composite without affecting its strain to failure. Replacing TATB by a TATB/HMX mixture (as in 0344) also increases the tensile strength by a similar amount, although the strain to failure is reduced. This may be due to the HMX component, as this is a weaker and more brittle crystal than PETN, and may be more susceptible to fracture as a result of deformation twinning²³. Since neither of the two weakest materials contained the KEL-F binder, it is not possible to ascertain the influence of the binder on the mechanical properties of the composites. Consequently it may be the large volume fractions of

HMX, or the replacement binders, that are responsible for the low tensile strengths of 0298 and 9501.

Figure 14 is an example of a fracture path in PBX 9501. The sample was stressed in the Brazilian geometry (figure 3). In this case there is little or no evidence of crystal fracture except at the bottom left of the picture. The most striking feature is the amount of interfacial failure with the fracture path predominantly following the boundaries of crystals.



FIGURE 14. THE FRACTURE PATH IN PBX 9501.

An example of time lapse photography is given in figure 15 for PBX X-0298 again loaded in the

Brazilian test. This sample failed at a load of 1.64 kgf corresponding to a tensile stress of 1.28 MPa at a time of 167 s after start of loading ($\dot{\epsilon} \approx 10^{-4} \text{ s}^{-1}$). The frames were recorded at 8 s intervals. Failure started at three separate sites (arrowed in frame (a)). Note that the upper failure propagated through two crystals whilst the lower failures propagated along crystal boundaries and through the matrix. By frame (d) a continuous fracture path had developed. The value of the time-lapse photography is that it shows that multiple nucleation sites can be involved and that tears in the binder can initiate interfacial debonding, as well as crystal fracture.

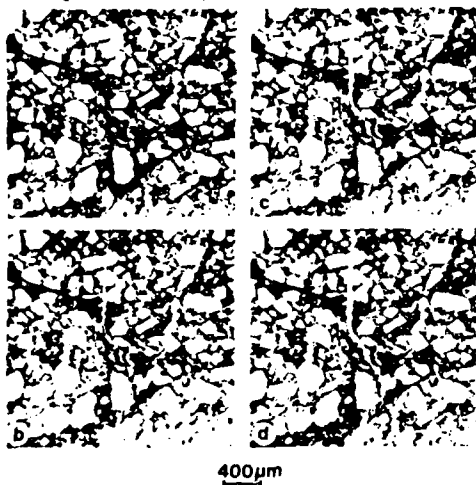


FIGURE 15. A TIME LAPSE PHOTOGRAPHIC SEQUENCE FOR PBX X - 0298.

ACKNOWLEDGEMENTS

This work was supported by grants from MOD (Procurement Executive) and the U.S. European Office on contact DAJA45-85-C-0052.

REFERENCES

1. Blackwood, J. D. and Bowden, F. P., *Proc. Roy. Soc. Lond.*, Vol A 213, 1952, p285.
2. Heavens, S. N., PhD Thesis, University of Cambridge, 1973.
3. Heavens, S. N. and Field, J. E., *Proc. Roy. Soc. Lond.*, Vol A 338, 1974, p77.
4. Swallowe, G. M., PhD Thesis, University of Cambridge, 1979.
5. Swallowe, G. M. and Field, J. E., *Proc. Roy. Soc. Lond.*, Vol A 379, 1982, p389.
6. Field, J. E., Swallowe, G. M. and Heavens, S.N., *Proc. Roy. Soc. Lond.*, Vol A 382, 1982, p231.
7. Krishna Mohan, V. and Field, J.E., *Combustion and Flame*, Vol 56, 1984, p269.
8. Krishna Mohan,V, Field, J. E. and Swallowe G. M., *Combustion Sci. and Tech.*, Vol 44, 1984, p269.
9. Field, J. E., Palmer, S. J. P., Pope P. H., Sundarajan, R. and Swallowe, G.M., *Proc. 8th Int. Symp. on Detonation*, Albuquerque, U.S.A. 1985.
10. Kolsky, H., "Stress waves in solids", Dover, New York, 1963.
11. Gorham, D. A., *Inst. Phys. Conf. Ser.*, Vol 47, 1979, p16.
12. Pope, P.H. and Field, J.E., *J. Phys. E.*, Vol 17, 1984, p817.
13. Awaji, H. and Sato, S., *J. Eng. Mater. and Tech.*, Vol 101, 1979, p140.
14. Johnson, H. D., MH SMP-78-08, 1979, Amarillo, Texas.
15. Johnson, H. D., MH SMP-79-26, 1979, Amarillo, Texas.
16. Johnson, H. D., MH SMP-81-22, 1981, Amarillo, Texas.
17. Chiang, F. P. *Opt. Eng.*, Vol 21, 1982, p379.
18. Ennos, A. E., "Laser speckle and related phenomena", edited by J. C. Dainty, Springer, Heidelberg, 1975, pp. 203-253.
19. Huntley, J. M., *J. Phys. E.*, Vol 19, 1986, p43.
20. Coffey, C. S. and Jacobs, S. J., *J. Appl. Phys.*, Vol 52, 1981, p6991.
21. Swallowe, G. M., Field, J. E. and Horn, L. A., *J. Mater. Sci.*, Vol 21, 1986, 4089.
22. Winter, R. E. and Field, J. E., *Proc. Roy. Soc. Lond.*, Vol A 343, 1975, p399.
23. Palmer, S. J. P. and Field, J. E., *Proc. Roy. Soc. Lond.*, Vol A 383, 1981, p399.

Speckle photography fringe analysis: assessment of current algorithms

J. M. Huntley

The accuracy and reliability of four fringe analysis algorithms have been assessed, using Young's fringe patterns calculated from computer generated speckle patterns. The 1-D integration, 1-D autocorrelation, 2-D Fourier transform, and 2-D Walsh transform methods all estimated the two in-plane displacement components with negligible systematic error; the random errors were found to vary in proportion to $\sigma \cdot VR$ (speckle diameter = σ , fringe visibility = V , and radius of laser probe beam = R), with the lowest errors given by the 2-D Fourier transform method.

I. Introduction

Double exposure speckle photography¹ is a widely used technique for measuring in-plane displacements in solid and fluid mechanics. To extract the displacement field, the photograph is probed point by point with a narrow laser beam: the spacing and angle of the Young's fringes which modulate the diffraction halo determine the local displacement vector. Automation of such a repetitive task is highly desirable. However, estimation of the two spatial frequency components, (k_m, k_n) of the fringes from a digitized pattern, is not a straightforward process because of the noise which modulates the fringes. References 2-12 are a small selection from the recent literature describing automatic systems and algorithms designed specifically for the case of Young's fringes from a speckle photograph. The purpose of this paper is to provide an objective comparison of four such algorithms: the 1-D integration,^{2,3} 1-D autocorrelation,² 2-D Fourier transform,⁴ and 2-D Walsh transform methods.⁵

The assessment of the four algorithms was made using a set of 320 standard fringe patterns, which were calculated from computer generated speckle patterns. The main advantage of simulated over real fringes is that they are well characterised: the speckle displacement is known precisely, with no systematic drifts or instrumental artefacts. The first part of the paper describes the method used to generate the patterns.

This is followed by the results of the tests, in which the main topics under investigation were the reliability (i.e., success rate in detecting the presence of the fringes) and the accuracy (i.e., standard deviation of the estimators k_m and k_n).

II. Computer Generated Fringe Patterns

The Young's fringes from a double exposure speckle pattern are themselves contaminated by speckle noise, which must be included in any realistic computer simulation. The most direct way of doing this is to model the entire process of recording and pointwise filtering a speckle photograph. By carrying out the speckle experiment in the computer, the effects of parameters such as the aperture ratio of the lens, the radius of the laser probe, speckle decorrelation, and film characteristics can be readily studied.

A. Speckle Pattern Formation

Consider the 4 planes shown in Fig. 1. Plane 1 is the pupil plane of the lens used to image the object onto the photographic plate (Plane 2). The position of the object plane does not affect the speckle statistics in Plane 2, provided the speckle size in Plane 1 is small compared with the diameter, D , of the pupil; in effect, the pupil plane is treated as a uniformly bright rough surface.¹³ After development, the photograph (now in Plane 3) is probed by a laser beam and the diffraction pattern is observed in Plane 4.

The complex amplitude and intensity of the light at position (x_j, y_j) in each of the 4 planes will be denoted by $A_j(x_j, y_j)$ and $I_j(x_j, y_j)$ respectively ($j = 1, 2, 3, 4$). A_j and I_j are sampled on a square mesh (m_i, n_i) , where $m_i, n_i = 0, 1, 2, \dots, N - 1$ and the point $m_i = n_i = 0$ corresponds to $x_j = y_j = 0$. The sampled arrays will be denoted by A_{jmn} and I_{jmn} .

The author is with University of Cambridge, Cavendish Laboratory, Cambridge CB3 OHE, U.K.

Received 19 January 1989.

0003-6835/89/204316-07\$02.00/0.

© 1989 Optical Society of America.

The sampling rates are chosen in accordance with the Shannon sampling theorem to be twice the highest spatial frequency of A_1 (Planes 1 and 3) or I_1 (Planes 2 and 4), which results in the following distances Δ_j between sample points:

$$\Delta_1 = 2D/N \quad (1)$$

$$\Delta_2 = \lambda d_{12}/2D \quad (2)$$

$$\Delta_3 = \lambda d_{12}/2D \quad (3)$$

$$\Delta_4 = 2Dd_{14}/Nd_{12} \quad (4)$$

d_{12} and d_{14} are the distances between Planes 1 and 2, and 3 and 4, respectively, and λ is the wavelength of the light, which is assumed to be plane polarised. Δ_2 and Δ_3 are both $\sigma/2.4$ where σ is the subjective speckle diameter¹

$$\sigma = 1.2\lambda d_{12}/D \quad (5)$$

The position of datapoint (m_j, n_j) in Planes 2 and 3 is given by

$$\begin{aligned} x_j &= \Delta_j m_j & m_j &= 0, 1, 2, \dots, N/2 - 1 \\ y_j &= \Delta_j n_j & n_j &= 0, 1, 2, \dots, N/2 - 1 \\ j &= 2, 3 \end{aligned} \quad (6)$$

A_1 and A_4 are calculated from A_2 and A_3 by the discrete Fourier transform so that aliasing modifies Eq. (6) for Planes 1 and 4:

$$\begin{aligned} x_j &= \Delta_j m_j & m_j &= 0, 1, 2, \dots, N/2 - 1 \\ &= \Delta_j(m_j - N) & m_j &= N/2, \dots, N - 1 \\ y_j &= \Delta_j n_j & n_j &= 0, 1, 2, \dots, N/2 - 1 \\ &= \Delta_j(n_j - N) & n_j &= N/2, \dots, N - 1 \\ j &= 1, 4 \end{aligned} \quad (7)$$

The 2-D discrete Fourier transform operator, \mathcal{J} , is defined by

$$\begin{aligned} A_{kpq} &= \mathcal{J}(A_{jmn}) \\ &= (1/N) \sum_{m=0}^{N-1} \sum_{n=0}^{N-1} A_{jmn} \exp(-2\pi i(kp + nq)/N); \end{aligned} \quad (8)$$

\mathcal{J}^{-1} is used to represent the corresponding inverse operation.

The fields A_1 and A_2 are related by the Huygens-Fresnel principle, expressed in the Fresnel approximation as¹³

$$\begin{aligned} A_2(x_2, y_2) &= (1/\lambda d_{12}) \exp(-i\pi(x_2^2 + y_2^2)/\lambda d_{12}) \int_{-\infty}^{\infty} \int_{-\infty}^{\infty} A_1(x_1, y_1) \\ &\times \exp(-i\pi(x_1^2 + y_1^2)/\lambda d_{12}) \\ &\times \exp(i2\pi(x_2 x_1 + y_2 y_1)/\lambda d_{12}) dx_1 dy_1 \end{aligned} \quad (9)$$

Two further functions $A_1'(x_1, y_1)$ and $A_2'(x_2, y_2)$ are introduced:

$$A_1'(x_1, y_1) = A_1(x_1, y_1) \exp(-i\pi(x_1^2 + y_1^2)/\lambda d_{12}); \quad (10)$$

$$A_2'(x_2, y_2) = A_2(x_2, y_2) \exp(i\pi(x_2^2 + y_2^2)/\lambda d_{12}). \quad (11)$$

Equation (9) shows A_1' and A_2' to be related to one another by the Fourier transform. The usual assumption

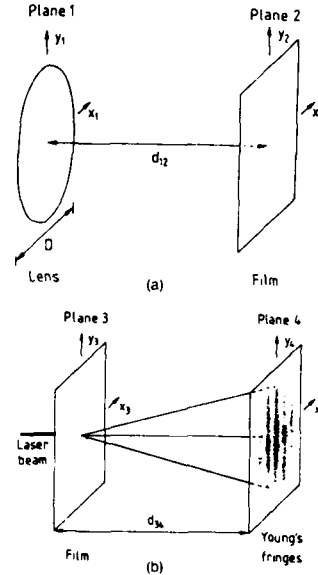


Fig. 1. Simulation of Young's fringe patterns; relative orientation of Planes 1-4: (a) and (b) are the arrangements for exposure and pointwise filtering of a speckle photograph.

tions regarding the statistical properties of A_1 (i.e., that Plane 1 consists of a large number of independent scatterers, with the phases uniformly distributed over $[-\pi, \pi]$) will be adopted here. Under these circumstances, the real and imaginary parts of A_2 and A_2' at any point (x_2, y_2) are independent Gaussian random variables.¹³

The simulation is started by filling the real and imaginary parts of A_{2mn} with random numbers from a Gaussian distribution with a mean of zero and standard deviation of unity. The effect of the lens is produced by transformation to Plane 1, multiplication by a window function W_{1mn} , followed by transformation back to Plane 2. The speckle pattern I_{2mn} is the modulus squared of this low-pass filtered amplitude distribution:

$$I_{2mn} = |\mathcal{J}^{-1}(W_{1pq}\mathcal{J}(A_{2mn}))|^2. \quad (12)$$

W_{1mn} is defined by $W_1(x_1, y_1)$ and Eq. (7), where

$$\begin{aligned} W_1(x_1, y_1) &= 1 & x_1^2 + y_1^2 &\leq (D/2)^2 \\ &= 0 & x_1^2 + y_1^2 &> (D/2)^2 \end{aligned} \quad (13)$$

for a circular iris. After the filtering operation described by Eq. (12), I_{2mn} is renormalized so that $\langle I_{2mn} \rangle = 1$. Figure 2 shows a speckle pattern generated in this way. The lens was stopped down to produce a large speckle diameter for illustration purposes by reducing D by a factor of 4 while keeping Δ_1 and Δ_2 unchanged.

A linear film response is assumed, so that the light amplitude in Plane 3 can be written:

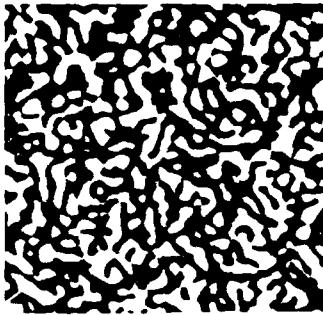


Fig. 2. Computer generated speckle pattern I_{2mn} ($m,n = 0,1,2..255$).

$$A_{3mn} = W_{3mn}(\alpha - \beta I_{2mn}), \quad (14)$$

where α and β are constants. A nonlinear response can of course be incorporated into the model, provided the sampling rate is increased sufficiently to prevent aliasing. W_{3mn} is a Gaussian window to simulate the usual laser beam profile:

$$W_{3mn} = \exp(-\Delta_3^2 r_3^2/R^2),$$

where

$$r_3^2 = (m_3 - N/2)^2 + (n_3 - N/2)^2 \quad (15)$$

and R is the effective radius of the laser beam. R/Δ_3 never exceeded $0.2N$ due to aliasing considerations. A_4 is related to A_3 by an equation similar to Eq. (9), which reduces to the Fraunhofer relationship provided $R^2/\lambda d_{34}$ is sufficiently small. I_4 is therefore calculated as

$$I_{4pq} = |\mathcal{F}(A_{3mn})|^2. \quad (16)$$

In Figs. 3–5 some of the first and second order statistical properties of the speckle pattern simulations are compared with the theoretical behavior. Figure 3 shows the probability density function for I_{2mn} as determined from an array of 256×256 datapoints. The continuous line is the expected negative exponential curve¹³ defined by

$$\begin{aligned} P(I_2) &= (1/(I_2)) \exp(-I_2/(I_2)) & I_2 \geq 0 \\ &= 0 & I_2 < 0 \end{aligned} \quad (17)$$

Figure 4 is a typical diffraction halo I_{4mn} . The radial intensity distribution $I_{\text{obs}}(\rho)$ obtained by averaging sixteen such halos (see Fig. 5) is in good agreement with the theoretical curve¹³ I_{th} :

$$\begin{aligned} I_{\text{th}}(\rho) &= \cos^{-1}\rho - \rho(1-\rho^2)^{1/2} & \rho \leq 1 \\ &= 0 & \rho > 1 \end{aligned}$$

where

$$\rho = (x_i^2 + y_i^2)^{1/2} d_{12}/D d_{14}. \quad (18)$$

B. Double Exposure Speckle Pattern

The method used here to create a displaced second speckle pattern is the digital equivalent of a shearing

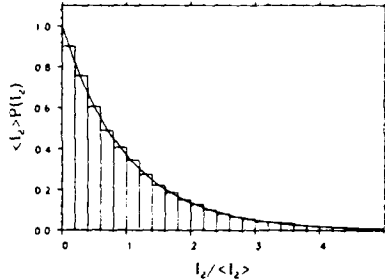


Fig. 3. Probability density function of intensity in Plane 2. Results from one 256×256 pixel computer generated speckle pattern. The solid curve is the expected negative exponential distribution.

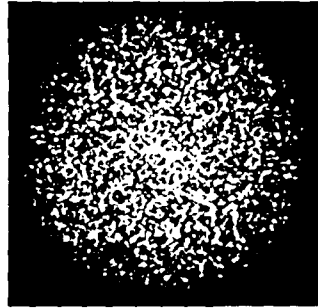


Fig. 4. Typical diffraction halo I_{4mn} calculated from a computer generated speckle pattern.

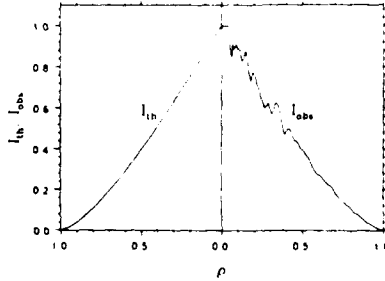


Fig. 5. Comparison of theoretical (I_{th}) and observed (I_{obs}) diffraction halo profiles. I_{obs} is the average from 16 independent halos similar to that shown in Fig. 4.

element in Plane 1. Multiplication of A_{1mn} by $\exp(-2\pi i(k_m m_1 + k_n n_1)/N)$ moves I_{2mn} by (k_m, k_n) pixels. k_m and k_n can be nonintegral, resulting in a nonintegral number of fringes in I_{4mn} : the most severe test of the transform methods of fringe analysis is when both k_m and k_n are halfway between adjacent integers. When performed digitally, the data is in fact shifted cyclically. The speckle patterns are therefore created in ar-

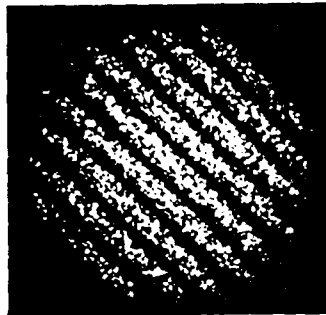


Fig. 6. Typical Young's fringe pattern I_{4mn} calculated from a double exposure speckle pattern. Fringe visibility = 1.0.

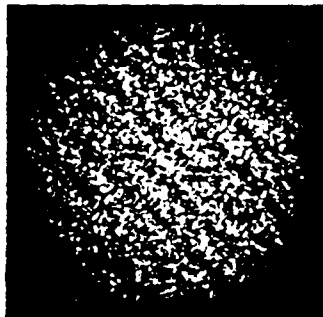


Fig. 7. Typical Young's fringe pattern I_{4mn} calculated from a double exposure speckle pattern. Fringe visibility = 0.5.

rays of 320 by 320 pixels, with only 256 by 256 pixels being retained in subsequent calculations. This allows displacements of up to (64,64) pixels to be made without speckles disappearing off one edge of the array and then reappearing across the opposite edge. The first exposure is made with I_{2mn} , the second with the displaced speckle pattern, denoted by I_{2mn}^d ($= |A_{2mn}^d|^2$). In practical applications there may be partial decorrelation of the two patterns, due to out-of-plane tilt or changes in the scattering surface. This can be simulated by adding an independent speckle pattern, A_{2mn}' , to A_{2mn}^d :

$$I_{2mn}^d = [(1 - \delta)A_{2mn}^d + \delta A_{2mn}']^2. \quad (19)$$

I_{2mn}^d is renormalized to give a mean intensity of unity; Eq. (14) then becomes

$$A_{2mn} = W_{2mn}(\alpha - \beta I_{2mn} + I_{2mn}^d) \quad (20)$$

for the double exposure case. The decorrelation parameter δ ranges between 0 and 1, which represents cases of complete correlation and decorrelation, respectively. It can be shown that for speckle patterns obeying negative exponential statistics, the visibility, V , of the fringes in Plane 4 is given by

$$V = (\delta - 1)^2 / (1 - 2\delta + 2\delta^2) \quad (21)$$

Figures 6 and 7 show two typical fringe patterns: $\delta = 0.0$ ($V = 1.0$) in Fig. 6; $\delta = 0.5$ ($V = 0.5$) in Fig. 7.

III. Comparison of Algorithms

The computer model was used to generate a total of 320 fringe patterns, subdivided into 10 datasets of 32 images, with an image size of $N \times N$ pixels ($N = 256$). The 10 sets of input parameters are listed in Table I. The patterns allow the effects of displacement angle (compare datasets 1 and 2), displacement magnitude (2, 4, and 5), film characteristics (2 and 3), laser probe radius (4, 6, and 7), and speckle decorrelation (2, 8, 9, and 10) to be investigated. The fringe patterns within each dataset were generated with the same input parameters, but from independent speckle patterns, to allow statistically significant conclusions to be drawn about the relative performance of the four fringe analysis algorithms. The main features of the algorithms are described briefly below.

In the 1-D integration method, the image is integrated along lines parallel to the fringes to create a 1-D signal. This is analysed by 1-D Fourier transformation, with the fringe spacing estimated from the position of the peak in the spectrum. Although carried out originally by optical means,^{6,7} the integration is now more usually implemented in software.^{2,3} This is the fastest of the four methods, but unlike the others requires manual assistance in the form of the fringe direction. Robinson has described an algorithm for automatic determination of the fringe direction,³ although this only uses a small fraction of the image and so has fairly low noise immunity.

The 1-D autocorrelation method² involves calculating the autocorrelation function of each row of the image. This eliminates the phase shift between rows, so that the autocorrelations can be averaged directly. k_m is obtained from the position of the peak in the Fourier spectrum of this 1-D signal. k_n is estimated in the same way, but operating on the image by columns rather than by rows.

The 2-D Fourier transform⁴ estimate of (k_m, k_n) is the position of the peak in the 2-D continuous Fourier spectrum of the fringes. An initial estimate, the peak position in the 2-D discrete Fourier spectrum, is re-

Table I. Parameters Used to Generate Ten Datasets of Young's Fringe Patterns

Dataset	k_m	k_n	k	α	β	(R/Δ)	δ
1	10.0	0.0	10.000	0	-1	0.20N	0.0
2	7.5	7.5	10.607	0	-1	0.20N	0.0
3	7.5	7.5	10.607	10	1	0.20N	0.0
4	3.5	3.5	4.950	0	-1	0.20N	0.0
5	15.5	15.5	21.920	0	-1	0.20N	0.0
6	3.5	3.5	4.950	0	-1	0.10N	0.0
7	3.5	3.5	4.950	0	-1	0.05N	0.0
8	7.5	7.5	10.607	0	-1	0.20N	0.5
9	7.5	7.5	10.607	0	-1	0.20N	0.667
10	7.5	7.5	10.607	0	-1	0.20N	0.75

fined by an iterative method. Three fringes are required within the diffraction halo, compared with four to five for the autocorrelation method.

A similar approach is adopted in the last of the four algorithms,⁵ except that a 2-D Walsh transform instead of the discrete Fourier transform provides the initial estimate of (k_m, k_n) ; this estimate is then refined by a square wave transform rather than by the continuous Fourier transform. The two algorithms are compared in Ref. 8. The accuracies are similar and, although the Walsh method is less reliable with low visibility fringes, the number of multiplications is much reduced so that it can run significantly faster when implemented on a microcomputer.

Before application of the algorithms to the 320 fringe patterns, the intense undiffracted peak of each image was set to zero (the equivalent of a beam stop). In datasets 1, 2, 3, 4, 5, 8, 9, and 10, all points within a radius of 4.0 pixels of the undiffracted peak were set to zero; the radius of the beam stop was increased to 5.0 and 9.0 for datasets 6 and 7 respectively. The positive bias was then removed by subtracting the diffraction halo given by Eq. (18). On a real system, the intensity profile may deviate from that given by Eq. (18), and it would then be advisable to estimate the profile by averaging diffraction halos from a single exposure speckle photograph.⁴

The exact value of fringe angle θ was used when performing the 1-D integrations. In the implementation of the 1-D autocorrelation method, the autocorrelations were simply averaged without the normalization or windowing suggested in Ref. 2. In both cases, the spacing of the fringes in the integrated or averaged signal was estimated by 1-D Fourier analysis: the position of the principal peak in the spectrum was identified and then refined by a bounded Newton-Raphson method. Details are given in Appendix (ii) of Ref. 4. The 2-D Fourier and Walsh transform algorithms were implemented as described in Refs. 4 and 5. All four algorithms were coded in FORTRAN 77, to run on an IBM 3084 mainframe computer.

The results obtained with the four methods are given in Tables II-V. S.R. is the success rate, the criterion adopted in deciding whether or not the fringes had been successfully detected, was that the estimated values of both k_m and k_n should be within 0.5 of the true values or in the case of the 1-D integration method that the estimate of $k = (k_m^2 + k_n^2)^{1/2}$ should be correct to within 0.5. The means and standard deviations of (k_m, k_n) were estimated from all the results, which were deemed to be successful. The estimates of the means are shown in Tables II-V as (\bar{k}_m, \bar{k}_n) ; the figures in parentheses represent the uncertainty in the last significant figure. As expected, the standard deviations of k_m and k_n were not found to be significantly different from one another and were therefore combined to give a more reliable estimate, s , of the true standard deviation, with lower and upper 95% confidence limits denoted by s_l and s_u , respectively. In the case of Table II (the 1-D integration method), the results are given in terms of the vector (k, θ) , the polar form of (k_m, k_n) .

Table II. Results of Analysis of Ten Datasets by the 1-D Integration Method

Dataset	S.R. (%)	V	\bar{k}	θ	s	s_l	s_u
1	100	0.99	10.067(4)	1.5708	0.025	0.020	0.033
2	100	0.99	10.602(4)	0.7854	0.025	0.020	0.034
3	100	0.99	10.600(5)	0.7854	0.029	0.023	0.038
4	100	1.00	4.949(4)	0.7854	0.025	0.020	0.033
5	100	0.92	21.911(6)	0.7854	0.034	0.027	0.045
6	100	0.99	4.946(9)	0.7854	0.049	0.039	0.065
7	100	0.95	4.890(18)	0.7854	0.102	0.081	0.136
8	100	0.48	10.606(11)	0.7854	0.063	0.050	0.084
9	100	0.21	10.631(26)	0.7854	0.149	0.119	0.199
10	63	0.16	10.647(46)	0.7854	0.207	0.157	0.303

Table III. Results of Analysis of Ten Datasets by the 1-D Autocorrelation Method

Dataset	S.R. (%)	V	\bar{k}_m	\bar{k}_n	s	s_l	s_u
1	100	0.99	10.014(8)	0.000(0)	0.043	0.035	0.058
2	100	0.99	7.493(5)	7.503(5)	0.026	0.022	0.032
3	100	0.99	7.497(6)	7.493(6)	0.034	0.029	0.041
4	100	1.00	3.509(5)	3.492(4)	0.025	0.021	0.031
5	100	0.92	15.496(6)	15.488(6)	0.035	0.029	0.042
6	100	0.99	3.482(13)	3.497(8)	0.062	0.053	0.076
7	100	0.95	3.429(21)	3.459(20)	0.114	0.097	0.138
8	100	0.48	7.506(15)	7.491(10)	0.073	0.062	0.088
9	63	0.21	7.521(40)	7.500(36)	0.169	0.135	0.226
10	6	0.16	7.722(67)	7.399(67)	0.078	0.044	0.287

Table IV. Results of Analysis of Ten Datasets by the 2-D Fourier Transform Method

Dataset	S.R. (%)	V	\bar{k}_m	\bar{k}_n	s	s_l	s_u
1	100	0.99	10.007(4)	-0.002(5)	0.026	0.022	0.032
2	100	0.99	7.494(5)	7.501(4)	0.025	0.021	0.030
3	100	0.99	7.496(5)	7.495(5)	0.027	0.023	0.033
4	100	1.00	3.505(4)	3.494(4)	0.023	0.019	0.028
5	100	0.92	15.498(6)	15.488(6)	0.031	0.027	0.038
6	100	0.99	3.489(10)	3.509(7)	0.047	0.040	0.057
7	100	0.95	3.453(17)	3.457(17)	0.095	0.081	0.116
8	100	0.48	7.503(11)	7.498(10)	0.061	0.052	0.074
9	94	0.21	7.532(20)	7.514(27)	0.121	0.111	0.159
10	19	0.16	7.416(9)	7.438(58)	0.195	0.140	0.335

Table V. Results of Analysis of Ten Datasets by the 2-D Walsh Transform Method

Dataset	S.R. (%)	V	\bar{k}_m	\bar{k}_n	s	s_l	s_u
1	100	0.99	10.006(5)	0.000(5)	0.026	0.022	0.032
2	100	0.99	7.494(5)	7.497(5)	0.027	0.023	0.032
3	100	0.99	7.498(6)	7.499(5)	0.030	0.025	0.036
4	100	1.00	3.510(5)	3.492(5)	0.027	0.023	0.032
5	100	0.92	15.497(6)	15.488(6)	0.032	0.027	0.039
6	100	0.99	3.490(11)	3.500(7)	0.050	0.043	0.061
7	100	0.95	3.396(19)	3.392(18)	0.104	0.088	0.127
8	100	0.48	7.503(11)	7.494(11)	0.061	0.052	0.074
9	88	0.21	7.522(24)	7.519(28)	0.138	0.117	0.168
10	16	0.16	7.536(84)	7.360(107)	0.203	0.140	0.370

The values of s are the estimates of the standard deviation of \bar{k} , which can be compared directly with the standard deviations of k_m and k_n given in Tables III-V.

IV. Discussion

Several interesting observations emerge from the results listed in Tables II-V. First, the mean values k_m , k_n and \bar{k} are not significantly different from the true values in nearly all cases (compare k_m , k_n and \bar{k} in Tables II-V with k_m , k_n and \bar{k} in Table I). The only significant discrepancy is with dataset 7, where k_m , and k_n are both 0.05-0.1 lower than the true values. In general, therefore, the systematic errors are less important than the random errors.

The second observation is that the four algorithms all result in comparable random errors for any given dataset (compare s in Tables II-V). The 2-D Fourier transform method has the lowest random errors; the errors associated with the 1-D integration, 2-D Walsh Transform, and 1-D autocorrelation methods are about 5%, 8% and 24% higher on average. The reliabilities of the four algorithms follow a similar trend, except that the 1-D integration method appears to be the most successful. In practice, manual (or computer) estimation of θ would carry its own probability of failure which is not taken into account here.

The final point of interest concerns the variation in standard deviation amongst the ten datasets under investigation. Comparison of datasets 1 and 2, and of 2, 4, and 5 of Table IV shows that the accuracy is not significantly affected by either displacement angle or magnitude. The slightly larger error resulting from dataset 5 can be attributed to the reduced fringe visibility due to the increased speckle pattern displacement. This observation is consistent with a uniform distribution of the noise over the central region of the 2-D Fourier transform plane: the signal peak is shifted slightly by the noise, giving rise to an error whose standard deviation is independent of the peak position.

The standard deviations from datasets 2 and 3 are comparable, suggesting that the values of the film transmission parameters, α and β , are not important. This is reasonable because α and β simply act as scaling factors for the undiffracted peak and diffraction halo, respectively; the undiffracted peak is removed before analysis so that a large value for α (dataset 3) should not affect the results.

By contrast, the fringe visibility V , and laser probe radius, R , both influence the accuracy considerably. The standard deviation, s , appears to vary as $1/R$ (datasets 4, 6, and 7) and as $1/V$ (datasets 2, 8, 9, and 10). The random error e to be expected in a real experiment is

$$e = s \Delta_1 \quad (22)$$

Δ_1 is $\sigma/2.4$, and taking the value $s = 0.025$ from dataset 2 ($V = 1$; $(R/\Delta_1) = 51.2$) therefore suggests the empirical relationship

$$e \approx 0.22\sigma^2/VR \quad (23)$$

Substitution of typical values $\sigma = 5 \mu\text{m}$, $R = 0.5 \text{ mm}$, and $V = 1$ into Eq. (23) results in a standard deviation of 11 nm. For comparison, the random errors produced by a real analysis system are typically a few tens of nm with good visibility fringes.⁸

Equation (23) assumes that the image digitizer adequately samples the diffraction pattern. In Sec. II, it was found that R/Δ_1 had to be kept below about 0.2 N to prevent aliasing when calculating the diffraction pattern. This implies a lower limit of

$$N = 12R/\sigma \quad (24)$$

on the required resolution ($N \times N$) of the image digitizer. On the basis of the figures given above, N would need to be greater than 1200. Common values in practice are 64, 128, or 256, so that aliasing of high frequency noise may increase the random errors considerably. The digitization of an image by a sensor array is equivalent to convolution of the image with the sampling function for a single sensor, followed by sampling with a delta function at the centre of each sensor. By the convolution theorem, the Fourier transform of the fringe pattern is multiplied by the Fourier transform of the sampling function. The cutoff spatial frequency, above which the noise is significantly attenuated, decreases as the dimensions of the sensor elements are increased. The aliasing errors can, therefore, be reduced by choosing a detector array with a large a sampling area per element as possible. Provided $|k_m|, |k_n| \ll N$, the optimum situation is one in which each element consists of a square of side equal to the distance between the centres of adjacent elements. Under these circumstances, noise with spatial frequency components equal to a multiple of the sampling frequency, which would have been aliased onto the zero frequency term, is exactly cancelled, with substantial cancellation at the signal peak (k_m, k_n). Equation (23) would then still be valid despite the undersampling.

V. Conclusions

Four fringe analysis algorithms from the recent literature have been compared using computer generated fringes. The fringes were simulated by a rigorous model for the speckle pattern recording and pointwise filtering processes.

The systematic errors from all four algorithms were found to be negligible. Much analysis has appeared in recent papers on fringe shifting due to the diffraction halo; these errors are made negligible by simply subtracting the diffraction halo from the fringe pattern.

For all four algorithms, the random errors were found to vary in proportion to σ^2/VR . The 2-D Fourier transform method gave the lowest random errors (standard deviation in each displacement component $\approx 0.22\sigma^2/VR$). The accuracies of the 1-D integration, 2-D Walsh transform, and 1-D autocorrelation methods were slightly poorer, with an average increase in standard deviation of 5%, 8%, and 24%, respectively. The reliabilities followed a similar trend: at a fringe

visibility of 20%, the success rate in detecting the fringes was 94%, 88%, and 63% for the 2-D Fourier transform, 2-D Walsh transform, and 1-D autocorrelation methods. The corresponding figure for the 1-D integration method was 100% once the fringe angle was known. This is also the fastest algorithm but determination of the fringe angle requires manual assistance. Of the remainder, the 2-D Walsh transform method will run the fastest; it is however the most complex to code. The computation times of the 2-D Fourier transform and 1-D autocorrelation methods are comparable, provided the autocorrelations are calculated by the Fast Fourier Transform. 2-D Fourier analysis requires no more than three fringes within the diffraction halo, compared with four to five for the 1-D autocorrelation technique. The latter breaks down if the fringes are nearly horizontal or vertical, so that it is necessary to evaluate autocorrelations along at least one extra independent direction. Out of the four algorithms under investigation, the 2-D Fourier transform method would therefore be recommended as the preferred choice under most circumstances.

A final point on the hardware aspect is that typical values of σ , R and N will result in considerable undersampling of the noise in the fringe patterns. The sampling area of each element is then as important as the number of pixels in the array. The optimum choice is a square element of side equal to the interpixel distance.

References

1. A. E. Ennos, "Speckle Interferometry," in *Laser Speckle and Related Phenomena*, J. C. Dainty, Ed. (Springer-Verlag, Berlin, 1975), pp. 203-253.
2. R. Meynart, "Instantaneous Velocity Field Measurements in Unsteady Gas Flow by Speckle Velocimetry," *Appl. Opt.* **22**, 535-540 (1983).
3. D. W. Robinson, "Automatic Fringe Analysis with a Computer Image-Processing System," *Appl. Opt.* **22**, 2169-2176 (1983).
4. J. M. Huntley, "An Image Processing System for the Analysis of Speckle Photographs," *J. Phys. E* **19**, 43-48 (1986).
5. J. M. Huntley, "Speckle Photography Fringe Analysis by the Walsh Transform," *Appl. Opt.* **25**, 382-386 (1986).
6. B. Ineichen, P. Eglin, and R. Dandliker, "Hybrid Optical and Electronic Image Processing for Strain Measurements by Speckle Photography," *Appl. Opt.* **19**, 2191-2195 (1980).
7. G. H. Kaufmann, A. E. Ennos, B. Gale, and D. J. Pugh, "An Electrooptical Read-out System for Analysis of Speckle Photographs," *J. Phys. E* **13**, 579-584 (1980).
8. J. M. Huntley, "Fast Transforms for Speckle Photography Fringe Analysis," *Opt. Lasers Eng.* **7**, 149-161 (1986-7).
9. H. D. Navone and G. H. Kaufmann, "Two-dimensional Digital Processing of Speckle Photography Fringes - 3. Accuracy in Angular Determination," *Appl. Opt.* **26**, 154-156 (1987).
10. A. Kirita, C. J. D. Pickering, and N. A. Halliwell, "Particle Image Velocimetry: A New Approach to Fringe Analysis," *Opt. Lasers Eng.* **7**, 137-147 (1986-7).
11. R. Erbeck, "Fast Image Processing with a Microcomputer Applied to Speckle Photography," *Appl. Opt.* **24**, 3838-3841 (1985).
12. D. J. Chen and F. P. Chiang, "Digital Processing of Young's Fringes in Speckle Photography," *Proc. Soc. Photo-Opt. Instrum. Eng.* **954**, 310-320 (1988).
13. J. W. Goodman, "Statistical Properties of Laser Speckle Patterns," in *Laser Speckle and Related Phenomena*, J. C. Dainty, Ed. (Springer-Verlag, Berlin, 1975), pp. 9-75.

The author is grateful to J. E. Field for his interest in the project and to the Science and Engineering Research Council and Gonville and Caius College, Cambridge, for support in the form of Research Fellowships.

High resolution moire photography: application to dynamic stress analysis

J. M. Huntley

J. E. Field

University of Cambridge
Cavendish Laboratory
Madingley Road
Cambridge CB3 OHE, England

Abstract. The techniques of high resolution moire photography and high speed photography have been combined to allow simultaneous measurement of both in-plane components of a transient displacement field with microsecond time resolution. A 150 lines/mm⁻¹ specimen grating is imaged onto a reference grating with a specially modified camera lens. The resulting real-time moire fringes are recorded with a high speed image converter camera. An automatic fringe analysis technique based on the 2-D Fourier transform method is used to extract the displacement information from the high speed sequences. The techniques are illustrated by the results of an investigation into the transient deformation of polymethyl methacrylate caused by solid particle impact.

Subject terms: high resolution moire, high speed photography, Fourier transform method, automatic fringe analysis, impact

Optical Engineering 28(8), 926-933 (August 1989)

CONTENTS

1. Introduction
2. Lens modification
3. Formation of real-time moire fringes
4. Dynamic stress field due to solid particle impact
5. Automatic fringe analysis
6. Conclusions
7. Acknowledgments
8. References

1. INTRODUCTION

High resolution moire photography is an incoherent optical technique, developed from the classic moire grid method by Burch and Forno,¹ for measuring in-plane displacement or deformation. The main feature of the technique is the use of a masked lens for recording the photographs. The mask tunes the lens to the spatial frequency of the specimen grating, resulting in an image of high contrast, with reduced susceptibility to lens aberrations. One further advantage is a three- to fourfold improvement in the depth of field.

Burch and Forno used their technique to study the deformation of large engineering structures: the specimen grating

frequency, typically a few lines/mm⁻¹ ($i \cdot \text{mm}^{-1}$), and demagnification were chosen to produce an image plane frequency of 300 $i \cdot \text{mm}^{-1}$. Double-exposure photographs were recorded on a high resolution emulsion and were subsequently spatially filtered to give u_x - and u_y -field fringe patterns for the deformation that occurred between the two exposures.

In this paper, we show how the high resolution moire technique can be extended to measure with microsecond time resolution both in-plane components of a dynamic displacement field. Three basic modifications have been made:

(1) The lens and mask have been chosen to operate at a magnification of 1:1, with a tuned frequency of 150 $i \cdot \text{mm}^{-1}$ in both the specimen and image planes. This results in a superior sensitivity, with one moire fringe now representing a specimen displacement of 6.7 μm . The reduced field of view (~20 mm \times 20 mm, compared with upwards of 1 m \times 1 m) is more appropriate for visualizing stress waves on the microsecond timescale.

(2) Real-time moire fringes are formed by imaging the specimen grating onto a reference grating; the high speed camera records the fringes rather than the grating. This is necessary because of the low spatial resolution of most high speed cameras, ranging typically from 30 $i \cdot \text{mm}^{-1}$ (rotating mirror) down to only 10 $i \cdot \text{mm}^{-1}$ (image converter).

Paper 2646 received Nov. 4, 1988, revised manuscript received April 24, 1989, accepted for publication April 24, 1989.
© 1989 Society of Photo-Optical Instrumentation Engineers



Fig. 1. Slotted mask used to tune objective lens OL_1 (see Fig. 2) to the spatial frequency of the specimen grating.

(3) The high speed photographs are subsequently processed automatically by computer. Although the fringe patterns reveal immediate qualitative information, more detailed analysis is required to map out the strain field. This is time consuming to carry out manually, particularly since one experiment will generate a sequence of typically 10 to 100 photographs. If crossed gratings (i.e., two sets of lines at 90°) are used both on the specimen and for the reference grating, the Fourier transform method used here allows both in-plane displacement components to be extracted from a single fringe pattern.

2. LENS MODIFICATION

An Olympus 80 mm f/4 macro lens was found to offer good field coverage at 150 l/mm^{-1} . The Olympus is designed to operate at f/1 magnification and is therefore more suitable for these experiments than is the 55 mm f/2 Super Takumar used by Burch and Forno.¹

The mask, shown in Fig. 1, has geometry identical to that described in Refs. 1 through 3; the theory of its operation is also described fully in those references and will not be repeated here. The dimension ξ_0 is related to the tuned frequency u_0 by

$$u_0 = \frac{\xi_0}{RA_0} \quad (1)$$

where R is the distance from the exit pupil to the image plane and A_0 is the center wavelength of the polychromatic illumination. In these experiments, the flash light source was filtered to the range 470 to 520 nm so that $\lambda_0 \approx 490 \text{ nm}$. Taking into account the magnification due to the rear elements of the lens, the value of ξ_0 corresponding to $u_0 = 150 \text{ l/mm}^{-1}$ is 8.2 mm. The mask was machined out of thin brass sheet and sprayed matt black. To obtain access to the iris diaphragm, the slotted ring at the front of the lens is unscrewed. This frees the aperture control sleeve, revealing two more retaining rings. Unscrewing the outer of these rings releases the front elements of the lens as a single unit. The diaphragm, which is also a single assembly held in place by three screws, can then be removed and replaced with the mask.

3. FORMATION OF REAL-TIME MOIRE FRINGES

The optical arrangement used to record the moire fringe patterns is shown in Fig. 2. Although the photographs were taken by transmitted light, the technique is equally applicable to opaque specimens photographed by reflected light.



Fig. 2. Experimental arrangement for high resolution moire photography. X—xenon flash lamp; F—Kodak Wratten filter No. 44; FL_1, FL_2 —field lenses; SG—specimen grating; RG—reference grating; OL_1 —high quality objective lens with masked aperture; OL_2/HSC —recording camera with lens.



Fig. 3. Optical arrangement for doubling the effective spatial frequency of the reference grating. Beam A is the path followed by light from a point source PS in the xenon flash. B, C, and D are the diffracted beams referred to in the text. Other symbols are identified in the caption to Fig. 2.

OL_1 , the masked objective, images the specimen grating SG (in image plane 1) onto the reference grating RG (image plane 2). A second objective, OL_2 , images RG onto image plane 3, which is either the film plane of a 35 mm camera, for quasi-static applications, or the photocathode of an image converter camera when recording dynamic events. The camera used for these studies was a Hadland Imacon 790.

Field lens FL_1 images the xenon flash lamp, X (Thor EAS) onto the mask in OL_1 . After triggering, the electrical power dissipated by the flash is of the order of $1 \text{ J} \cdot \mu\text{s}^{-1}$. Provided the magnification is high enough, the image of A covers all four slots and the lighting is essentially incoherent. FL_2 images the mask onto the iris plane of OL_2 .

In preliminary experiments, the spatial frequencies of SG and RG were both chosen to be 150 l/mm^{-1} . SG is imaged onto RG at a magnification of approximately 1:1, so the formation of moire fringes can be regarded as the usual geometric superimposition of two gratings of almost the same spatial frequency. In practice, however, the fringe contrast is not particularly high. It was found that the contrast could be improved considerably by halving the spatial frequency of the reference grating (i.e., by replacing RG with a 75 l/mm^{-1} grating) and stopping down OL_2 to block the image of the mask. A simple 1-D analysis of this situation is illustrated in Fig. 3. Consider a monochromatic point source PS (wavelength λ_0) situated within the extended flash light source such that its image (beam A) falls within the upper slot of OL_1 . From Eq. (1), it is clear that one of the first-order diffraction peaks from SG (beam B, shown as a dashed line) passes through the lower slot. Beams A and B pass through RG, but the direct beams are blocked by the iris diaphragm of OL_2 , and only the first-order diffracted beams are transmitted. The image is formed from the -1 diffracted beam from A and from the $+1$ diffracted beam from B (denoted C and D, respectively).

The amplitude transmission functions of the specimen and reference gratings, $f_s(y)$ and $f_r(y)$, are assumed to take the form

$$f_s(y) = \frac{1 + d_s \cos 2\pi v_s y}{2} \quad (2)$$

$$f_r(y) = \frac{1 + d_r \cos 2\pi v_r y}{2}$$

where d_s, d_r are proportional to the first-order amplitude diffraction efficiencies ($0 \leq d_s, d_r \leq 1$), and v_s, v_r are the spatial frequencies of the specimen and reference gratings, respectively. If it is assumed that the lenses are thin and free of aberrations, the amplitude distribution of beams A, B, C, and D in image planes 2 and 3 can be written as

$$\begin{aligned} a_A(y) &= g(y), \\ a_B(y) &= \frac{d_s g(y) \exp(-2\pi v_s y)}{2}, \\ a_C(y) &= \frac{d_r g(y) \exp(-2\pi v_r y)}{2}, \\ a_D(y) &= \frac{d_s d_r g(y) \exp[2\pi(v_r - v_s)y]}{4}. \end{aligned} \quad (3)$$

where $g(y)$ is a complex function, with a modulus of unity, to allow for the fact that the source is off axis and the light is not collimated in the image planes; g is the same in image planes 2 and 3, provided the system is focused correctly. The intensity distribution in the film plane is given by

$$\begin{aligned} I(y) &= |a_C + a_D|^2 \\ &= \frac{d_r^2}{4} \left\{ 1 + \frac{d_s^2}{4} + d_s \cos[2\pi(2v_r - v_s)y] \right\} \end{aligned} \quad (4)$$

The final recorded intensity distribution is obtained by integrating Eq. (4) over all of the point emitters within the extended source and over the range of wavelengths transmitted by the filter. The form of Eq. (4) is independent of the position of the point source. At wavelengths differing from λ_0 , there will be some sources for which beam A passes through the upper slot but for which beam B is blocked by the mask. Equation (4) therefore describes the recorded image, although the fringes will have reduced contrast if the spectrum of the light source is too wide. The important points are (1) that a moire fringe pattern is formed in which the effective spatial frequency of the reference grating is twice the actual value and (2) that the fringe contrast is not constrained by the diffraction efficiency of the reference grating.

The specimen and reference gratings were created by exposing film to a two-beam interference pattern from a He-Ne laser. The emulsion used was Agfa 10F75; the reference grating on a glass plate and the specimen gratings on 100 μm thick polyester film. Conventional stripping film (Agfa Litex 0821S, for example) has a coarse grain structure compared with holographic emulsions and was found to be unsuitable for the high frequency gratings required here. The

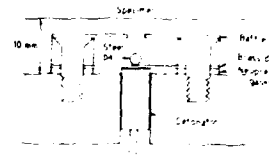


Fig. 4. Cross section through explosive gun used to fire steel ball at specimen.

gratings were bonded to the specimens, emulsion side to air, with cyanoacrylate adhesive.

4. DYNAMIC STRESS FIELD DUE TO SOLID PARTICLE IMPACT

High velocity impact occurs in a number of practical situations, with usually undesirable consequences. Two examples are the damage caused to an aircraft flying through rain and the internal erosion of gas pipelines by sand particles. Dynamic effects can exert a significant influence on the material's response; in the case of liquid drop impact on a brittle material, most of the damage results from the extension of surface flaws by the Rayleigh surface wave.⁴ Experiments have been carried out to measure the transient response of a solid to high speed solid particle impact. Results are presented here as an illustration of the modified high resolution movie technique.

Specimens were machined out of 6 mm thick sheets of cast polymethyl methacrylate (PMMA, ICI 'Perspex') to form rectangular plates with dimensions 70 mm \times 40 mm \times 6 mm. A grating was attached to one face of each plate, as described in the previous section. The projectile (2 mm diameter steel ball) was fired by means of a small detonator (ICI fast acting fuse) in contact with a brass disk to hit the center of one of the long edges of the plate (see Fig. 4). A 5 kV pulse was applied to the detonator, followed 40 μs and 72 μs later by trigger pulses to the flash and camera. With a 0.61 mm thick brass disk, the ball speed was $115 \pm 10 \text{ m s}^{-1}$ with an impact time reproducible to $\pm 3 \mu\text{s}$. The baffle shown in Fig. 4 is another brass disk with a hole for the ball to pass through; this attenuates the air shock, which can otherwise slightly shift the position of the moire fringes. A neoprene gasket was used to prevent the gaseous reaction products from escaping near the sample for the same reason.

The apparatus shown in Fig. 2 was aligned using an unexpanded laser beam, with the expected impact site lying on the optic axis; this minimized the broadening of the sample edge on the photographs. Prior to the recording of a photographic sequence, the position of OL_1 was adjusted to produce linear mismatch fringes. These fringes are equivalent to an initial fictitious strain, either compressive or tensile depending on whether SG is imaged onto RG at a magnification of less than or greater than unity. For each event, two sequences were recorded: one beforehand, showing the undeformed mismatch fringes, and the second during impact. Each sequence consists of eight frames, separated by 0.95 μs . Three examples of fringe patterns recorded during an event are shown in Figs. 5 through 7. The film used was Kodak T-Max 400, push processed to an effective speed of 3200 ASA. For Figs. 5 and 6, a single grating was attached to the specimen, with the lines

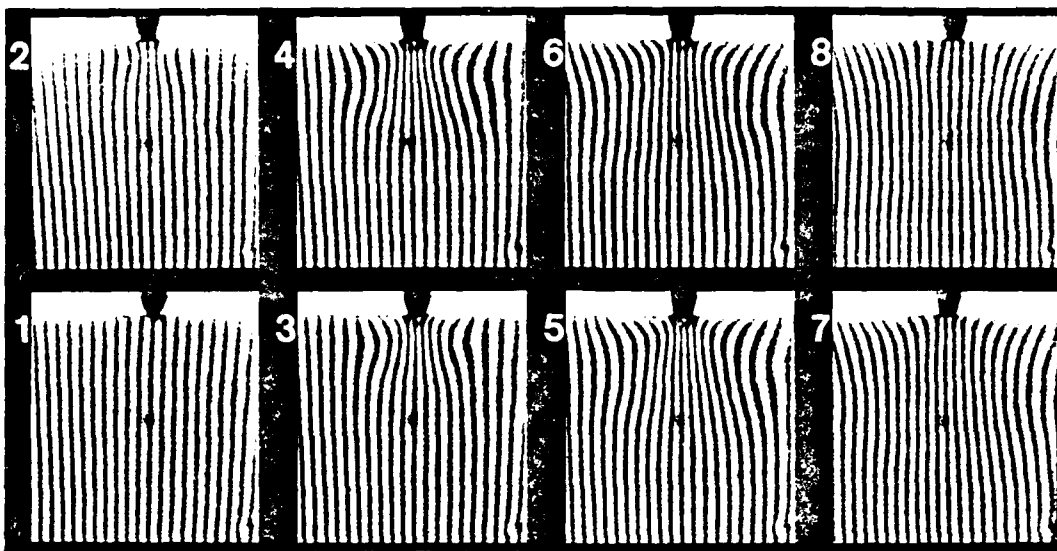


Fig. 5. Ball impact on PMMA: u_x -field fringes. Impact velocity = $115 \text{ m} \cdot \text{s}^{-1}$, interframe time = $0.95 \mu\text{s}$, specimen grating frequency = $150 \text{ f} \cdot \text{mm}^{-1}$, field of view = $16 \times 16 \text{ mm}^2$. Note that the spot at the center of each frame in the Imacon sequences is an artifact due to ion damage of the photocathode.

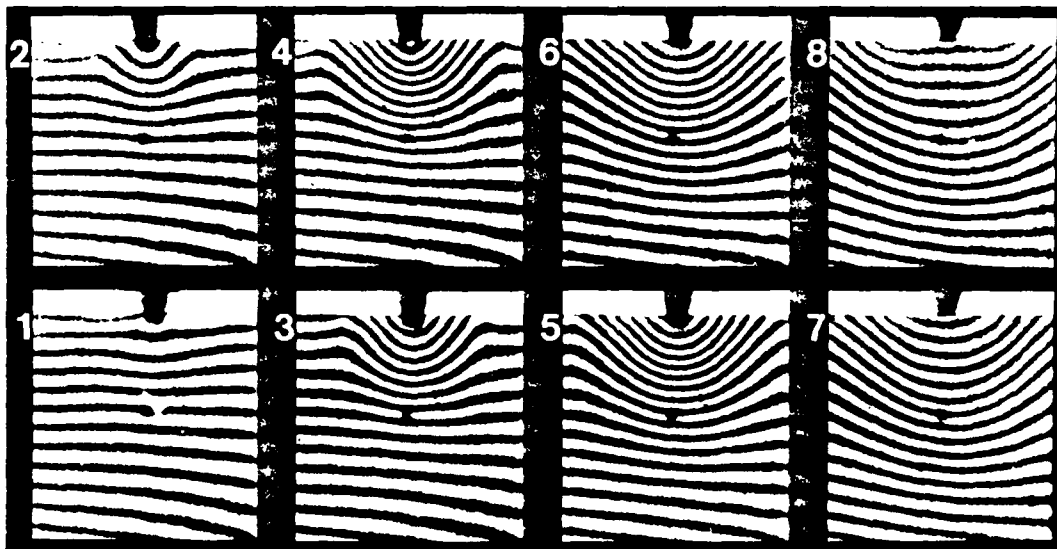


Fig. 6. Ball impact on PMMA: u_y -field fringes. Experimental details are as for Fig. 5.

perpendicular and parallel to the edge, respectively. These two sequences therefore represent the time variation of the x and y displacement components (u_x and u_y). A crossed grating was used in the case of Fig. 7. Although the fringe contrast is

somewhat reduced, both u_x and u_y have been recorded simultaneously, which is a considerable advantage when the event is not reproducible. The mismatch fringes in Fig. 5 are tensile; those in Figs. 6 and 7 are compressive.

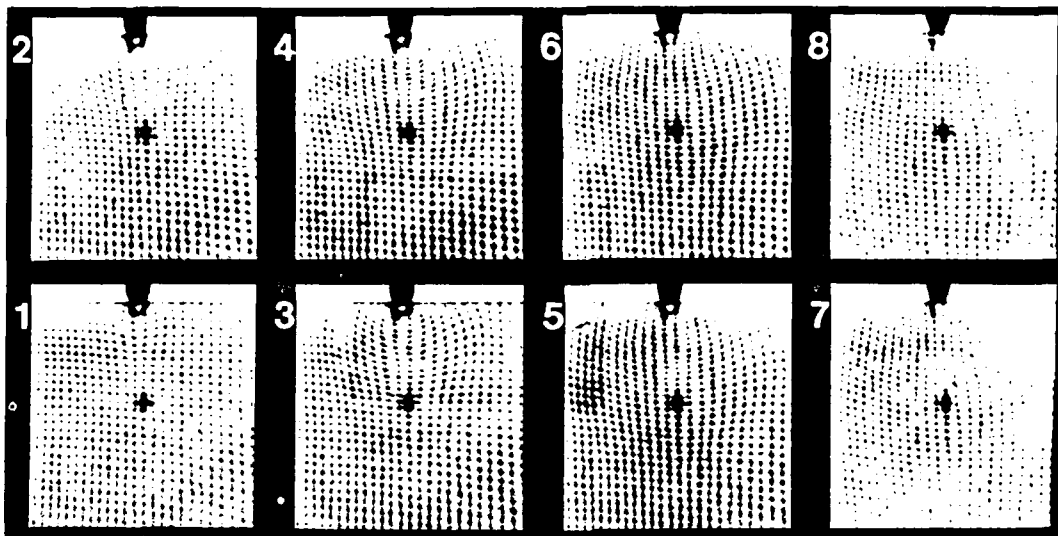


Fig. 7. Ball impact on PMMA: combined u_x - and u_y -field fringes. Experimental details are as for Fig. 5.

5. AUTOMATIC FRINGE ANALYSIS

Useful quantitative information can be easily obtained from Figs. 5 through 7. For example, the strain at a few points can be calculated by measuring the local fringe spacing; bunching of the fringes indicates tension in Fig. 5 and compression in Figs. 6 and 7. Some form of computer analysis is desirable, however, to maximize the amount of information extracted. The method adopted here is based on a 2-D version of the Takeda Fourier transform method.^{1,6}

A fringe pattern has the general intensity distribution

$$\begin{aligned} I(x,y) &= a(x,y) + b(x,y)\cos\Phi(x,y) \\ &= a(x,y) + \frac{b(x,y)}{2} [\exp[i\Phi(x,y)] + \exp[-i\Phi(x,y)]], \end{aligned} \quad (5)$$

where a and b represent the variation of background intensity and fringe contrast, respectively. In moire photography, the phase $\Phi(x,y)$ is related to the relevant displacement component $u(x,y)$ by

$$u(x,y) = p_c \frac{\Phi(x,y)}{2\pi}, \quad (6)$$

where p_c is the pitch of the specimen grating. In general, $a(x,y)$ and $b(x,y)$ will be unknown, so Φ cannot be obtained directly from Eq. (5) by a simple inverse cosine operation. However, provided carrier fringes are present, the three terms on the right-hand side of Eq. (5) can be separated by filtering in the 2-D Fourier transform plane of $I(x,y)$.⁶ For example, if the middle term is selected, then the modified (complex) intensity distribution becomes

$$I'(x,y) = \frac{b(x,y)}{2} \exp[i\Phi(x,y)] \quad (7)$$

and $\Phi(x,y)$ is readily calculated as

$$\Phi(x,y) = \tan^{-1} \frac{\text{Im}[I'(x,y)]}{\text{Re}[I'(x,y)]}, \quad (8)$$

where Re and Im denote real and imaginary parts of a complex number. The phase values given by Eq. (8) are all wrapped onto the range $-\pi$ to π because of the inverse tangent operation and must be unwrapped before $u(x,y)$ can be calculated by Eq. (6).

The practical implementation of this technique is straightforward. The two sets of eight frames, recorded before and during the event, are digitized directly from the film. The image resolution used in these experiments was 256 × 256 pixels. Denoting the digitized intensity distribution of a given image by $I(m,n)$, $m, n = 0, 1, \dots, 255$, a window $W(m,n)$ is applied to the data:

$$I_j(m,n) = W(m,n)I(m,n). \quad (9)$$

A rectangular window was used for the present analysis:

$$W(m,n) = \begin{cases} 1, & m_1 \leq m \leq m_2, n_1 \leq n \leq n_2, \\ 0, & \text{otherwise.} \end{cases} \quad (10)$$

where the borders m_1 , m_2 , n_1 , and n_2 are chosen according to the region of the image containing the fringes. An alternative is the Hamming window; this reduces leakage from the dc peak in the frequency domain but reduces the signal-to-noise ratio of the phase maps near the borders in the spatial domain. The leakage problem with rectangular windows can be reduced substantially by subtracting the dc level of the image

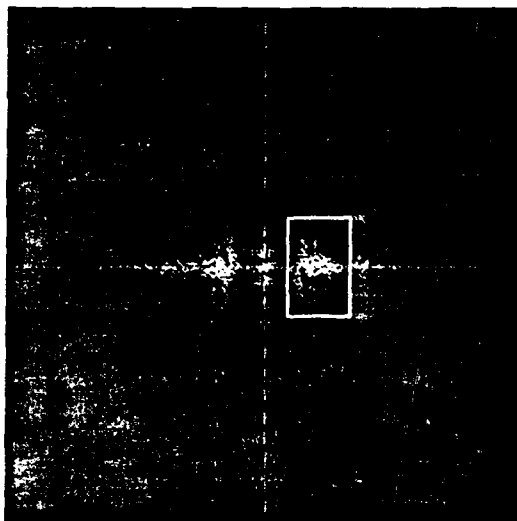


Fig. 8. Real part of the 2-D Fourier transform of frame 5, Fig. 5. The bandpass filter is indicated by the rectangular box.

$$I_2(m, n) = \begin{cases} \frac{\sum_{m=m_1}^{m_2} \sum_{n=n_1}^{n_2} I_1(m, n)}{(m_2 - m_1 + 1)(n_2 - n_1 + 1)}, & m_1 \leq m \leq m_2, n_1 \leq n \leq n_2, \\ I_1(m, n), & \text{otherwise} \end{cases} \quad (1)$$

The 2-D discrete Fourier transform of $I_2(m, n)$ is then calculated. As an example, Fig. 8 shows the real part of the transform of frame 5, Fig. 5. The peak corresponding to the $\exp[i\Phi(x, y)]$ term of Eq. (5) is isolated: in the case of the example shown in Fig. 8, only the Fourier coefficients inside the box are retained, with the remainder set to zero. After inverse transformation, the phase at each pixel is calculated according to Eq. (8). Unwrapping is achieved by working along each row in turn; when the magnitude of the phase change between adjacent data points is greater than π , 2π is either added to or subtracted from the remaining data points in the row, depending on the sign of the change. The process is then repeated but working by columns rather than by rows. This phase unwrapping method worked well on the fringe patterns shown in Figs. 5 and 6. With poor quality fringes, however, unwrapping along the central column may produce better results because the signal-to-noise ratio tends to be higher at the center of the phase map than at the edges.

Figure 9 shows the u_x component of the displacement field calculated from frame 5 of Fig. 5. This map still contains the fictitious displacement field corresponding to the carrier fringes. In Ref. 5, the carrier fringes were removed by introducing a shift in the Fourier domain before inverse transformation. However, a residual fictitious displacement field will be present unless the carrier fringes were initially parallel, with an integral number of fringes across the field of

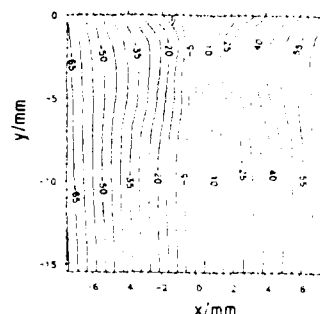


Fig. 9. Contour map of u_x resulting from the analysis of frame 5, Fig. 5, by the Fourier transform method. Contour interval = $5.0 \mu\text{m}$.

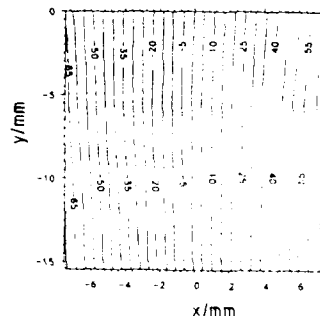


Fig. 10. Contour map of u_x before deformation. The initial (fictitious) strain is due to the tension mismatch fringes. Contour interval = $5.0 \mu\text{m}$.

view. Alternatively, the linear phase distribution corresponding to the carrier frequency can be subtracted from the recovered phase.⁶ This was essentially the approach adopted in the present analysis, but instead of assuming a linear phase distribution, we obtained the true distribution by analyzing a fringe pattern recorded before the deformation (see Fig. 10). The difference between Figs. 9 and 10 (Fig. 11) therefore shows $u_x(x, y)$ caused by the impact alone. With this approach, the carrier fringes do not need to be parallel or of uniform spacing. Furthermore, errors due to image distortion are eliminated because a given specimen coordinate is represented by the same pixel position in both phase maps. Field distortion in this application is due primarily to the electron optics in the image converter camera. As a result, the distortion will vary between frames, and it is therefore advisable to calculate the initial phase distribution for each frame individually. Thus, analysis of an event lasting for eight frames involves application of the Fourier transform method to 16 images. Once the appropriate filter has been established by examining the Fourier transform of one of the images, all 16 are processed automatically by the computer. Figure 12 shows the results from the analysis of the eight frames of Fig. 5.

The same procedure can be followed in the case of the crossed fringe patterns (Fig. 7). The real part of the Fourier

transform of frame 4 is shown in Fig. 13. The transform now consists of four peaks due to the fringes, together with the dc peak. The four fringe peaks are isolated from one another, provided the spatial frequency of the carrier is sufficiently high; the u_x and u_y fringe information can then be separated by choosing the appropriate peak before inverse transformation. If the Fourier components outside box 1 of Fig. 13 are set to zero, then the resulting phase map represents u_x . In the same way, isolation of peak 2 results in a phase map proportional to u_y . Figures 14 and 15 show $u_x(x,y)$ and $u_y(x,y)$, respectively, from frame 4 of Fig. 7 after subtraction of the undeformed displacement field. The reduced contrast of the original fringe pattern meant that a phase unwrapping routine with greater noise immunity than the one described earlier

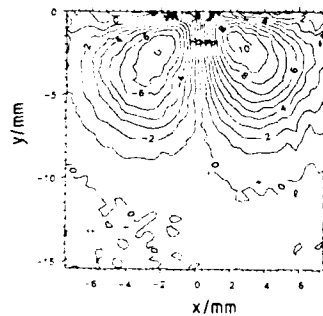


Fig. 11. Contour map of u_x as for Fig. 9 but after subtraction of the initial displacement field (Fig. 10). Contour interval = $1.0 \mu\text{m}$.

was required to produce Figs. 14 and 15. Details of the algorithm are presented in Ref. 8.

6. CONCLUSIONS

It has been shown that the technique of high resolution moire photography can be adapted to form high contrast real-time

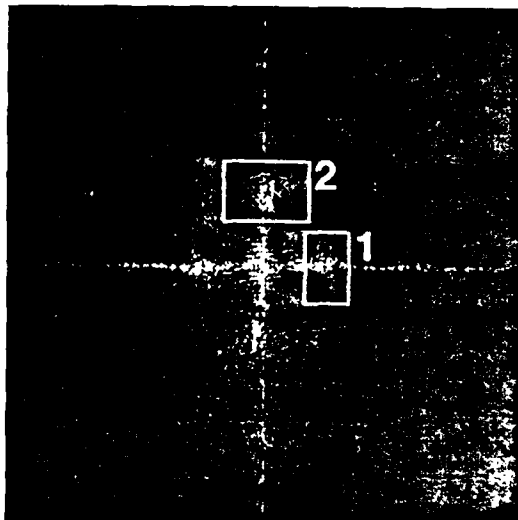


Fig. 13. Real part of the 2-D Fourier transform of frame 4, Fig. 7. Bandpass filters 1 and 2 separate the u_x - and u_y -field fringe patterns

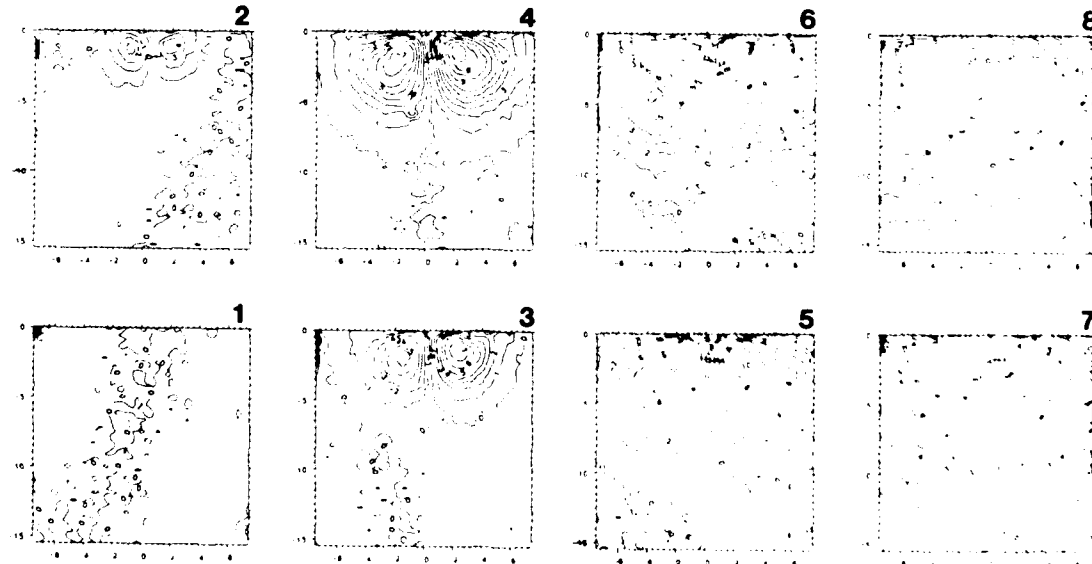


Fig. 12. Contour maps of u_x calculated from the eight frames of Fig. 5. Frame 5 is as shown in Fig. 11. Contour interval = $1.0 \mu\text{m}$.

HIGH RESOLUTION MOIRE PHOTOGRAPHY APPLICATION TO DYNAMIC STRESS ANALYSIS

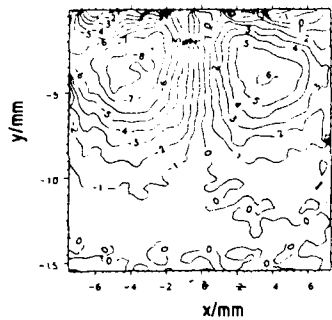


Fig. 14. Contour map of u_x calculated from frame 4 of Fig. 7. Contour interval = $1.0 \mu\text{m}$.

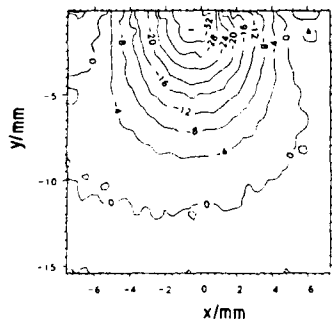


Fig. 15. Contour map of u_y calculated from frame 4 of Fig. 7. Contour interval = $4.0 \mu\text{m}$.

moire fringes and that these can be used to measure deformation with microsecond time resolution. The sensitivity of the technique (spatial frequency of specimen grating = $150 \text{ f} \cdot \text{mm}^{-1}$) lies usefully between conventional moire (typically under $40 \text{ f} \cdot \text{mm}^{-1}$) and moire interferometry ($1000 \text{ f} \cdot \text{mm}^{-1}$ or more). The main advantage over moire interferometry is the simplicity of the experimental arrangement. The light source is a flash lamp rather than high powered laser.

The Fourier transform method of fringe analysis has been used to extract automatically the displacement information from a fringe pattern. It was found to be reliable and capable of processing an entire high speed sequence with no manual intervention. It was shown how the method could be extended

to the case of two fringe patterns superimposed on the same image. This was applied to fringe patterns resulting from the use of crossed specimen and reference gratings and allowed both in-plane displacement components to be measured simultaneously.

7. ACKNOWLEDGMENTS

The authors wish to acknowledge contributions from N. Wilson and M. F. Turner at the early stages of this work. The explosive gun used to fire the steel balls was based on a design by M. M. Chaudhri. One of us (J. M. H.) is grateful to Gonville and Caius College, Cambridge, and to the Science and Engineering Research Council for support in the form of research fellowships.

8. REFERENCES

1. J. M. Burch and C. Forno, "High sensitivity moire grid technique for studying deformation in large objects," Opt. Eng. 14(2), 178-185 (1975)
2. J. M. Burch and C. Forno, "High resolution moire photography," Opt. Eng. 21(4), 602-614 (1982)
3. C. Forno, "Deformation measurement using high resolution moire photography," Opt. Lasers Eng. 8, 189-212 (1988)
4. S. Van der Zwaag and J. F. Field, "Rain erosion damage in brittle materials," Eng. Fract. Mech. 17(4), 367 (1983)
5. M. Iakeda, H. Ina, and S. Kobayashi, "Fourier-transform method of fringe-pattern analysis for computer-based topography and interferometry," J. Opt. Soc. Am. 72(1), 156-160 (1982)
6. D. J. Bone, H. A. Bachor, and R. J. Sandeman, "Fringe pattern analysis using a 2-D Fourier transform," Appl. Opt. 25(10), 1653-1660 (1986)
7. W. W. Mack, "Two-dimensional fringe-pattern analysis," Appl. Opt. 22(23), 3898-3901 (1983)
8. J. M. Huntley, "Noise-immune phase unwrapping algorithm," submitted Sept. 1988 to Appl. Opt.

Jonathan M. Huntley received his BA in physics and Ph.D. degrees from the University of Cambridge in 1983 and 1987 respectively. He is currently a research fellow at the Cavendish Laboratory, with research interests that include speckle metrology, moire techniques, high speed photography, and dynamic fracture.



John E. Field has been a member of the Cavendish Laboratory since 1958. He became university demonstrator in 1966 and university lecturer in 1971. His present position is head of the Physics and Chemistry of Solids Section of the laboratory. His research interests include fracture, impact, erosion phenomena, explosive initiation, and high speed photography.



Crack growth in viscoelastic media: effect of specimen size

J. M. Huntley

University of Cambridge, Cavendish Laboratory,
Madingley Road, Cambridge CB3 0HE, UK

Abstract

The strain energy release rate G required to propagate a crack at velocity V along an infinite viscoelastic strip of width $2h$ is calculated numerically. It is shown that G can be approximated by $2\gamma C(h/V)/C(l/V)$, where γ is the intrinsic fracture energy, $C(t)$ is the creep compliance function, and l is the Barenblatt or Dugdale zone length. The analysis predicts a region of the G - V curve having negative gradient, providing a possible explanation for the instability phenomena observed in the fracture of polymers. The critical point (G_c, V_c) at which $dG/dV = 0$, is dependent on specimen size, with large specimens having greater apparent fracture surface energy than small ones. When applied to polymethyl methacrylate (PMMA), the predicted value of V_c is in close agreement with the velocity observed at the transition from slow to fast crack growth.

1. Introduction

Numerous experiments have been carried out over the past four decades to investigate the kinetics of crack propagation in viscoelastic media (see, for example, Greensmith and Thomas 1955; Mueller and Knauss 1971a; Gent and Schultz 1972; Andrews and Kinloch 1973; Maugis and Barquins 1978). When $G \leq 2\gamma$ (G being the strain energy release rate, γ the intrinsic fracture energy), no crack growth is observed, as would be expected from the Griffith criterion $G = 2\gamma$ for an equilibrium crack. However, when $G > 2\gamma$, slow stable crack growth can occur, with viscoelastic losses absorbing the surplus energy $G - 2\gamma$. For a given crack speed, the energy dissipated per unit length of crack advance is found to be proportional to 2γ , as demonstrated by peeling experiments in a range of liquids (Gent and Shultz 1972) or on various substrates (Andrews and Kinloch 1973). The basic equation governing crack propagation in viscoelastic media can therefore be written as (Maugis and Barquins 1978):

$$G - 2\gamma = 2\gamma\phi(a_T V) \quad (1)$$

where ϕ is a non-dimensional loss function, V is the crack speed, and a_T is the Williams Landel Ferry shift factor to take account of measurements made at different temperatures. Equation (1) applies to both adhesive and cohesive modes of failure. γ is defined as the intrinsic fracture energy, i.e. the energy needed to create unit area of new surface in the absence of viscoelastic dissipation in the bulk material. For adhesive failure, γ is the true (rate-independent) thermodynamic surface energy required to overcome the van der Waals and electrostatic forces between substrate and elastomer. For cohesive failure, γ includes the energy expended irreversibly in breaking or pulling out the molecular chains to create unit area of new surface. Rate-independence of γ may also hold in the latter case, as suggested by experiments on polyurethane in which internal friction was reduced by swelling (Mueller and Knauss 1971a); however, equation (1) would still be expected to apply to situations where γ is rate-dependent.

Maugis and Barquins (1978) studied the adherence of polyurethane on glass with a range of geometries and showed that equation (1) was satisfied over 6 decades of crack velocity; the viscoelastic dissipation function $\phi(a_T V)$ was found to be independent of specimen geometry and loading system, and therefore appeared to be a material property. The observed variation of G with V is shown schematically in figure 1 as the region $V < V_c$. Maugis has recently argued (1985) that at high crack speeds, the material behaviour will tend to become elastic so $\phi(a_T V)$ will decrease with V (figure 1, region $V_c < V < V_1$). At the critical point (G_c, V_c) , $dG/dV = d\phi/dV = 0$ and the system becomes unstable: if the crack accelerates, the resistance to propagation decreases so the crack accelerates further. However, dG/dV cannot be negative for all velocities greater than V_c . There may be further regions of positive gradient due to a complicated

loss spectrum, but in any case the crack cannot travel faster than the Rayleigh wave speed, c_R . At speeds approaching c_R , the surplus energy $G - 2\gamma$ is converted into kinetic energy, and dG/dV becomes positive again in the range $V_1 < V < c_R$. From velocity V_c , a crack will therefore accelerate to velocity V_2 (close to c_R) which may in practice be several orders of magnitude higher than V_c . The criterion $G = G_c$ for the onset of catastrophic failure is therefore not the Griffith criterion, but one of crack speed discontinuity resulting from the viscoelastic loss function $\phi(a_T V)$.

Several attempts have been made to calculate the variation of G with V (Mueller and Knauss 1971b; Schapery 1975a; Greenwood and Johnson 1981; Christensen and Wu 1981; Huntley 1987; de Gennes 1988). Generally, these predicted that G would increase monotonically with V , so the important region of negative slope was not explained. However, two relatively simple analyses presented recently (Huntley 1987; de Gennes 1988) do predict such a region at high crack speeds, provided the size of the specimen is taken into account. The present paper develops further the ideas from Huntley (1987).

2. Strain energy release rate

The problem considered here is a semi-infinite mode I crack growing in an infinite strip of width $2h$ (see figure 2). A coordinate system (x,y) and tractions $T = T_i(x)$ ($i = x,y$) acting on the edges of the strip move with the crack tip at speed V . Time is allowed for the system to reach steady-state conditions, so that the stress, strain and displacement distributions in the strip, $\sigma_{ij}(x,y)$, $\epsilon_{ij}(x,y)$ and $u = u_i(x,y)$ are time-invariant in the moving coordinate system. It is assumed that $T \rightarrow 0$ as $|x| \rightarrow \infty$, and that inertial effects can be neglected. No restrictions are imposed at this stage on the stress-strain relation for the material in the strip.

The strain energy release rate, G , is defined by

$$G = -d(-U_w + U_e)/da \quad (2)$$

where U_w is the mechanical work done by the edge tractions T , U_e is the elastic strain energy of the system, and a is the crack length. To calculate G for the strip problem, we consider a virtual crack extension of δa through the following three steps:

Step 1 Change edge tractions $T(x)$ to $T(x - \delta a)$ by superposing $\delta T(x) = -(dT/dx)\delta a$. Edge tractions move through $\delta u^{(1)}(x,h)$.

Step 2 Cut material from $(0,0)$ to $(\delta a,0)$, applying tractions to new surface to keep $u(x,0) = 0$, $x > 0$. Reduce new surface tractions to zero. Wait for time $\delta t = \delta a/V$. At point x , $T(x - \delta a)$ moves through $\delta u^{(2)}(x,h)$.

Step 3 Move coordinate system by δa so origin is at new crack tip position.

After steps 1,2 and 3, the crack, edge tractions, and stress, strain and displacement distributions have moved by δa in the $+x$ direction. The total change in elastic energy, δU_e , is zero because of the assumption that $T \rightarrow 0$ as $|x| \rightarrow \infty$. The total work done by the edge tractions is

$$\delta U_w = \delta U_w^{(1)} + \delta U_w^{(2)} \quad (3)$$

where the superscripts 1 and 2 refer to steps 1 and 2. From the symmetry of the problem, the total work done is twice that done on the upper edge. Neglecting terms above first order in δa results in

$$\delta U_w^{(1)} = 2 \int_{-\infty}^{\infty} T(x) \cdot \delta u^{(1)}(x,h) dx \quad (4)$$

$$\delta U_w^{(2)} \approx 2 \int_{-\infty}^{\infty} T(x) \cdot \delta u^{(2)}(x, h) dx \quad (5)$$

Therefore

$$\delta U_w \approx 2 \int_{-\infty}^{\infty} T(x) \cdot \delta u(x, h) dx \quad (6)$$

where

$$\begin{aligned} \delta u &= \delta u^{(1)} + \delta u^{(2)} \\ &= u(x - \delta a, h) - u(x, h) \\ &\approx -(\partial u / \partial x) \cdot \delta a \end{aligned} \quad (7)$$

In the limit $\delta a \rightarrow 0$, it follows from equations (2), (6) and (7) that

$$G = -2 \int_{-\infty}^{\infty} T(x) \cdot [\partial u(x, h) / \partial x] dx \quad (8)$$

For an elastic material, this result could have been established by simple application of the Rice J-integral (Rice 1968). It is clear from the above derivation, however, that equation (8) is generally true, independent of the material's constitutive equations. In §5, it will be used to calculate G for crack growth in a viscoelastic strip.

3. Elastic stress and displacement fields

Before progressing to viscoelastic materials, it is useful to consider briefly the case of an elastic strip. Let the edge tractions be chosen such that just the singular term in the stress field expansion is present. The stress and displacement fields are therefore given by (see, for example, Lawn and Wilshaw 1975):

$$\sigma_{ij}^e(x, y) = K_I f_{ij}(\theta) / (2\pi r)^{1/2} \quad (9)$$

$$u_i^e(x, y) = K_I (1 + v) g_i(\theta) r^{1/2} / (8\pi)^{1/2} E \quad (10)$$

where

$$r = (x^2 + y^2)^{1/2}$$

$$\theta = \tan^{-1}(y/x)$$

$$f_{xx}(\theta) = \cos(\theta/2)[1 - \sin(\theta/2)\sin(3\theta/2)]$$

$$f_{yy}(\theta) = \cos(\theta/2)[1 + \sin(\theta/2)\sin(3\theta/2)]$$

$$f_{xy}(\theta) = \sin(\theta/2)\cos(\theta/2)\cos(3\theta/2)$$

$$g_x(\theta) = [(2\kappa - 1)\cos(\theta/2) - \cos(3\theta/2)]$$

$$g_y(\theta) = [(2\kappa + 1)\sin(\theta/2) - \sin(3\theta/2)]$$

$$\kappa = (3 - \nu)/(1 + \nu) \quad (\text{plane stress})$$

$$= (3 - 4\nu) \quad (\text{plane strain}) \quad (11)$$

E and ν represent Young's modulus and Poisson's ratio, respectively, and the superscript e denotes an elastic field. The required edge tractions are:

$$\begin{aligned} T_x(x) &= \sigma_{xy}^e(x, h) \\ T_y(x) &= \sigma_{yy}^e(x, h) \quad (\text{upper edge}) \\ T_x(x) &= -\sigma_{xy}^e(x, -h) \\ T_y(x) &= -\sigma_{yy}^e(x, -h) \quad (\text{lower edge}) \end{aligned} \quad (12)$$

The integral in equation (8) can be readily evaluated with the above stress and displacement distributions to give the usual result

$$\begin{aligned} G &= K_I^2/E \quad (\text{plane stress}) \\ &= K_I^2(1 - \nu^2)/E \quad (\text{plane strain}) \end{aligned} \quad (13)$$

4. Viscoelastic stress and strain fields

For the problem under consideration, the creep formulation (imposed stresses) is more suitable than the relaxation approach (imposed strains). A small change in stress $\delta\sigma_{xx}$ at time $t = 0$ results in a change in strain $\delta\varepsilon_{xx} = C(t)\delta\sigma_{xx}$ at time t , where $C(t)$ is the creep compliance. In linear viscoelasticity theory, the total strain is then given by the superposition principle as a convolution integral. The expression for ε_{xx} , for example, is

$$\varepsilon_{xx}(t) = \int_{-\infty}^t C(t-t')(\partial\sigma_{xx}/\partial t')dt' - \int_{-\infty}^t R(t-t')[d(\sigma_{yy} + \sigma_{zz})/\partial t']dt' \quad (14)$$

where the compliance function $R(t)$ takes the place of the elastic compliance ν/E .

For the present problem, where material flows at constant speed through a fixed stress distribution, the loading history at any point (x, y) is determined by $\sigma_u(x', y)$ ($x' \geq x$). Provided $\sigma_u(x, y)$ is known, and $|\sigma_{ij}(x, y)| \rightarrow 0$ as $x \rightarrow \infty$, the viscoelastic strain field can therefore be calculated as follows:

$$\frac{\partial u_x}{\partial x} = \int_{-\infty}^x C[(x'-x)/V](\partial\sigma_{xx}/\partial x')dx' - \int_{-\infty}^x R[(x'-x)/V](\partial\sigma_{yy}/\partial x')dx' \quad (15)$$

$$\frac{\partial u_y}{\partial y} = \int_{-\infty}^x C[(x'-x)/V](\partial\sigma_{yy}/\partial x')dx' - \int_{-\infty}^x R[(x'-x)/V](\partial\sigma_{xx}/\partial x')dx' \quad (16)$$

$$(\frac{\partial u_x}{\partial y} + \frac{\partial u_y}{\partial x}) = 2 \int_{-\infty}^x [C[(x'-x)/V] + R[(x'-x)/V]](\partial\sigma_{xy}/\partial x')dx' \quad (17)$$

where the strains have been expressed directly in terms of displacement gradient, and plane stress conditions have been assumed. Evaluation of G by equation (8) requires both $\frac{\partial u_x}{\partial x}$ and $\frac{\partial u_y}{\partial x}$. The first of these is specified by equation (15). The second can be obtained by differentiating

equation (15) with respect to y , followed by integration with respect to γ ; the resulting expression for $\partial u_x / \partial y$ is then subtracted from equation (17) to give:

$$\begin{aligned} \partial u_y / \partial x = & \int_{-\infty}^x C[(x'-x)/V] [2(\partial \sigma_{xy} / \partial x') - (\partial \sigma_{xx} / \partial y)] dx' \\ & + \int_{-\infty}^x R[(x'-x)/V] [2(\partial \sigma_{xy} / \partial x') + (\partial \sigma_{yy} / \partial y)] dx' \end{aligned} \quad (18)$$

We now consider the particular situation in which the applied tractions $T(x)$ are given by equation (12). The problem then is to deduce the resulting stress distribution so that G can be evaluated by equations (8), (15) and (18). Elastic solutions (such as those given by equations (9)-(11)) can often be generalised to viscoelastic solutions through the classical correspondence principle plus Laplace transform inversion (see, for example, Williams 1980). This method is only applicable when the crack is stationary; moving cracks, however, can be analysed under somewhat restrictive conditions by the extended correspondence principle developed by Graham (1968). The restrictions for the present problem are:

- (a) the crack cannot decrease in size;
- (b) the elastic stress σ_{yy}^e on the upper edge ($y = h$) and on the future crack line ($y = 0, x > 0$) must be independent of E and v ; and
- (c) the elastic displacement u_y^e on the upper edge ($y = h$) and on the crack face ($y = 0, x \leq 0$) must be separable in the form $u_y^e = \xi(E, v) \chi(x)$.

Condition (a) is obviously satisfied; inspection of equations (9)-(11) shows that condition (b) is also satisfied, but that (c) is not, since u_y^e takes the form $u_y^e = \xi(E) \chi(v, x)$ on the upper edge. However, as pointed out by Schapery (1975b), provided v is constant (which is at least approximately true for many polymeric materials), dependence of the elastic solution on Poisson's ratio does not invalidate the extended correspondence principle. Under these conditions, therefore, the Laplace transforms of the elastic and viscoelastic stress fields take the same form, and since the elastic stress field involves no elastic constants, the elastic and viscoelastic stress fields are identical. The same conclusion can be reached by assuming the elastic stress field to hold, and then checking that the strains calculated by equations (15)-(17) obey the compatibility equation, and that $(\partial u_y(x, 0) / \partial x) = 0$ ($x > 0$). These conditions are in fact satisfied even when v is time-dependent, so that the extended correspondence principle is over-restrictive in this particular case. The calculations in the next section will, however, be made with Poisson's ratio taken to be constant.

5. Calculation of G

It is convenient to rewrite equation (8) in terms of the non-dimensional coordinate $\beta = x/h$:

$$G = -2 \int_{-\infty}^{\infty} T \cdot (\partial u / \partial \beta) d\beta \quad (19)$$

The tractions and strains along the line $y = h$ can be expressed as functions of β using equations (9), (11), (12), (15) and (18):

$$T_1 = K_1 p_1(\beta) / (2\pi h)^{1/2} \quad (20)$$

$$\partial u_y / \partial \beta = \left[K_1 h^{1/2} / 8(2\pi)^{1/2} \right] \int_{-\infty}^{\beta} C[(\beta' - \beta)h/V] q_1(\beta') d\beta' \quad (21)$$

where

$$\begin{aligned}
p_x(\beta) &= \sin(\theta/2)\cos(\theta/2)\cos(3\theta/2)/(1+\beta^2)^{1/4} \\
p_y(\beta) &= \cos(\theta/2)[1+\sin(\theta/2)\sin(3\theta/2)]/(1+\beta^2)^{1/4} \\
q_x(\beta) &= [-(1-7v)\cos(3\theta/2)-3(1+v)\cos(7\theta/2)]/(1+\beta^2)^{3/4} \\
q_y(\beta) &= [(11+3v)\sin(3\theta/2)-3(1+v)\sin(7\theta/2)]/(1+\beta^2)^{3/4} \\
\theta &= \tan^{-1}(1/\beta)
\end{aligned} \tag{22}$$

and v is assumed to be constant as discussed in the previous section.

We calculate G first for the case of the standard linear solid shown in figure 3(a). This has the creep function

$$C(t) = (1/E_\infty)[1 - (1 - 1/k)\exp(-t/T)] \tag{23}$$

where the relaxation time $T = \eta/E_\infty$; $k = E_0/E_\infty$; and E_0 and E_∞ are the instantaneous and relaxed modulus, respectively. $C(\beta h/V)$ is plotted in figure 3(b) as a function of β , for different values of (VT/h) . Figure 3(c) shows the functions $q_i(\beta)$: evaluation of $\partial u_i/\partial \beta$ requires convolution of q_i with $C(\beta h/V)$ (equation (22)). It is clear from figure 3(b) that at low crack speeds ($VT/h \rightarrow 0$), the convolution integral reduces to that for an elastic material with modulus E_∞ ; G is therefore given by equation (13) as

$$G = K_I^2/E_\infty \tag{24}$$

As the crack speed increases, the q_i curves become increasingly weighted by the short time portion of the compliance function. The width of $q_i(\beta)$ is of order unity; since the rise-distance of the $VT/h = 1$ curve in figure 3(b) is also of order unity, a significant reduction in $\partial u_i/\partial \beta$, and hence G , will occur as the speed approaches $V = h/T$. At very high speeds ($VT/h \rightarrow \infty$), the response is again elastic, but with modulus E_0 ; G therefore drops to the final value

$$G = K_I^2/E_0 \tag{25}$$

Calculation of G for arbitrary V is difficult to perform analytically with this particular choice of creep function, but the low speed asymptotic form can be established with the approximation

$$\begin{aligned}
C((\beta' - \beta)h/V) &= (1/E_\infty)[1 - (1 - 1/k)(VT/h)\delta(\beta' - \beta)] \\
&\quad [(VT/h) \ll 1]
\end{aligned} \tag{26}$$

where δ is the Dirac delta function. This gives the result

$$\begin{aligned}
G &= (K_I^2/E_\infty)[1 - (2/\pi)(1 + v/2)(1 - 1/k)(VT/h)] \\
&\quad [(VT/h) \ll 1]
\end{aligned} \tag{27}$$

G can in any case be evaluated numerically. Figure 4 shows the variation of non-dimensional strain energy release rate ($E_\infty G/K_I^2$) with non-dimensional crack velocity (VT/h) for three different values of k , and three values of v . The inner and outer integrals (equations (21) and (19), respectively) were carried out by routines from a standard package of numerical algorithms (NAG library subroutines D01AHF and D01AMF). As expected, the low and high speed values of G approach the limits given by equations (24) and (25), with a significant drop in G occurring at $VT/h \approx 1$. The physical meaning behind the behaviour shown in figure 4 is that for a given stress intensity factor, the distance moved by the edge tractions per unit length of crack advance decreases as the crack speed increases, due to the increased stiffness of the material. Figure 4 can in fact be usefully considered as a plot of $(E_\infty C_e)$ versus (VT/h) where

$$C_e = G/K_I^2 \tag{28}$$

is the effective specimen compliance.

6. Calculation of viscoelastic loss function

The main result from the previous section was the variation of G/K_I^2 with crack speed. In order to calculate $G(V)$ (and hence $\phi(V)$, through equation (1)), we therefore require the crack speed dependence of K_I . The form of $K_I(V)$ has been considered theoretically by a number of authors (Schapery 1975a; Greenwood and Johnson 1981); we use here the Greenwood and Johnson analysis of adhesive failure. This models the contact between two viscoelastic surfaces as a Barenblatt crack where energy 2γ is required to overcome the surface attractive forces in the crack tip zone. The shape of the Barenblatt zone is approximated by that of an elastic crack, with modulus given by the reciprocal of the creep compliance at a representative time $t^* = l/V$, where l is the zone length. l therefore varies as $1/C(l/V)$, and so increases monotonically with V . An increased value of l implies a higher stress intensity factor, because the surface forces are active over a greater area. K_I in fact varies as $l^{1/2}$ for an elastic crack, which leads to the approximate result

$$K_I^2 = 2\gamma/C(l/V) \quad (29)$$

The velocity dependence of l is given by

$$(l/V)E_\infty C(l/V) = l_0/V \quad (30)$$

where l_0 is the Barenblatt zone length at zero crack speed. Substitution of the creep function for the three element model (equation (23)) into equation (30) results in

$$(l/VT)[1 - (1 - 1/k)\exp(-l/VT)] = l_0/VT \quad (31)$$

Equation (31) defines (VT/l) as a function of non-dimensional velocity (VT/l_0) ; equation (23) can then be used to calculate $C(l/V)$. Figure 5 shows the variation of K_I^2 with VT/l_0 for three values of k .

From equations (1), (28) and (29), it follows immediately that

$$\begin{aligned} G/2\gamma &= C/l/V \\ &= \phi(V) + 1 \end{aligned} \quad (32)$$

In graphical terms, $G/2\gamma$ is obtained by simply adding the log-log curves in figure 4 to those in figure 5, after shifting along the horizontal axis by $m = h/l_0$ to allow for the different length scales in the two non-dimensional crack velocities. l_0 is typically of the order of atomic dimensions: in polyurethane, for example, $l_0 \approx 5 \times 10^{-12} \text{ m}$ (Greenwood and Johnson 1981). h can easily range from $10^{-6} - 1 \text{ m}$: the lower limit occurs in filled polymers where particles of micron dimensions are separated by adhesive layers of comparable thickness; the upper limit is based on the dimensions of a typical testing machine. Suitable values of m therefore lie between 10^5 and 10^{11} . It should be pointed out that since the maximum zone length is kl_0 , we must have $m \gg k$ (small scale yielding) for the calculation of G in §5 to be valid.

Figure 6 shows the variation of $G/2\gamma$ with crack speed for the particular case $k = 10^3$, $v = 0.0$, and with four different specimen dimensions ($m = 10^5, 10^7, 10^9$ and 10^{11}). It is clear that the region of negative gradient is due solely to the contribution from figure 4, i.e. to the drop in specimen compliance with increasing crack speed. Evaluation of G by equation (24), which defines Maugis and Barquins' "work of adhesion" (Maugis and Barquins 1978), will show no such region: this case corresponds to that of infinite specimen dimensions. The critical point (G_c , V_c) at which $dG/dV = 0$, is size dependent, with both G_c and V_c decreasing as the specimen dimensions are reduced; the effect is particularly significant at low values of m . In the low velocity regime, $G(V)$ is effectively size independent.

Although the problem considered here is highly idealised, it is expected that the main features will be applicable to other situations where the tractions move with the crack, and are of significant magnitude over a length scale comparable to the characteristic dimension of the specimen. It should be emphasized that, unlike the elastic case, G and K_I are not equivalent fracture parameters. K_I increases monotonically with V (figure 5), whereas G has regions of both positive and negative gradient (figure 6). The kinetics of crack growth above V_c may therefore depend on which of the two parameters is imposed directly by the loading system (i.e., which one is independent of specimen modulus). In peeling experiments, for example, the applied force defines G , because movement of the load through unit distance causes unit crack extension; the contact force on a punch, on the other hand is related directly to K_I (Greenwood and Johnson

1981).

7. Approximate analysis

The curves in figure 4 showing $E_\infty G/K_1^2$, or equivalently $E_\infty C_e$ where C_e is the effective specimen compliance (defined by equation (28)), were obtained by means of a double integral involving the creep compliance and stress distribution along the line $y = h$. It is useful at this stage to seek a simple approximate expression for C_e .

As noted earlier, the functions $q_i(\beta)$ (see figure 3(c)) have a width $\Delta\beta$ of order unity. A given value for the ratio (V/h) specifies the creep curve $C(\beta h/V)$ with which the q_i are convolved (see figure 3(b)). We make the approximation that $C(\beta h/V)$ is constant, and takes the value of $C(h/V)$ at the point $\beta = 1$. The problem is now that of an elastic crack with Young's modulus replaced by $1/C(h/V)$, so the double integral for G (equations 19 and 21) can readily be performed to give

$$G = K_1^2 C(h/V) \quad (33)$$

Figure 7 shows G/K_1^2 evaluated according to equation (33) for the three-element model, with three different values of k . The agreement with the results of the exact calculations (figure 4) is quite reasonable in view of the approximation used. Combining equations (29) and (33), we obtain a simple approximate expression for the loss function

$$\begin{aligned} \phi(V) &= (G - 2\gamma)/2\gamma \\ &= [C(h/V)/C(l/V)] - 1 \end{aligned} \quad (34)$$

Figure 8(a) shows how $\phi(V)$ can be visualised from a log-log plot of $C(t)$. The creep function in this case is that of the three element model with $E_0/E_\infty = 10^3$. Points A and B represent times $t = l/V$ and h/V respectively, so the difference between their intercepts on the vertical axis is $\log_{10}(1 + \phi(V))$. A and B move to the left with increasing crack speed: $\phi(V)$ is therefore seen to rise at first, but then to fall again at high V , provided h is finite.

It is instructive to consider in a qualitative way the regions of the specimen in which energy is being dissipated. Viscoelastic losses are often expressed in terms of the loss modulus under cyclic stress or strain loading. The energy dissipated per cycle, W , in the three element viscoelastic model under stress loading is given by (see, for example, Williams 1980):

$$W/W_m = 2\omega T/(1 + \omega^2 T^2) \quad (35)$$

where ω is the angular frequency of the applied stress and W_m is the maximum value of W , which occurs at $\omega = 1/T$. $W(\omega)$ is plotted in figure 8(b).

The loading time for material at distance r from the crack tip is $t = r/V$, with an equivalent frequency $\omega \sim V/r$. The frequency content of the moving stress field therefore lies between $\omega \sim V/h$ (point B' in figure 8(b)) and $\omega \sim V/l$ (point A'). A' and B' move to the right with increasing V . At very low speeds ($VT/l \ll 1$), $W \ll W_m$ for all the relevant frequency components. As VT/l approaches unity ($A' = 0$), however, the material close to the crack tip starts dissipating energy strongly. Comparison with figure 8(a) shows that at this speed ($A = 0$), $\phi(V)$ is rising significantly above zero for the first time. At higher speeds, W decreases close to the crack tip, and the strongest dissipation occurs at a radius $r \sim VT$. This lossy zone spreads out with increasing V until it coincides with the specimen boundary ($VT/h \sim 1$, corresponding to $B' = 0$). Further increases in V would therefore be expected to result in the entire specimen becoming progressively less dissipative. For comparison, the equivalent point $B = 0$ in figure 8(a) represents the onset of a significant downturn in $\phi(V)$.

8. Fracture of PMMA

The fracture properties of the brittle polymer polymethyl methacrylate (PMMA) have been studied in some detail (see, for example, Marshall et al. 1969; Williams 1972; Marshall et al. 1974; Fuller et al. 1975; Döll et al. 1979; Takahashi et al. 1984). Slow crack growth is observed when K_1 exceeds about $0.8 \text{ MPa m}^{1/2}$; the crack speed increases with K_1 until a point of instability is reached at $K_1 \approx 1.6 \text{ MPa m}^{1/2}$, $V \approx 0.1 \text{ m s}^{-1}$ (Marshall et al. 1969; Marshall et al. 1974). Experiments using ultrasonic fractography showed that the transition from slow to fast crack growth occurs almost instantaneously, with a final crack speed in the range $90\text{-}150 \text{ m s}^{-1}$

(Takahashi et al. 1984). PMMA behaves in a viscoelastic manner at room temperature; it is therefore of interest to investigate the possible rôle of the viscoelastic loss function in the slow-to-fast transition.

The craze zone at the tip of a crack in PMMA has been modelled as a Dugdale plastic zone (Williams 1972; Marshall et al. 1974). In terms of the zone length, l , and crack opening displacement, u , the fracture parameters are given by

$$K_I = \sigma_y (8l/\pi)^{1/2} \quad (36)$$

$$2\gamma = u\sigma_y \quad (37)$$

where σ_y is the yield stress. It may be assumed (Marshall et al. 1974) that σ_y is related to the yield strain ϵ_y , and K_I^2 to 2γ , through the modulus at time $t = l/V$:

$$\sigma_y = \epsilon_y / C(l/V) \quad (38)$$

$$K_I^2 = 2\gamma / C(l/V) \quad (39)$$

It is observed experimentally that l and u are constant ($l = 35 \mu\text{m}$; $u = 2.7 \mu\text{m}$), varying by only a few per cent for crack speeds in the range $10^{-11} - 2 \times 10^{-2} \text{ m s}^{-1}$ (Döll et al. 1979). Likewise, ϵ_y is essentially rate independent (Williams 1972). In the Greenwood and Johnson model considered in §6, the magnitude of the surface forces was taken to be velocity independent, and changes in K_I arose from the varying zone length; in the present case, l is constant whereas σ_y is velocity dependent. A further consequence of the rate dependence of σ_y is that 2γ now varies with crack speed. However, equation (39) relating K_I to 2γ is identical to equation (29), so equation (34) is still valid as an approximate expression for the loss function.

Figure 9 shows the creep function for cast PMMA (ICI 'Perspex', molecular weight $\approx 2.5 \times 10^6$). The data, kindly supplied by Drs Read and Dean, was obtained by a variety of techniques (Read and Dean 1984), and altogether covers over 17 decades of time. The loss function was calculated from equation (34), with l taking the constant value of $35 \mu\text{m}$. Two curves are shown in figure 10, corresponding to specimen dimensions of 35 mm ($m = 10^3$) and 350 mm ($m = 10^4$). Both curves show a region of negative gradient, and the critical velocity is about $3 \times 10^{-2} \text{ m s}^{-1}$. This compares well with the experimental value, typically in the range $10^{-2} - 10^{-1} \text{ m s}^{-1}$. For example, Marshall et al. (1974) observed velocities up to $2 \times 10^{-2} \text{ m s}^{-1}$ in double torsion tests at 20°C ; when the K - V curve was extrapolated to K_{Ic} , the corresponding critical velocity was estimated as $5 \times 10^{-2} \text{ m s}^{-1}$. Another interesting feature is that the apparent fracture surface energy for the large specimen ($G_c \approx 2.96\gamma$) is about 9% higher than that for the smaller one ($G_c \approx 2.72\gamma$), with both values substantially higher than the true surface energy, 2γ .

Although equation (38) suggests that σ_y increases monotonically with crack speed, thermal effects are likely to reduce the yield stress at high V (Williams 1972). Experiments on PMMA have indicated temperature rises of up to 500 K at crack speeds of several hundred m s^{-1} (Fuller et al. 1975). The instability phenomenon may therefore be partly due to thermal softening, since both 2γ and K_I are proportional to σ_y (equations (36) and (36)). However, any variation of the true fracture surface energy with crack speed will be modified by the additional multiplicative factor $(1 + \phi(V))$, so the bulk viscoelastic losses are likely to play at least a contributory rôle in the onset of fast crack growth in PMMA.

9. Conclusions

The problem considered in this paper was that of a crack moving at constant speed V along an infinite viscoelastic strip of width $2h$. Moving edge tractions imposed a stress intensity factor K_I , and the strain energy release rate G required to maintain the propagation was calculated as a function of V . It was found that the modulus relating G to K_I^2 could be approximated by the reciprocal of the creep compliance function at time $t = h/V$. By incorporating a Barenblatt or Dugdale crack tip model (zone length l), in which the modulus relating K_I^2 to 2γ is approximated by the reciprocal of the creep function at $t = l/V$, $G/2\gamma$ was shown to be given approximately by the ratio $C(h/V)/C(l/V)$. By contrast with previous work (which assumed G to be related to K_I^2 through the relaxed modulus E_∞), the present analysis predicts a region on the G - V curve having negative gradient, and hence provides a possible explanation for the instability phenomena observed in the adhesive and cohesive failure of polymers. The critical point (G_c, V_c) at which

$dG/dV = 0$, is predicted to be dependent on specimen size, with large specimens having greater apparent fracture surface energy than small ones. This effect may be important in understanding the performance of thin adhesive joints and filled polymers.

When applied to the mildly viscoelastic brittle polymer PMMA, it was found that as well as the 2γ dissipated as plastic work at the crack tip, bulk viscoelastic losses accounted for an additional amount approximately equal to γ at the critical crack speed, for specimen dimensions $h = 350$ mm. The losses were reduced by about 25% for specimens an order of magnitude smaller. The critical velocity V_c was predicted to be about 3×10^{-2} m s⁻¹, in good agreement with the value observed at the onset of the velocity discontinuity. Although other effects such as thermal softening must also be considered, it would appear that the viscoelastic loss function is a significant factor in the fracture behaviour of PMMA, controlling both the slow crack speed regime and the slow-to-fast transition.

Acknowledgments

The author is grateful to Dr J E Field for his encouragement with the project, and to Prof D Tabor, Dr J A Greenwood and Prof K L Johnson for useful discussions. The creep data on PMMA was kindly provided by Drs B E Read and G D Dean. The author thanks Gonville and Caius College, Cambridge, and the Science and Engineering Research Council for Research Fellowships. The work was supported in part by the M.O.D. and the U.S. European Office on contract DAJA 45-89-C0009.

References

- Andrews, E.H. and Kinloch, A.J. 1973 *Proc. R. Soc. Lond. A* **332**, 385-399.
Christensen, R.M. and Wu, E.M. 1981 *Eng. Fracture Mech.* **14**, 215-225.
Döll, W., Schinker, M.G., and Koenczoel, L. 1979 *Int. J. Fracture* **15**, R145-149.
Fuller, K.N.G., Fox, P.G. and Field, J.E. 1975 *Proc. R. Soc. Lond. A* **341**, 537-557.
de Gennes, P.G. 1988 *C.R. Acad. Sc. Paris II* **307**, 1949-1953.
Gent, A.N. and Schultz, J. 1972 *J. Adhesion* **3**, 281-294.
Graham, G.A.C. 1968 *Q. Appl. Math.* **26**, 167-174.
Greensmith, H.W. and Thomas, A.G. 1955 *J. Polymer Sci.* **18**, 189-200.
Greenwood, J.A. and Johnson, K.L. 1981 *Phil. Mag. A* **43**, 697-711.
Huntley, J.M. 1987 Ph.D. Thesis, University of Cambridge, England.
Lawn, B.R. and Wilshaw, T.R. 1975 *Fracture of brittle solids* Cambridge: University Press.
Marshall, G.P., Culver, L.E., and Williams, J.G. 1969 *Plastics and Polymers* **37**, 75-81.
Marshall, G.P., Coutts, L.H. and Williams, J.G. 1974 *J. Mat. Sci.* **9**, 1409-1419.
Maugis, D. and Barquins, M. 1978 *J. Phys. D* **11**, 1989-2023.
Maugis, D. 1985 *J. Mat. Sci.* **20**, 3041-3073.
Mueller, H.K. and Knauss, W.G. 1971a *Trans. Soc. Rheology* **15**, 217-233.
Mueller, H.K. and Knauss, W.G. 1971b *J. Appl. Mech.* **38**, Series E 483-488.
Read, B.E. and Dean, G.D. 1984 *Polymer* **25**, 1679-1686.
Rice, J.R. 1968 In *Fracture*, pp. 191-311. New York: Academic Press.
Schapery, R.A. 1975a *Int. J. Fracture* **11**, 369-387.
Schapery, R.A. 1975b *Int. J. Fracture* **11**, 141-158.
Takahashi, K., Matsushige, K. and Sakurada, Y. 1984 *J. Mat. Sci.* **19** 4026-4034.
Williams, J.G. 1972 *Int. J. Fracture Mech.* **8**, 393-401.
Williams, J.G. 1980 *Stress analysis of polymers*. Chichester: Ellis Horwood.

Figure Captions

Figure 1. Schematic illustration of the effect of viscoelastic losses on the variation of strain energy release rate (G) with crack speed (V). (G_c, V_c) represents the critical point, marking the transition from slow to fast crack growth.

Figure 2. Strip geometry used in the calculation of strain energy release rate.

Figure 3. (a) Three-element viscoelastic model. (b) Creep function of the model in (a), in terms of non-dimensional distance along the strip, $\beta = x/h$, for different non-dimensional crack velocities VT/h , where T is the relaxation time. $E_0/E_\infty = 5$ in this example. (c) Functions $q_j(\beta)$ (for the case $v = 0$) with which $C(\beta h/V)$ is convolved in calculating the strain distribution along the edge of the strip.

Figure 4. Variation of G/K_1^2 with non-dimensional crack velocity VT/h for a three element viscoelastic material. E_0 and E_∞ are the instantaneous and relaxed modulus respectively, and v is Poisson's ratio.

Figure 5. Variation of $K_1^2/2\gamma$ with non-dimensional crack velocity VT/l_0 (l_0 = Barenblatt zone length at zero crack velocity) for the Greenwood and Johnson model, as applied to a three element viscoelastic material.

Figure 6. Variation of $G/2\gamma$ with non-dimensional crack velocity VT/l_0 , obtained by combining Figures 4 and 5. The five curves show the effect of varying the specimen size ($m = h/l_0$). k ($= E_0/E_\infty$) = 10^3 in each case.

Figure 7. Variation of G/K_1^2 with non-dimensional crack velocity VT/h : approximate result (equation 33), which may be compared with the exact behaviour shown in Fig. 4.

Figure 8. (a) Creep function for three element viscoelastic model with time constant T and $E_0/E_\infty = 10^3$. Points A and B represent times $t = l/V$ and h/V respectively, and move from right to left with increasing V . The loss function $\phi(V)$ can be deduced from the intercepts on the vertical axis as shown. (b) Energy dissipated per cycle by the three element model under cyclic stress loading of angular frequency ω . Points A' and B' represent frequencies $\omega = V/l$ and V/h respectively, and move from left to right with increasing V .

Figure 9. Creep function for PMMA.

Figure 10. Viscoelastic loss function for PMMA. The two curves $m = 10^3$ and 10^4 correspond to specimen dimensions of $h \approx 35$ mm and 350 mm, respectively.

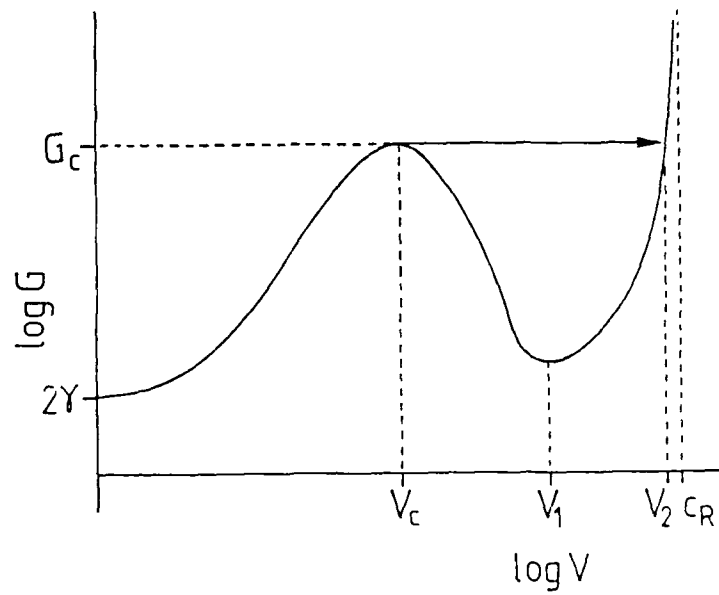


Fig. 1

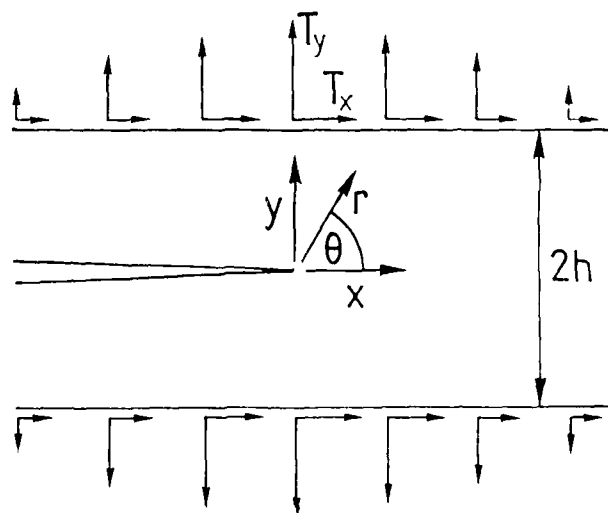


Fig. 2

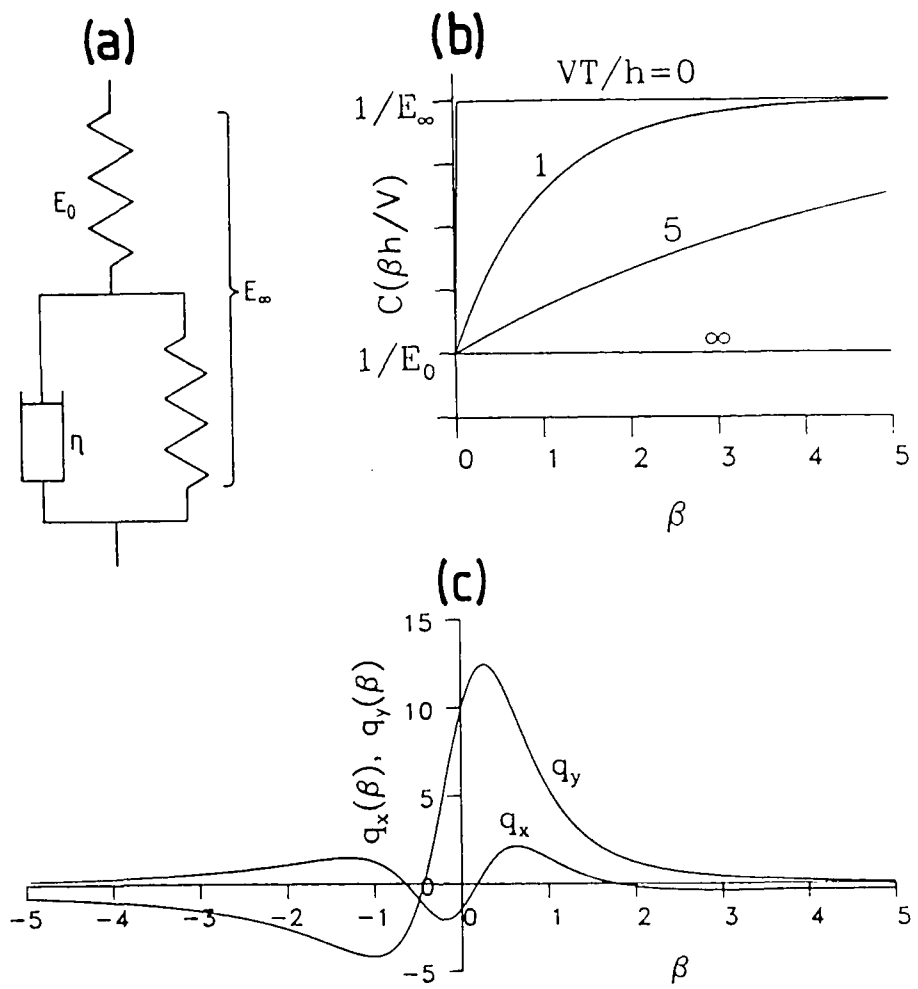


Fig. 3

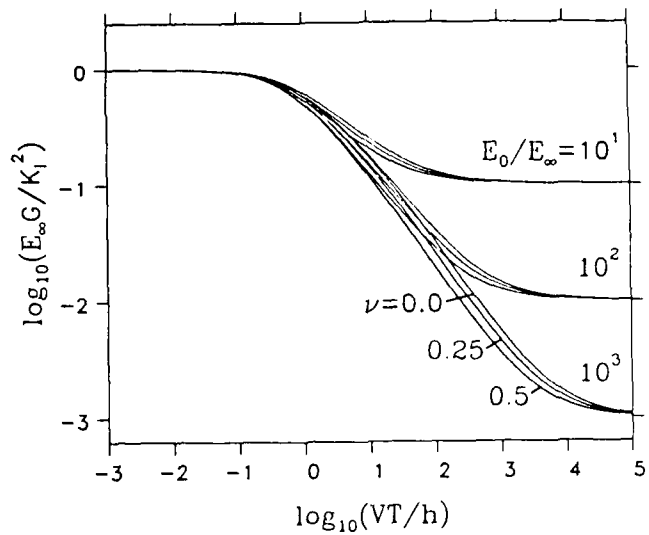


Fig. 4

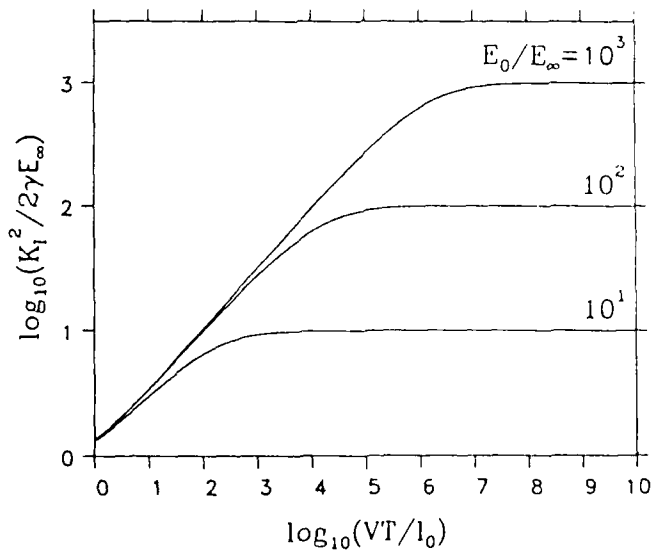


Fig. 5

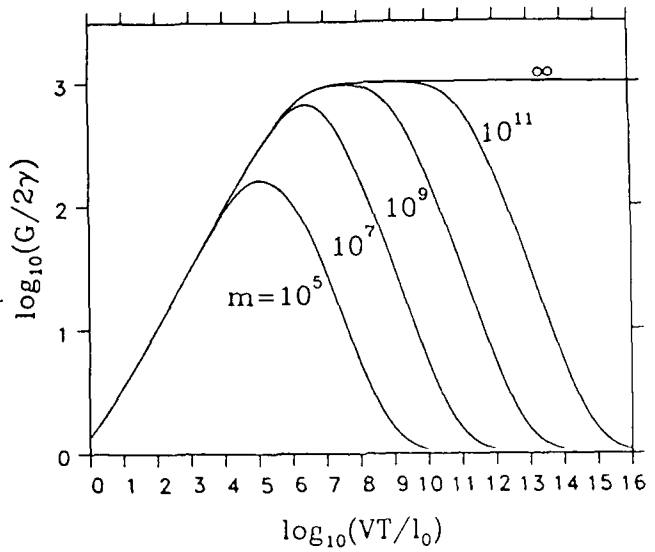


Fig. 6

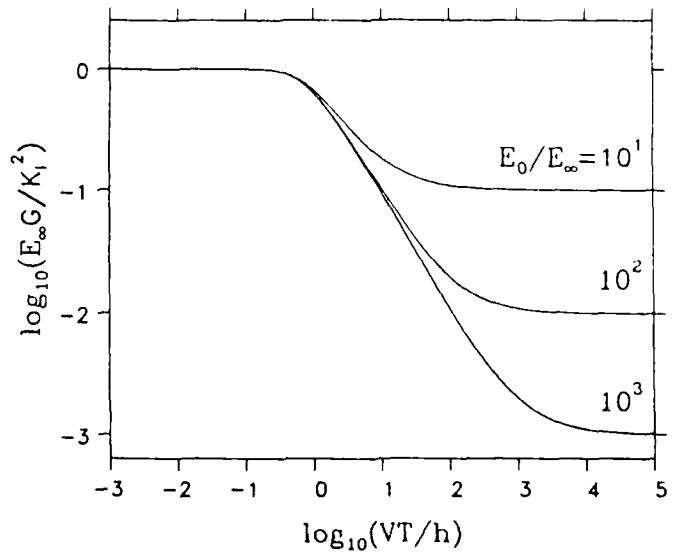


Fig. 7

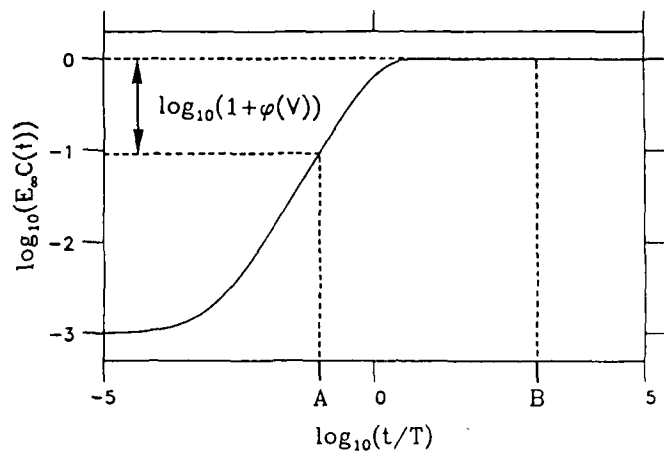


Fig. 8(a)

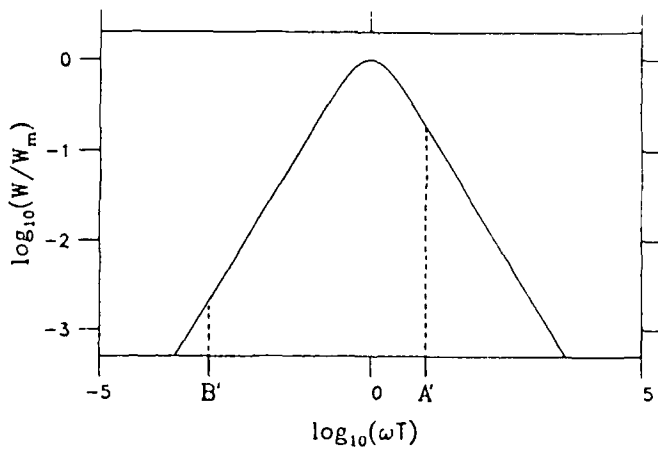


Fig. 8(b)

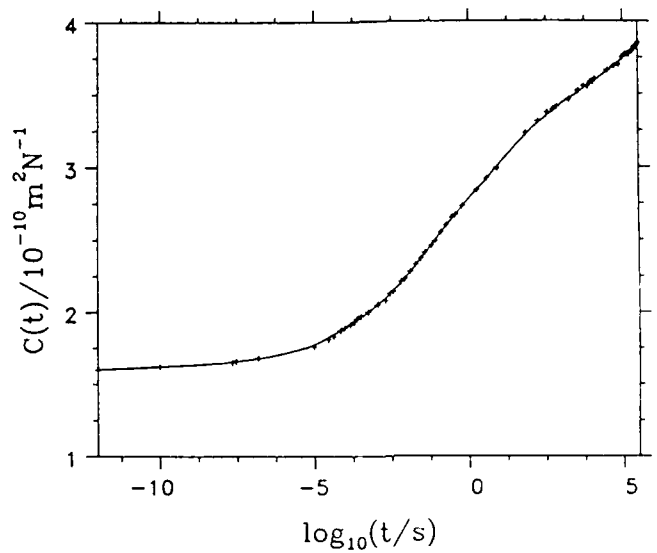


Fig. 9

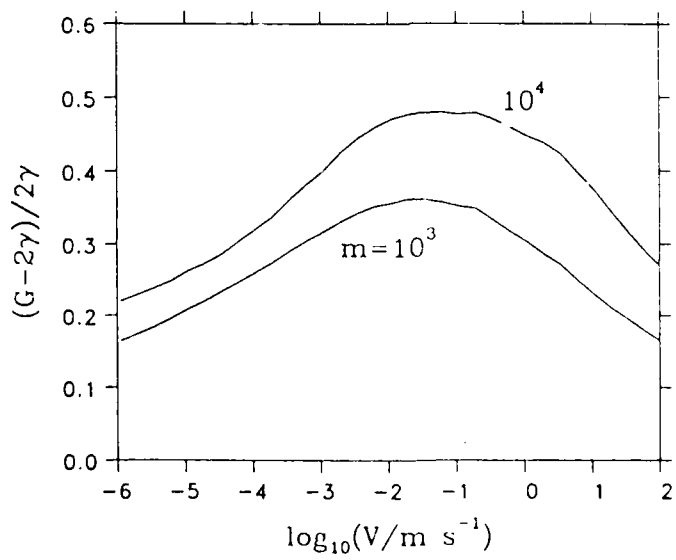


Fig. 10